ISBN 978-82-326-2664-9 (printed version)
ISBN 978-82-326-2665-6 (electronic version)
ISSN 1503-8181

Finn-Idar Grøtta Giske

Doctoral Thesis

Doctoral theses at NTNU, 2017:298

Finn-Idar Grøtta Giske

Long-Term Extreme Response Analysis of Marine Structures Using Inverse Reliability Methods

NTNU
Norwegian University of
Science and Technology
Faculty of Engineering
Department of MarineTechnology

NTNU
Norwegian University of
Science and Technology

Doctoral theses at NTNU, 2017:298

NTNU

NTNU
Norwegian University of
Science and Technology

Finn-Idar Grøtta Giske

Long-Term Extreme Response Analysis of Marine Structures Using Inverse Reliability Methods

Thesis for the degree of Philosophiae Doctor

Trondheim, December 2017

Norwegian University of Science and Technology
Faculty of Engineering
Department of MarineTechnology

NTNU
Norwegian University of
Science and Technology

NTNU
Norwegian University of Science and Technology

Thesis for the degree of Philosophiae Doctor

Faculty of Engineering
Department of MarineTechnology

ISBN 978-82-326-2664-9 (printed version)
ISBN 978-82-326-2665-6 (electronic version)
ISSN 1503-8181

Doctoral theses at NTNU, 2017:298

Printed by Skipnes Kommunikasjon as

Summary

For the assessment of extreme responses needed in design of marine structures, a full long-term analysis is recognized as the most accurate approach. However, due to the very large number of structural response analyses traditionally needed for this approach, the computational effort is usually considered to increase above acceptable levels for complex structures, e.g. floating bridges. In this work, an effort is made towards more efficient, yet accurate, full long-term analyses.

This thesis is written as a collection of four papers, where each paper is either published or submitted for journal publication. In the first paper, a new method is presented for efficient calculation of auto- and cross-spectral densities in the stochastic modelling of ocean waves and wave loads. As part of the short-term response analyses, the method contributes to more efficient long-term response prediction. In the second paper, an exact and an approximate formulation for the long-term extreme response of marine structures are discussed and compared. A new method is proposed for the numerical solution of the exact formulation, based on an inverse first order reliability method (IFORM). In the third paper, the IFORM approach is further developed, and the accuracy of the long-term extreme response approximation is improved, using an inverse second order reliability method (ISORM) approach. Finally, in the fourth paper, the developments of the first three papers are demonstrated for a long-span pontoon bridge subjected to wave loads, revealing that characteristic values of the long-term extreme response can indeed be calculated in an efficient manner. Especially the ISORM approach is seen to provide high accuracy, using only a reasonable amount of short-term response calculations.

Hopefully, the contributions of this work will make full long-term extreme response analyses more attractive and available for the practical design of marine structures.

Preface

This thesis is submitted in partial fulfilment of the requirements for the degree of philisophiae doctor (Ph.D.) at the Norwegian University of Science and Technology (NTNU). The research has been carried out from August 2014 to September 2017 at the department of Marine Technology, under the supervision of Professor Bernt Johan Leira and Associate Professor Ole Øiseth.

Acknowledgements

The work has been funded by Multiconsult ASA and by the Research Council of Norway as a part of the project *Chained Floating Bridge*, project number 235252. I am truly thankful for their support. I would also like to express my gratitude to Multiconsult for providing an excellent working environment during the last two years of this work.

Pursuing the Ph.D. degree has been a great challenge, and the road ahead was never lit up very far. The guidance provided by Professor Bernt Johan Leira and Associate Professor Ole Øiseth has therefore been essential, and I truly appreciate their knowledge and dedication.

I would like to thank my colleagues at the Structural Dynamics Group of the Department of Structural Engineering, NTNU, for treating me as one of their own. I would also like to thank my fellow Ph.D. candidates at Multiconsult, Morten and Reignard, for sharing in the joy and frustration of pursuing a Ph.D. degree.

Last, but not least, the fondest thanks to all of my family, in particular my wife Ingvild and my daughter Laurentse, for the love and joy you bring into my life.

Finn-Idar Grøtta Giske
Oslo, December 2017

Contents

CHAPTER 1

Introduction

1.1 Background and motivation

1.1.1 Long-term design approach

For the evaluation of extreme response of marine structures due to environmental loads, a full long-term analysis is recognized as the most accurate design approach [60]. In principle, the full long-term approach takes into account all possible combinations of environmental parameters. This means that for straightforward methods such as full numerical integration and crude Monte Carlo simulation, a very large number of short-term response calculations have to be conducted. For complex structures, e.g. floating bridges, each short-term calculation is usually very time consuming, and the full long-term approach is often considered infeasible.

In recent years, efforts have been made to reduce the number of short-term calculations required for full long-term extreme response evaluation. These are based on the observation that many combinations of environmental parameters contribute little or nothing to the long-term extreme response. A copula based environmental modelling approach is proposed in [80], and the copula concept is further utilized in an adaptive refinement algorithm for more efficient long-term integration. In [68] an inverse FORM (IFORM) approach [79] is used to provide an estimate of the long-term extreme response. An importance sampling Monte Carlo simulation approach, based on the IFORM estimate, is also proposed.

The alternative to performing full long-term analyses, is to use simplified approaches, such as the environmental contour method [29, 30]. This is a highly efficient approach, which is widely used in practice. However, some sort of calibration against full long-term analysis is required [60].

In order to make the full long-term approach attractive and available for

practical design, further development of methods for carrying out full long-term analyses with a limited amount of short-term response calculations is important. It is believed that the very efficient IFORM method can be further developed with respect to accuracy, which motivates the work presented in this thesis.

1.1.2 Fjord crossings

Fjord crossing technology is currently a research topic of high interest in Norway. The Norwegian Public Roads Administration (NPRA) has launched the project *Coastal Highway Route E39* which aims at replacing eight ferry crossings along the west coast of Norway with fixed links. The fjord crossings considered in this project are quite extreme, with lengths up to 5 km and depths up to 1300 m. This calls for further development of existing fjord crossing technologies, as well as development of new technologies. Floating bridge technology is therefore a very relevant research topic.

The concept of floating bridges can be dated as far back as 2000 BC, but only the last 200 years they have been used as a part of modern infrastructure [77]. Most of the existing floating bridges are found in northern America, but Norway is also leading in the field with its two curved pontoon bridges, the Bergsøysund Bridge and the Nordhordland Bridge. Even though floating bridges are by far not as common as other bridge types, e.g. suspension bridges, they are considered cost-efficient alternatives for crossings with unusual depth or soft bottom [52].

A chained floating bridge is a new bridge concept that has the potential to reduce costs at wide crossings, where ferries are presently the most cost-efficient alternative [65]. With low construction costs, this concept could be an attractive alternative for fjord crossings in Norway and other places. A chained floating bridge has never before been built and the realization of such a bridge would represent a major technological advance.

The design of more extreme yet reliable fjord crossing structures motivates further development of methods for long-term stochastic extreme response analysis.

1.2 Outline of the thesis

This thesis is based on a collection of papers, which are either published or submitted for journal publication. The thesis is outlined as follows. Chapter 1 gives a brief introduction to the basic concepts and an overview of the relevant theory. The research objectives and the scope of the thesis are discussed, and the publications resulting from the work are listed and summarized. Some concluding remarks are made, along with recommendations for future work. Chapters 2-5 contain the individual papers. Chapters 2,3 and 5 contain the accepted manuscripts of the respective papers, whereas Chapter 4 contains the preprint submitted for journal publication. Finally, an error bound for the method developed in Chapter 2 is included in Appendix A.

1.3 Short-term response

Marine structures are subjected to environmental loads, such as wind and wave loads, which are inherently random. In order to account for these loads in the design of marine structures, the theory of stochastic processes has proven to be indispensable. For most engineering purposes, a sufficiently accurate description is obtained by modelling the environmental loads as stationary stochastic processes for a limited period of time, referred to as a short-term period [60]. The appropriate duration of a short-term period, denoted $\tilde{T}$, will depend on the type of environmental loads considered. For wave loads on offshore structures, $\tilde{T}$ is typically chosen as three hours. A short-term state is defined by a collection of environmental variables $\boldsymbol{W} = [W_1, W_2, \ldots, W_n]$, which are the parameters of the modelled load processes. Examples of such environmental variables are the significant wave height and period for wave loads, and mean wind speed for wind loads.

1.3.1 Structural response

In order to evaluate the load effects corresponding to the environmental loads, a model for the structural response is required. For complex structures, these models are usually made within the framework of the finite element method (FEM). If the time domain approach is applied, the structural response model is used to provide response realizations corresponding to simulated time series of the environmental loads. This approach is usually required when non-linear effects are significant. If, on the other hand,

the dynamics of the structure can be modelled as a linear, time-invariant system, the frequency domain approach is more efficient. The structural response model is then completely described by a complex transfer function matrix $\boldsymbol{H}(\omega)$, where ω is the frequency variable.

Given the environmental parameters $\boldsymbol{W}$, we consider some response process $R(t)|\boldsymbol{W}$ corresponding to the environmental loads. Here t is the time variable. The response process may represent e.g. an axial force or a bending moment of a critical component of the structure, or a displacement. For given environmental variables, we assume that the load processes are stationary and that the response process $R(t)|\boldsymbol{W}$ inherits this property. Without loss of generality, we also assume that $R(t)|\boldsymbol{W}$ has a mean value of zero. Thus $R(t)|\boldsymbol{W}$ is a zero mean stationary stochastic process, an assumption which is made throughout this thesis.

1.3.2 Short-term response statistics

An important quantity for the extreme value statistics of the stationary response process $R(t)|\boldsymbol{W}$, is the average upcrossing frequency or mean upcrossing rate. It is denoted $\nu(r|\boldsymbol{w})$ and is a measure of how often the process increases above a level r for given environmental parameters $\boldsymbol{W} = \boldsymbol{w}$. An r-upcrossing occurs if the process $R(t)|\boldsymbol{W}$ reaches the level r with a positive derivative. The mean upcrossing rate can be estimated by simulations of the response process, for instance using the efficient procedures presented in [35, 36]. Alternatively, if $R(t)|\boldsymbol{W}$ is assumed to be Gaussian, the mean upcrossing rate is given as

$$\nu(r|\boldsymbol{w}) = \frac{1}{2\pi}\frac{\sigma_{\dot{R}}(\boldsymbol{w})}{\sigma_R(\boldsymbol{w})}\exp\left\{-\frac{1}{2}\left(\frac{r}{\sigma_R(\boldsymbol{w})}\right)^2\right\}, \tag{1.1}$$

where $\sigma_R(\boldsymbol{w})$ and $\sigma_{\dot{R}}(\boldsymbol{w})$ are the standard deviations of the response process and its derivative respectively [60].

The short-term extreme value distribution is given by the cumulative distribution function (CDF) $F_{\tilde{R}|\boldsymbol{W}}(r|\boldsymbol{w})$, where $\tilde{R}|\boldsymbol{W} = \max\{R(t)|\boldsymbol{W} : t \in [0, \tilde{T}]\}$ is the random variable representing the largest response value during a short-term period. The extreme value distribution $F_{\tilde{R}|\boldsymbol{W}}(r|\boldsymbol{w})$ can be estimated from simulations of the response by assuming it to be a Gumbel distribution, or the average conditional exceedance rate (ACER) method can be applied [56]. Alternatively, by assuming upcrossings of high levels r to be independ-

ent events, the extreme value distribution can be expressed in terms of the mean upcrossing rate as

$$F_{\tilde{R}|\boldsymbol{W}}\left(r|\boldsymbol{w}\right) = \exp\left\{-\nu\left(r|\boldsymbol{w}\right)\tilde{T}\right\}, \tag{1.2}$$

which will be valid for large values of r. For details we refer to Section 10.5 of [60]. If the response process is also Gaussian, Eqns. (1.1) and (1.2) can be combined to give the expression

$$F_{\tilde{R}|\boldsymbol{W}}\left(r|\boldsymbol{w}\right) = \exp\left\{-\frac{\tilde{T}}{2\pi}\frac{\sigma_{\dot{R}}(\boldsymbol{w})}{\sigma_R(\boldsymbol{w})}\exp\left\{-\frac{1}{2}\left(\frac{r}{\sigma_R(\boldsymbol{w})}\right)^2\right\}\right\}.$$

We also consider the short-term peaks distribution. A response peak is defined as the maximum value of the response process $R(t)|\boldsymbol{W}$ between two consecutive zero-upcrossings. The value of an arbitrary response peak, denoted $\tilde{R}_p|\boldsymbol{W}$, is then a random variable whose CDF is $F_{\tilde{R}_p|\boldsymbol{W}}(r|\boldsymbol{w})$. Under the assumption of a narrow banded response process, the short-term peaks distribution can also be expressed in terms of the mean upcrossing rate. We have then that

$$F_{\tilde{R}_p|\boldsymbol{W}}(r|\boldsymbol{w}) = 1 - \frac{\nu(r|\boldsymbol{w})}{\nu(0|\boldsymbol{w})},\ r \geq 0, \tag{1.3}$$

which is valid if $R(t)|\boldsymbol{W}$ is narrow banded [60]. For the case of Gaussian response, Eqns. (1.1) and (1.3) yield

$$F_{\tilde{R}_p|\boldsymbol{W}}(r|\boldsymbol{w}) = 1 - \exp\left\{-\frac{1}{2}\left(\frac{r}{\sigma_R(\boldsymbol{w})}\right)^2\right\},\ r \geq 0,$$

which means that the peaks are Rayleigh distributed.

1.4 Long-term extreme response modelling

For the assessment of long-term extreme responses of marine structures, it is common to model the environmental conditions as a sequence of short-term states, during which the environmental processes are assumed stationary [60]. The long-term situation is composed of a large number $\tilde{N}$ of short-term conditions, each of duration $\tilde{T}$, giving a long-term time duration of $T = \tilde{N}\tilde{T}$.

In reality, the vector of environmental parameters $\boldsymbol{W} = [W_1, W_2, \ldots, W_n]$ is a stochastic process $\boldsymbol{W}(t)$, where t denotes time. Since observation can

only provide part of a single realization of $\boldsymbol{W}(t)$, an ergodicity assumption is required in order to estimate the probabilistic structure of $\boldsymbol{W}(t)$ [59]. Under the ergodicity assumption, observations of the environmental parameters over time can be used to estimate the joint probability density function (PDF) $f_{\boldsymbol{W}}(\boldsymbol{w})$ of the environmental parameters.

Denoting the considered (zero mean) response process by $R(t)$, the aim of the long-term extreme response modelling is to establish a formulation for the long-term extreme value distribution

$$F_{\tilde{R}_{LT}}(r) = P[\tilde{R}_{LT} \leq r].$$

Here $\tilde{R}_{LT} = \max\{R(t) : t \in [0,T]\}$ denotes the largest response value during the entire long-term period, and $F_{\tilde{R}_{LT}}(r)$ is its CDF. In the literature, different models for the long-term extreme response can be found, resulting in different formulations for $F_{\tilde{R}_{LT}}(r)$. An overview of the most common models can be found in [68] and in Section 12.4 of [60]. The main difference between these models is which short-term statistics they are based on: The peaks distribution, the extreme value distribution or the mean upcrossing rate. In the following, we briefly introduce the different formulations.

1.4.1 Models based on all short-term peaks

Assuming that all response peaks are statistically independent, the long-term extreme value distribution can be formulated as

$$F_{\tilde{R}_{LT}}(r) = F_{\tilde{R}_p}(r)^{\overline{\nu(0)}T}.$$

Here $F_{\tilde{R}_p}(r)$ denotes the long-term distribution of an arbitrary response peak $\tilde{R}_p$, and $\overline{\nu(0)}$ is the long-term mean frequency of zero-upcrossings, defined as

$$\overline{\nu(0)} = \int_{\boldsymbol{w}} \nu\left(0|\boldsymbol{w}\right) f_{\boldsymbol{W}}\left(\boldsymbol{w}\right) d\boldsymbol{w}.$$

Thus, $\overline{\nu(0)}T$ represents the expected number of response peaks during the long-term period T.

An approximate formulation for the long-term peaks distribution, based on the short-term peaks distribution $F_{\tilde{R}_p|\boldsymbol{W}}\left(r|\boldsymbol{w}\right)$, is given by

$$F_{\tilde{R}_p}(r) \approx \int_{\boldsymbol{w}} F_{\tilde{R}_p|\boldsymbol{W}}\left(r|\boldsymbol{w}\right) f_{\boldsymbol{W}}\left(\boldsymbol{w}\right) d\boldsymbol{w}.$$

Although it may appear correct, this formulation is only an approximation because it assumes that the number of response peaks is the same for all environmental conditions. This is not the case, and in order to account for this effect, the formulation known as Battjes' formulation was proposed in [6, 7]. The long-term peaks distribution is then given by

$$F_{\tilde{R}_p}(r) = \int_{\boldsymbol{w}} \frac{\nu(0|\boldsymbol{w})}{\overline{\nu(0)}} F_{\tilde{R}_p|\boldsymbol{W}}\left(r|\boldsymbol{w}\right) f_{\boldsymbol{W}}\left(\boldsymbol{w}\right) d\boldsymbol{w}.$$

1.4.2 Models based on the short-term extreme values

Let $\tilde{R}$ denote the maximum response value during an arbitrary short-term condition. Assuming that the short-term extreme values are independent, the long-term extreme value distribution $F_{\tilde{R}_{LT}}(r)$ is obtained as

$$F_{\tilde{R}_{LT}}(r) = F_{\tilde{R}}\left(r\right)^{\tilde{N}},$$

where $F_{\tilde{R}}\left(r\right)$ is the long-term CDF of the short-term extreme value. This can be obtained as an average of the short-term CDFs $F_{\tilde{R}|\boldsymbol{W}}(r|\boldsymbol{w})$, weighted by the distribution $f_{\boldsymbol{W}}(\boldsymbol{w})$ of the environmental parameters. The correct long-term CDF $F_{\tilde{R}}\left(r\right)$ is obtained when an ergodic averaging is used [39, 59], see also Section 12.4.2 of [60]. This yields the formulation

$$F_{\tilde{R}}\left(r\right) = \exp\left\{\int_{\boldsymbol{w}} \left(\ln F_{\tilde{R}|\boldsymbol{W}}\left(r|\boldsymbol{w}\right)\right) f_{\boldsymbol{W}}\left(\boldsymbol{w}\right) d\boldsymbol{w}\right\}. \tag{1.4}$$

A very common approximate formulation is obtained by using the population mean:

$$F_{\tilde{R}}\left(r\right) \approx \int_{\boldsymbol{w}} F_{\tilde{R}|\boldsymbol{W}}\left(r|\boldsymbol{w}\right) f_{\boldsymbol{W}}\left(\boldsymbol{w}\right) d\boldsymbol{w}. \tag{1.5}$$

1.4.3 Model based on the short-term uppcrossing rate

As shown in [59], the long-term extreme value distribution can be expressed directly in terms of the mean upcrossing rate $\nu(r|\boldsymbol{w})$ as

$$F_{\tilde{R}_{LT}}\left(r\right) = \exp\left\{-T\int_{\boldsymbol{w}} \nu\left(r|\boldsymbol{w}\right) f_{\boldsymbol{W}}\left(\boldsymbol{w}\right) d\boldsymbol{w}\right\}. \tag{1.6}$$

This formulation assumes that upcrossings of high levels r are statistically independent, i.e. that the upcrossings are Poisson-distributed. This

is a reasonable assumption, especially when extreme values are considered. Furthermore, it is less restrictive than assuming independence of extreme values or all peaks.

Under the assumption of independent upcrossings of high levels, the short-term extreme value distribution $F_{\tilde{R}|\boldsymbol{W}}(r|\boldsymbol{w})$ can be expressed by Eqn. (1.2). Solving Eqn. (1.2) for the mean upcrossing rate gives the relation

$$\nu(r|\boldsymbol{w}) = -\frac{1}{\tilde{T}} \ln F_{\tilde{R}|\boldsymbol{W}}(r|\boldsymbol{w}).$$

Inserting this expression into Eqn. (1.6) yields

$$F_{\tilde{R}_{LT}}(r) = \exp\left\{\int_{\boldsymbol{w}} \left(\ln F_{\tilde{R}|\boldsymbol{W}}(r|\boldsymbol{w})\right) f_{\boldsymbol{W}}(\boldsymbol{w})\, d\boldsymbol{w}\right\}^{T/\tilde{T}} = F_{\tilde{R}}(r)^{\tilde{N}},$$

since $T = \tilde{N}\tilde{T}$. Here $F_{\tilde{R}}(r)$ is the long-term CDF of the short-term extreme value as given by the formulation Eqn. (1.4). This shows that the formulations represented by Eqns. (1.4) and (1.6) are the same, and the only assumption required for either one is independent upcrossings of high levels.

1.4.4 Characteristic values of the extreme response

When long-term extreme responses are calculated for design purposes, we usually seek the characteristic response value r_q which has a specified annual exceedance probability q. This may also be referred to as the response value with a return period of $1/q$ years, or simply the $1/q$-year response. The characteristic response r_q is found by requiring

$$F_{\tilde{R}_{LT}}(r_q) = 1 - q,$$

with the long-term period T taken as one year. Alternatively, the requirement can be written in terms of the long-term CDF of the short-term extreme value as

$$F_{\tilde{R}}(r_q) = (1-q)^{1/\tilde{N}} \approx 1 - \frac{q}{\tilde{N}},$$

where $\tilde{N}$ is the number of short-term periods in one year. It should be noted that the above approximation is as good as exact, since q is a small number and $\tilde{N}$ is large.

1.5 Reliability methods

1.5.1 Reliability problem

A reliability problem in the general sense is an integral of the form

$$\int\limits_{G(\boldsymbol{v})\leq 0} f_{\boldsymbol{V}}(\boldsymbol{v})d\boldsymbol{v}, \tag{1.7}$$

where $\boldsymbol{V} = [V_1, V_2, \cdots, V_m]$ is a random vector with joint PDF $f_{\boldsymbol{V}}(\boldsymbol{v})$, and $G(\boldsymbol{v})$ is a function referred to as the limit state function [53]. Usually the value of the integral is small, representing the probability of failure in some sense. It is well known that an expression of the form

$$F(r) = \int\limits_{\boldsymbol{w}} F_{Y|\boldsymbol{W}}\left(r|\boldsymbol{w}\right) f_{\boldsymbol{W}}\left(\boldsymbol{w}\right) d\boldsymbol{w},$$

where Y is a random variable and $\boldsymbol{W}$ a random vector, can be reformulated in terms of a reliability problem. Indeed, the above expression can be rewritten as

$$F(r) = \int\limits_{\boldsymbol{w}} \int\limits_{y\leq r} f_{Y|\boldsymbol{W}}\left(y|\boldsymbol{w}\right) dy f_{\boldsymbol{W}}\left(\boldsymbol{w}\right) d\boldsymbol{w}.$$

Introducing the random vector $\boldsymbol{V} = [\boldsymbol{W}, Y]$, whose joint PDF is given by $f_{\boldsymbol{V}}\left(\boldsymbol{v}\right) = f_{Y|\boldsymbol{W}}\left(y|\boldsymbol{w}\right) f_{\boldsymbol{W}}\left(\boldsymbol{w}\right)$, we obtain

$$F(r) = \int\limits_{y\leq r} f_{\boldsymbol{V}}\left(\boldsymbol{v}\right) d\boldsymbol{v} = 1 - \int\limits_{r\leq y} f_{\boldsymbol{V}}\left(\boldsymbol{v}\right) d\boldsymbol{v} = 1 - \int\limits_{G_r(\boldsymbol{v})\leq 0} f_{\boldsymbol{V}}\left(\boldsymbol{v}\right) d\boldsymbol{v}.$$

Here the limit state function is $G_r(\boldsymbol{v}) = r - y$, with y being the last component of the vector $\boldsymbol{v} = [\boldsymbol{w}, y]$.

1.5.2 First- and second-order reliability methods

The integral Eqn. (1.7) can be solved efficiently in an approximate manner using the first-order reliability method (FORM). The random vector $\boldsymbol{V}$ is then transformed into a vector $\boldsymbol{U}$ of independent standard normal variables by the Rosenblatt transformation $\boldsymbol{U} = T(\boldsymbol{V})$ [53], defined by the equations

$$\Phi\left(U_1\right) = F_{V_1}\left(V_1\right), \tag{1.8a}$$
$$\Phi\left(U_i\right) = F_{V_i|V_1,\ldots,V_{i-1}}\left(V_i|V_1,\ldots,V_{i-1}\right), i = 2,\ldots,m-1, \tag{1.8b}$$
$$\Phi\left(U_m\right) = F_{V_m|V_1,\ldots,V_{m-1}}\left(V_m|V_1,\ldots,V_{m-1}\right), \tag{1.8c}$$

where $\Phi(\cdot)$ denotes the standard normal CDF. Given a point $\boldsymbol{u}$ in the standard normal space, the inverse transformation evaluated at $\boldsymbol{u}$, i.e. $\boldsymbol{v} = T^{-1}(\boldsymbol{u})$, can be found by solving the equations in Eqn. (1.8) successively, obtaining

$$\begin{aligned}
v_1\left(\boldsymbol{u}\right) &= F_{V_1}^{-1}\left(\Phi\left(u_1\right)\right), \\
v_i\left(\boldsymbol{u}\right) &= F_{V_i|V_1,\ldots,V_{i-1}}^{-1}\left(\Phi\left(u_i\right)|v_1\left(\boldsymbol{u}\right),\ldots,v_{i-1}\left(\boldsymbol{u}\right)\right), i = 2,\ldots,m-1, \\
v_m\left(\boldsymbol{u}\right) &= F_{V_m|V_1,\ldots,V_{m-1}}^{-1}\left(\Phi\left(u_m\right)|v_1\left(\boldsymbol{u}\right),\ldots,v_{m-1}\left(\boldsymbol{u}\right)\right).
\end{aligned}$$

Knowing that the Rosenblatt transformation preserves probability, Eqn. (1.7) is then rewritten in terms of the transformed variables as

$$\int\limits_{G(\boldsymbol{v})\leq 0} f_{\boldsymbol{V}}\left(\boldsymbol{v}\right) d\boldsymbol{v} = \int\limits_{g(\boldsymbol{u})\leq 0} f_{\boldsymbol{U}}\left(\boldsymbol{u}\right) d\boldsymbol{u}.$$

Here $f_{\boldsymbol{U}}(\boldsymbol{u})$ denotes the PDF of the multivariate standard normal distribution, and $g\left(\boldsymbol{u}\right) = G\left(T^{-1}\left(\boldsymbol{u}\right)\right)$ is the transformed limit state function.

When FORM is applied, the transformed limit state function is replaced by its linear approximation at the most probable point (MPP) $\boldsymbol{u}^*$, i.e. the point on the surface $g(\boldsymbol{u}) = 0$ closest to the origin. The MPP $\boldsymbol{u}^*$ and the smallest distance β is found by solving the minimization problem

$$\beta = \min|\boldsymbol{u}|;\ \text{subject to } g(\boldsymbol{u}) = 0, \tag{1.10}$$

and the integral Eqn. (1.7) is finally approximated by

$$\int\limits_{G(\boldsymbol{v})\leq 0} f_{\boldsymbol{V}}\left(\boldsymbol{v}\right) d\boldsymbol{v} = \int\limits_{g(\boldsymbol{u})\leq 0} f_{\boldsymbol{U}}\left(\boldsymbol{u}\right) d\boldsymbol{u} \approx \Phi(-\beta). \tag{1.11}$$

When SORM is applied, $g(\boldsymbol{u})$ is replaced by its quadratic approximation at the MPP $\boldsymbol{u}^*$. Although an exact solution does exist for the quadratic approximation [46], the asymptotic result of [10] is commonly used, as it

gives a simpler expression where the FORM solution is corrected by a SORM factor. We have then

$$\int\limits_{G(\boldsymbol{v})\leq 0} f_{\boldsymbol{V}}\left(\boldsymbol{v}\right) d\boldsymbol{v} = \int\limits_{g(\boldsymbol{u})\leq 0} f_{\boldsymbol{U}}\left(\boldsymbol{u}\right) d\boldsymbol{u} \approx \Phi(-\beta) \prod_{i=1}^{m-1} \left(1-\beta\kappa_i\right)^{-\frac{1}{2}}.$$

where κ_i are the main curvatures of the surface $g(\boldsymbol{u}) = 0$ at $\boldsymbol{u}^*$.

1.5.3 Inverse reliability methods

An inverse reliability problem arises when the value of the integral Eqn. (1.7) is specified, and some parameter of the limit state function is to be determined. An important example is the case where the limit state function can be written as $G_r(\boldsymbol{v}) = r - H(\boldsymbol{v})$ for some function $H(\boldsymbol{v})$, and we want to determine the value r_q such that

$$\int\limits_{G_{r_q}(\boldsymbol{v})\leq 0} f_{\boldsymbol{V}}(\boldsymbol{v}) d\boldsymbol{v} = q, \tag{1.12}$$

where q is a specified value. The transformed limit state function is given as $g_r(\boldsymbol{u}) = r - H(T^{-1}(\boldsymbol{u})) = r - h(\boldsymbol{u})$.

Applying the FORM approximation Eqn. (1.11) to the inverse reliability problem Eqn. (1.12), the target value of β is derived as $\beta = -\Phi^{-1}(q)$. Thus, conferring Eqn. (1.10), we seek the value r_q such that β is the minimal distance from the origin to the surface $g_{r_q}(\boldsymbol{u}) = r_q - h(\boldsymbol{u}) = 0$. According to [17, 79] this inverse FORM (IFORM) problem can be formulated as

$$r_q = \max h(\boldsymbol{u}); \text{ subject to } |\boldsymbol{u}| = \beta.$$

If we want to use the SORM approximation for the inverse reliability problem Eqn. (1.12), the target value for β can no longer be derived directly. However, inverse SORM (ISORM) approaches can be derived by updating β iteratively [49].

1.6 Research objectives and scope

1.6.1 Research objectives

The primary objective of this work is to develop more efficient, yet accurate, methods for full long-term extreme response analysis of marine structures, making such analyses feasible also for complex structures such as floating bridges. In an effort to achieve this goal, the following research objectives have been realized in the papers presented in this thesis.

To develop an accurate and efficient method for computation of cross-spectral densities in the stochastic modelling of waves and wave loads. In the short-term response analysis of marine structures, the auto- and cross-spectral densities of the wave load are important quantities, and their evaluation may contribute significantly to the computation time, for instance when the power spectral density method [42] is applied. The cross-spectral densities of waves and wave loads can be formulated in terms of an integral that requires numerical evaluation for each realization of the environmental variables $\boldsymbol{W}$. Therefore, it is important for the long-term analysis that these are calculated in an accurate and efficient manner.

To study and compare models for long-term extreme response. The basis of any computational method for the characteristic long-term response, is some model for the long-term extreme response, cf. Section 1.4. An understanding of the different models found in the literature, and their effect on the characteristic response, is therefore important for the development of the computational methods.

To develop a novel IFORM method for calculation of long-term extreme response. An IFORM method for efficient calculation of long-term extreme response can be found in the literature [68, 79]. This IFORM method is, however, based on the approximate formulation Eqn. (1.5). The development of an IFORM method based on the correct formulation Eqn. (1.4) is therefore of interest.

To develop an ISORM method for calculation of long-term extreme response. By using the second-order reliability method (SORM) instead of FORM, improved accuracy can be achieved. The development of an ISORM method for calculation of long-term extreme response is therefore of interest.

To verify the efficiency and accuracy of the developed IFORM and ISORM methods for a complex structure. The efficiency and accuracy of the IFORM and ISORM methods for calculation of long-term extreme response should be verified, when applied to a complex structure such as a floating bridge.

To develop a computational framework for efficient long-term extreme response calculations of floating bridges. Pontoon bridges serve as the main application considered in this thesis. The examples used to demonstrate the developed methods should therefore constitute a framework for efficient long-term extreme response calculations of floating bridges.

1.6.2 Scope

For the IFORM and ISORM methods for long-term extreme response developed in this thesis, only the models based on the short-term extreme values, cf. Section 1.4.2, are considered. The models presented in Section 1.4.1 based on all short-term peaks are not considered, as they require more restrictive assumptions. As showed in Section 1.4.3, the model based on the upcrossing rate is equivalent to the model represented by Eqn. (1.4).

Proper estimation of the PDF $f_{\boldsymbol{W}}(\boldsymbol{w})$ of the environmental variables is of major importance for accurate long-term extreme response prediction. Also the choice of which parameters to include is important. However, the environmental modelling is not the focus of this work, and the PDF $f_{\boldsymbol{W}}(\boldsymbol{w})$ will be assumed to be given.

The details of the structural modelling is also considered to be outside the scope of this work. The structural response model for the floating bridge considered in Paper IV is provided by Knut Andreas Kvåle, who has also contributed with a description of the model, which is included in Paper IV.

The long-term extreme response models presented in Section 1.4 are all global models [14], considering all environmental conditions. This is recognized as an appropriate modelling approach for extratropical weather conditions. The alternative would be an event model, or random storm approach, where only the most severe environmental conditions are considered. Such an approach is appropriate for tropical weather conditions, and is considered outside the scope of this thesis.

1.7 Publications

1.7.1 List of publications

The following papers are included in this thesis:

I [20] Giske, F.-I. G., Leira, B. J. and Øiseth, O. 'Efficient computation of cross-spectral densities in the stochastic modelling of waves and wave loads'. *Applied Ocean Research* 62 (2017), pp. 70–88. doi:10.1016/j.apor.2016.11.007.

II [21] Giske, F.-I. G., Leira, B. J. and Øiseth, O. 'Full long-term extreme response analysis of marine structures using inverse FORM'. *Probabilistic Engineering Mechanics* 50 (2017), pp. 1–8. doi:10.1016/j.probengmech.2017.10.007.

III [22] Giske, F.-I. G., Leira, B. J. and Øiseth, O. 'Long-term extreme response analysis of marine structures using inverse SORM'. *Submitted for journal publication* (2017).

IV [26] Giske, F.-I. G., Kvåle, K. A., Leira, B. J. and Øiseth, O. 'Long-term extreme response analysis of a long-span pontoon bridge'. *Marine Structures* 58 (2018), pp. 154–171. doi:10.1016/j.marstruc.2017.11.010

The following papers have been accepted for publication in various conference proceedings:

V [25] Giske, F.-I. G., Leira, B. J. and Øiseth, O. 'Stochastic modelling of wave loads on floating bridges: efficient calculation of cross-spectral densities'. *IABSE Congress Report*. Vol. 19. IABSE, 2016, pp. 48–56.

VI [23] Giske, F.-I. G., Leira, B. J. and Øiseth, O. 'Long-term extreme response analysis of marine structures using inverse SORM'. *ASME 2017 36th International Conference on Ocean, Offshore and Arctic Engineering*. Vol. 3A. ASME, 2017. doi:10.1115/OMAE2017-61409.

VII [24] Giske, F.-I. G., Leira, B. J. and Øiseth, O. 'Long-term stochastic extreme response analysis of floating bridges'. *Procedia Engineering* 199 (2017), pp. 1175–1180. doi:10.1016/j.proeng.2017.09.305.

1.7.2 Declaration of authorship

Finn-Idar G. Giske is the first author of all papers included in this thesis (Papers I-IV). For Papers I-III, he came up with the main ideas, implemented the theory, obtained the numerical results and wrote the manuscripts. The co-authors Bernt J. Leira and Ole Øiseth provided constructive criticism, which increased the scientific quality. For Paper IV, Finn-Idar G. Giske came up with the main ideas, implemented the theory, obtained the numerical results and wrote most of the manuscript. Knut Andreas Kvåle provided the structural response model of the case study bridge and wrote Sections 5.2.3 and 5.3. Bernt J. Leira and Ole Øiseth provided constructive criticism and discussed the work.

1.7.3 Summary of papers

Paper I

Long-term response analyses are conducted by performing several short-term response calculations. Hence, the efficiency of each short-term analysis is crucial for the overall efficiency. For floating bridges, and other marine structures, calculation of auto- and cross-spectral densities for the wave loads may represent a bottleneck. In Paper I, a new method is presented for efficient calculation of auto- and cross-spectral densities in the stochastic modelling of ocean waves and wave loads. The accuracy and the efficiency of the new method is investigated, and a comparison with the existing approach is performed. Using two floating bridge examples, it is demonstrated that the new method provides a significant improvement in computational efficiency.

Paper II

In Paper II the focus is shifted from the short-term response calculations to the long-term extreme response formulations and their solution. The goal is to reduce the number of short-term calculations needed for a long-term analysis. This can be achieved by means of the first order reliability method (FORM), known for its computational efficiency. In the existing literature, FORM is only applied to the approximate long-term formulation Eqn. (1.5). In Paper II, however, the more correct long-term formulation Eqn. (1.4) is solved in an approximate manner using FORM.

In order to obtain characteristic values of the long-term extreme response, an inverse FORM (IFORM) approach is applied. A new solution algorithm for IFORM is proposed in Paper II, resolving some convergence issues of an iteration algorithm found in the literature. Using a single-degree-of-freedom (SDOF) example, the accuracy and efficiency of the IFORM approach is assessed, revealing that the IFORM methods provide good estimates using a reasonable amount of short-term response calculations.

Paper III

Although the IFORM approach proposed in Paper II represent an efficient approximation for the long-term extreme response, there is more to gain with respect to the accuracy of the approximation. In Paper III, the second order reliability method (SORM) is used to improve the accuracy of the approximation, resulting in a novel inverse SORM (ISORM) approach. Using the same SDOF example as in Paper II, the ISORM method is seen to achieve significantly improved accuracy, yet keep the number of required short-term response analyses within acceptable levels.

Paper IV

Due to the very large number of structural response analyses traditionally needed for a full long-term analysis, the computational effort is usually considered to increase above acceptable levels for complex structures such as floating bridges. However, utilizing the IFORM and ISORM approaches developed in Paper II and Paper III, the full long-term approach is made feasible also for complex structures. In addition, the method proposed in Paper I can further reduce the computational effort. In Paper IV, the developments of the first three papers are demonstrated for a long-span pontoon bridge subjected to wave loads.

1.8 Conclusion

1.8.1 Concluding remarks

The work presented in this thesis has contributed to the development of more efficient, yet accurate, methods for full long-term extreme response analysis. Hopefully, this contribution will make full long-term analyses feasible and available for the design of complex marine structures, such as e.g. floating bridges.

In Paper I (Chapter 2), a new method was presented for the calculation of auto- and cross-spectral densities in the stochastic modelling of ocean waves and wave loads, based on a series expansion solution of the integral expressing the cross-spectral density. The method was developed for first order wave excitation loads, but it is readily extended to the computation of other cross-spectral densities, e.g. for wave elevation, wave kinematics or second order load. The only difference will be which transfer functions that are used. The accuracy of the new method was verified, and using two floating bridge examples, it was demonstrated that the new method provides a significant improvement in computational efficiency.

In Paper II (Chapter 3), an exact and an approximate formulation for the long-term extreme response of marine structures, cf. Eqns. (1.4) and (1.5) respectively, were discussed and compared. It was shown that the approximate formulation underestimates the long-term extreme response values. It was also shown how both formulations can be solved in an approximate manner using FORM, and how characteristic extreme response values can be obtained by IFORM. Furthermore, a new solution algorithm for the IFORM problem was proposed, resolving some convergence issues of an iteration algorithm given in the literature. The different approximations for the long-term extreme response were compared for an SDOF example, revealing that the IFORM approximations give reasonably good estimates for the long-term extreme response. The number of required short-term response analyses for the IFORM method was found to be within acceptable limits.

In Paper III (Chapter 4), the inverse FORM solution from Chapter 3 was improved by use of SORM, resulting in an inverse SORM method. In order to find the extreme response using inverse reliability methods, an upper tail approximation depending on a parameter C was introduced. Considering the SDOF example from Paper II (Chapter 3), the ISORM method was

seen to give significantly improved accuracy, especially with the parameter C chosen as some large value.

Finally, in Paper IV (Chapter 5), a framework for full long-term extreme response analysis of marine structures was demonstrated for a long-span case study floating bridge. This framework is based on the methods developed in Papers I-III. The presented numerical results revealed that the characteristic extreme response could be calculated in an efficient and accurate manner. Especially the ISORM method provided high accuracy. The full long-term analysis was also compared with the environmental contour method, which is much used in practical design. It was recognized that the environmental contour method could be calibrated by comparison with the IFORM and ISORM results.

1.8.2 Recommendations for future work

The primary goal of this work has been to develop of more efficient, yet accurate, methods for full long-term extreme response analysis of marine structures. The hope is that the presented methods will be put into use in practical design. The application to floating bridges has been used as an example throughout this thesis. However, the methodology is presented in a general setting, and many other types of applications could benefit from this work. It would, for instance, be interesting to see the application of the methods to offshore wind turbines.

The presented methods have been demonstrated for a complex structure by the case study of a long-span pontoon bridge. Still, it is relatively simple frequency domain approaches for the short-term response that have been used. It would be interesting to validate the efficiency of the proposed methods in combination with e.g. time domain methods for non-linear response.

With regard to further development of the methods presented in this thesis, it could be interesting to investigate the use of other ISORM methods [49]. These methods are more sophisticated, using an exact expression for the quadratic approximation rather than the asymptotic expression which is used in Section 4.2.2. For the estimation of extreme response it is expected that the asymptotic expression is sufficiently accurate, but other ISORM methods could potentially further reduce the computational effort.

Paper I:

CHAPTER 2

Efficient computation of cross-spectral densities in the stochastic modelling of waves and wave loads

Finn-Idar G. Giske, Bernt J. Leira, Ole Øiseth

Published in *Applied Ocean Research* 62(2017), pp. 70-88.
doi:10.1016/j.apor.2016.11.007

Abstract

A new method is presented for efficient calculation of auto- and cross-spectral densities in the stochastic modelling of ocean waves and wave loads. As part of the short-term response analyses, the method may contribute to more efficient long-term response prediction. Specifically the cross-spectral densities of the first order wave excitation forces are considered, but the method is straightforwardly generalized to other cross-spectral densities, e.g. for wave elevation, wave kinematics or second order loads. The method can be used with any choice of directional spreading function, but special attention is given to the commonly used cos-2s type directional distribution. In addition to the development of the new method, the traditional method using the trapezoidal rule for numerical quadrature is improved by developing an adaptive way of choosing the number of integration points. The accuracy of the adaptive method and the new method is investigated, revealing rapid convergence for both methods. However, the new method appears more robust as it avoids so-called spurious hat errors. When applied to two different pontoon type floating bridges the adaptive method and the new method both achieve a great improvement in computational effort compared to the traditional trapezoidal rule method. When the dimensions of the floating bridge increase, i.e. the number of pontoons and their relative distances increase, the new method is superior with respect to computation time.

2.1 Introduction

For the assessment of extreme responses needed in the design of marine structures a full long-term response analysis is the most accurate approach [60, 68], and for fatigue design it is usually required [51, 60]. In the long-term approach structural response analyses have to be carried out for a large number of sea states, which can be very time-consuming. Over the last decade new methods have been developed making long-term analysis more efficient, either by reducing the number of required short-term analyses [68, 75] or by computing the relevant short-term quantities more efficiently [58]. In the short-term response analysis of marine structures the auto- and cross-spectral densities of the wave load are important quantities, and their computation may contribute significantly to the computation time, for instance when the power spectral density method [42] is applied. The method proposed in this paper contributes to more efficient short-term analyses by making the evaluation of auto- and cross-spectral densities more efficient.

When the sea surface is modelled as a stochastic process the cross-spectral density between the wave elevations at the points (x_m, y_m) and (x_n, y_n) can be written as

$$S_{mn}(\omega) = \int_{-\pi}^{\pi} e^{i\kappa(\omega)L\cos(\beta-\theta)} S_{\eta\eta}^{(2)}(\theta,\omega)\, d\theta, \tag{2.1}$$

where $\kappa(\omega)$ is the wave number and $S_{\eta\eta}^{(2)}(\theta,\omega)$ denotes the directional wave spectrum [63]. β and L are constants that depend on the spatial separations $\Delta x = x_m - x_n$ and $\Delta y = y_m - y_n$, see Section 2.2.3 for definitions. In [66] a series expansion solution of the integral (2.1) is found by expressing the directional spectrum as a Fourier series and solving the integral term-by-term using Bessel functions, see also Section 7.2.1 of [63]. This series expansion is then used to obtain equations for the unknown Fourier coefficients of the directional spectrum such that these can be evaluated from measured cross-spectral densities. This paper deals with the reverse problem, as the aim is to evaluate the cross-spectral densities when a theoretical model for the directional spectrum is assumed.

A consistent stochastic theory of ocean waves and wave loading processes is presented in [71], which have been applied for offshore structures [70, 72] and floating bridges [19, 41, 42, 44, 45]. In this context calculation of the cross-spectral densities requires computation of integrals similar to (2.1),

which can be written in the form

$$\int_{-\pi}^{\pi} f(\theta) e^{i\kappa(\omega) L \cos\theta} d\theta, \tag{2.2}$$

for some function $f(\theta)$. In applications these integrals have traditionally been evaluated using straightforward numerical quadrature [19, 44]. This requires care with respect to the number of integration points, because too few integration points may result in errors referred to as spurious hats [44]. The reason why these spurious hats occur is that when the factor $\kappa(\omega)L$ in (2.2) is large, the integral becomes highly oscillatory. It is worth mentioning that general methods for numerical quadrature of highly oscillatory integrals do exist [34, 64]. However, these methods are quite complex, especially for oscillatory integrals with stationary points like (2.2). Also, a more specialised computation method is expected to be more efficient.

In the present paper a new method is developed for the calculation of cross-spectral densities in the stochastic modelling of ocean waves and wave loads. The series expansion solution of (2.1) found in [63, 66] is first generalized to the case of cross-spectral densities of first order wave excitation forces, and then utilized as a computational method for the cross-spectral densities. The method may readily be generalized to other cross-spectral densities, e.g. for wave elevation, wave kinematics or second order loads by using different transfer functions.

The new method will apply to any directional distribution expressed as a Fourier series. The Fourier coefficients of various theoretical models of the directional distribution can be found in [40] or in Section 2.5 of [28]. For the sake of completeness this paper includes a derivation of the Fourier coefficients of the *cos-2s* directional distribution in the most general case where s is any positive real number, thus providing a proof of the Fourier coefficients stated in [28, 40].

In addition to the development of the new method, the traditional method using the trapezoidal rule for numerical quadrature is improved by developing an adaptive way of choosing the number of integration points. This adaptive trapezoidal rule method is developed by observing when the spurious hats occur. The accuracy and efficiency is investigated for both the adaptive trapezoidal rule method and the new series expansion method. Finally the performances of the methods are compared when applied to pontoon type floating bridges.

2.2 Review of the stochastic modelling of ocean waves

2.2.1 Cross-spectral density

A common approach when modelling wind generated waves for engineering purposes is to assume that the sea elevation is a homogeneous stationary stochastic process [71]. The sea elevation at the point (x, y) at time t, denoted $\eta(x, y, t)$, is then written as

$$\eta(x, y, t) = \int_{-\infty}^{\infty} e^{i\omega t - i\kappa(x\cos\theta + y\sin\theta)} dB(\boldsymbol{\kappa}, \omega), \tag{2.3}$$

where $\boldsymbol{\kappa} = [\kappa\cos\theta, \kappa\sin\theta]$ is the wave number vector, ω is the frequency and $B(\boldsymbol{\kappa}, \omega)$ is the spectral process associated with the wave elevation. By further assuming the existence of a dispersion relation which relates the frequency ω and the wave number κ by a one-to-one mapping $\kappa = \kappa(\omega)$, or equivalently $\omega = \omega(\kappa)$, the cross-spectral density between the wave elevation at two points (x_m, y_m) and (x_n, y_n) can be expressed by

$$S_{mn}(\omega) = \int_{\theta} e^{-i\kappa(\omega)(\Delta x\cos\theta + \Delta y\sin\theta)} S^{(2)}_{\eta\eta}(\theta, \omega)\, d\theta,$$

where $\Delta x = x_m - x_n$ and $\Delta y = y_m - y_n$ is the separation of the locations (x_m, y_m) and (x_n, y_n) in space. $S^{(2)}_{\eta\eta}(\theta, \omega)$ is the directional wave spectral density. The details of the derivation is given in Section 2.A as well as in [71]. According to the Airy wave theory, or linear wave theory, the dispersion relation takes the form

$$\omega^2 = \kappa g \tanh(\kappa d), \qquad \omega, \kappa \geq 0,$$

with water depth d and gravitational acceleration g, defining the function $\kappa(\omega)$ implicitly.

The directional wave spectral density $S^{(2)}_{\eta\eta}(\theta, \omega)$ is frequently written as $S^{(2)}_{\eta\eta}(\theta, \omega) = S_{\eta\eta}(\omega)\,\Psi(\theta, \omega)$ and thus separated into a one-dimensional wave spectral density $S_{\eta\eta}(\omega)$ and a spreading function $\Psi(\theta, \omega)$. The spreading function is sometimes assumed to be a function of the direction θ only, but such an assumption is not done here. For an overview of the various theoretical models for $S_{\eta\eta}(\omega)$ and $\Psi(\theta, \omega)$ see e.g. [28, 73]. The cross-spectral density can now be written as

$$S_{mn}(\omega) = S_{\eta\eta}(\omega) \int_{-\pi}^{\pi} \Psi(\theta, \omega)\, e^{-i\kappa(\omega)(\Delta x\cos\theta + \Delta y\sin\theta)} d\theta. \tag{2.4}$$

2.2.2 Auto-spectral density and complex coherency

If we consider the case $m = n$, we have that $\Delta x = \Delta y = 0$, and (2.4) gives an expression for the auto-spectral density

$$S_{nn}(\omega) = S_{\eta\eta}(\omega) \int_{-\pi}^{\pi} \Psi(\theta, \omega)\, d\theta. \tag{2.5}$$

Since the wave elevation is assumed to be homogeneous, the auto-spectral density should be equal to the one-dimensional wave spectral density at any point (x_n, y_n). This imposes the following normalization of the spreading function:

$$\int_{-\pi}^{\pi} \Psi(\theta, \omega)\, d\theta = 1. \tag{2.6}$$

The complex coherency is defined in terms of auto- and cross-spectral densities as

$$\gamma_{mn}(\omega) = \frac{S_{mn}(\omega)}{\sqrt{S_{nn}(\omega) S_{mm}(\omega)}}.$$

Combining equations (2.4), (2.5) and (2.6), we find that the complex coherency is given by

$$\gamma_{mn}(\omega) = \frac{S_{mn}(\omega)}{S_{\eta\eta}(\omega)} = \int_{-\pi}^{\pi} \Psi(\theta, \omega)\, e^{-i\kappa(\omega)(\Delta x \cos\theta + \Delta y \sin\theta)} d\theta. \tag{2.7}$$

The complex coherency is favourable to deal with in computations because it is dimensionless, independent of the one-dimensional spectral density and it satisfies $|\gamma_{mn}(\omega)| \leq 1$. For this reason most of the derivations in this paper will deal with the complex coherency rather than the cross-spectral density. The cross-spectral density can always be obtained from the complex coherency and the auto-spectral densities by

$$S_{mn}(\omega) = \gamma_{mn}(\omega) \sqrt{S_{nn}(\omega) S_{mm}(\omega)}.$$

2.2.3 Directional distribution function

The spreading function $\Psi(\theta, \omega)$ is commonly given as a distribution around a mean wave direction, in which case it is written as

$$\Psi(\theta, \omega) = D(\theta - \bar{\theta}, \omega), \tag{2.8}$$

where $\bar{\theta}$ is the mean wave direction and $D(\phi, \omega)$ is the directional distribution function centred around zero. The directional distribution function is 2π-periodic and according to (2.6) it should integrate to one over one period. By inserting (2.8) into (2.7), using the periodicity of $D(\phi, \omega)$, the complex coherency can be expressed in terms of the directional distribution by

$$\gamma_{mn}(\omega) = \int_{-\pi}^{\pi} D(\phi, \omega)\, e^{-i\kappa(\omega)\left(\Delta x \cos\left(\phi+\bar{\theta}\right)+\Delta y \sin\left(\phi+\bar{\theta}\right)\right)} d\phi.$$

The linear combination of sine and cosine in the expression above can be written in terms of a single harmonic function as

$$\begin{aligned} &-\Delta x \cos\left(\phi+\bar{\theta}\right) - \Delta y \sin\left(\phi+\bar{\theta}\right) \\ &\qquad = \sqrt{\Delta x^2 + \Delta y^2} \cos\left(\phi + \bar{\theta} + \pi - \operatorname{atan2}(\Delta y, \Delta x)\right), \end{aligned}$$

where $\operatorname{atan2}(\Delta y, \Delta x)$ is the generalization of $\arctan(\Delta y/\Delta x)$ that covers the entire circular range. If we then define

$$\begin{aligned} L &= \sqrt{\Delta x^2 + \Delta y^2}, \\ \beta &= \bar{\theta} + \pi - \operatorname{atan2}(\Delta y, \Delta x), \end{aligned}$$

we obtain

$$\gamma_{mn}(\omega) = \int_{-\pi}^{\pi} D(\phi, \omega)\, e^{i\kappa(\omega) L \cos(\phi+\beta)} d\phi = \int_{-\pi+\beta}^{\pi+\beta} D(\theta-\beta, \omega)\, e^{i\kappa(\omega) L \cos\theta} d\theta,$$

where the integrand is 2π-periodic. Thus the complex coherency is finally given as

$$\gamma_{mn}(\omega) = \int_{-\pi}^{\pi} D(\theta-\beta, \omega)\, e^{i\kappa(\omega) L \cos\theta} d\theta. \tag{2.9}$$

2.2.4 Series expansion of the complex coherency

Expressing the directional distribution function $D(\phi, \omega)$ as a Fourier series in ϕ, the integral (2.9) can be solved in terms of Bessel functions using the same approach as in [66], which is also given in Section 7.2.1 of [63].

Let the directional distribution function be given by the Fourier series

$$D(\phi, \omega) = \sum_{k=-\infty}^{\infty} c_k(\omega) e^{ik\phi}. \tag{2.10}$$

Since the directional distribution is a real function, the Fourier coefficients are required to satisfy $c_{-k}(\omega) = \overline{c_k(\omega)}$ for $k \geq 0$, the overline denoting complex conjugation. Using this Fourier expansion in the expression (2.9) for the complex coherency yields

$$\gamma_{mn}(\omega) = \sum_{k=-\infty}^{\infty} c_k(\omega) e^{-ik\beta} \int_{-\pi}^{\pi} e^{ik\theta} e^{i\kappa(\omega)L\cos\theta} d\theta \tag{2.11}$$

where we have assumed that the order of summation and integration can be interchanged. The integrals in the above expression can be solved in terms of Bessel functions by utilizing the integral representation 9.1.21 in [1] stating that

$$J_k(z)\,\pi i^k = \int_0^{\pi} e^{iz\cos\theta} \cos(k\theta)\, d\theta,$$

where $J_k(z)$ is the Bessel function of the first kind with integer order k. Specifically we find that

$$\begin{aligned}
\int_{-\pi}^{\pi} e^{ik\theta} e^{i\kappa(\omega)L\cos\theta} d\theta &= \int_{-\pi}^{\pi} e^{i\kappa(\omega)L\cos\theta} \cos(k\theta)\, d\theta \\
&\quad + i \int_{-\pi}^{\pi} e^{i\kappa(\omega)L\cos\theta} \sin(k\theta)\, d\theta \\
&= 2\int_0^{\pi} e^{i\kappa(\omega)L\cos\theta} \cos(k\theta)\, d\theta \\
&= 2J_k(\kappa(\omega)L)\,\pi i^k,
\end{aligned}$$

which inserted into (2.11) yields the following series expansion of the complex coherency:

$$\gamma_{mn}(\omega) = 2\pi \sum_{k=-\infty}^{\infty} c_k(\omega) i^k e^{-ik\beta} J_k(\kappa(\omega)L). \tag{2.12}$$

2.2.5 Directional distribution of the *cos-2s* type

The most commonly used directional distribution is given by

$$D(\phi,\omega) = \frac{2^{2s(\omega)}\Gamma^2(s(\omega)+1)}{2\pi\Gamma(2s(\omega)+1)} \cos^{2s(\omega)}\frac{\phi}{2}, \qquad \phi \in [-\pi,\pi), \tag{2.13}$$

where $\Gamma(\cdot)$ denotes the gamma function and $s(\omega)$ is a non-negative real valued function. This type of directional distribution was originally proposed by [50] and was developed further by [54] and [27] who investigated

frequency dependence through the spreading parameter $s(\omega)$. Although in applications $s(\omega)$ is frequently assumed constant, wave data reveals a strong frequency dependence [40]. Throughout this paper the spreading parameter $s(\omega)$ is assumed to be a function of frequency. Note, however, that the ω-dependency will not be written explicitly as in (2.13) for simplicity of notation.

In order to make $D(\phi,\omega)$ as given by (2.13) a 2π-periodic function in ϕ for any $s \geq 0$, it should rather be written as

$$D\left(\phi,\omega\right) = \frac{2^{2s}\Gamma^2\left(s+1\right)}{2\pi\Gamma\left(2s+1\right)}\left(\cos^2\frac{\phi}{2}\right)^s, \qquad \phi \in \mathbb{R}. \tag{2.14}$$

If we rewrite $\cos^2\frac{\phi}{2} = \frac{1}{2}(1+\cos\phi)$ it is clear that this directional distribution is 2π-periodic. Writing $D(\phi,\omega)$ in this way rather than as in (2.13) will also ensure that $D(\phi,\omega)$ is real and non-negative at any ϕ for any choice of s. Now for an arbitrary non-negative real number s, the following identity holds according to Theorem 1 in Section 2.B.

$$\left(\cos^2\frac{\phi}{2}\right)^s = \frac{1}{2^{2s}}\frac{\Gamma\left(2s+1\right)}{\Gamma^2\left(s+1\right)} + \frac{1}{2^{2s-1}}\sum_{k=1}^{\infty}\frac{\Gamma\left(2s+1\right)}{\Gamma\left(s-k+1\right)\Gamma\left(s+k+1\right)}\cos\left(k\phi\right), \tag{2.15}$$

Using this identity the directional distribution (2.14) can be written

$$\begin{aligned} D\left(\phi,\omega\right) &= \frac{1}{2\pi} + \frac{1}{\pi}\sum_{k=1}^{\infty}\frac{\Gamma^2\left(s+1\right)}{\Gamma\left(s-k+1\right)\Gamma\left(s+k+1\right)}\cos\left(k\phi\right) \\ &= \frac{1}{2\pi}\sum_{k=-\infty}^{\infty}\frac{\Gamma^2\left(s+1\right)}{\Gamma\left(s-k+1\right)\Gamma\left(s+k+1\right)}e^{ik\phi}, \end{aligned}$$

which is recognized as a Fourier series of the form (2.10) where

$$c_k(\omega) = \frac{1}{2\pi}\frac{\Gamma^2\left(s+1\right)}{\Gamma\left(s-k+1\right)\Gamma\left(s+k+1\right)}, \qquad k \in \{0,\pm1,\pm2,\ldots\}. \tag{2.16}$$

These Fourier coefficients agrees with those stated in [28, 40]. This derivation of the Fourier coefficients of the directional distribution (2.13) generalizes the derivation found in Section 7.2.1 of [63] which is valid for integer s.

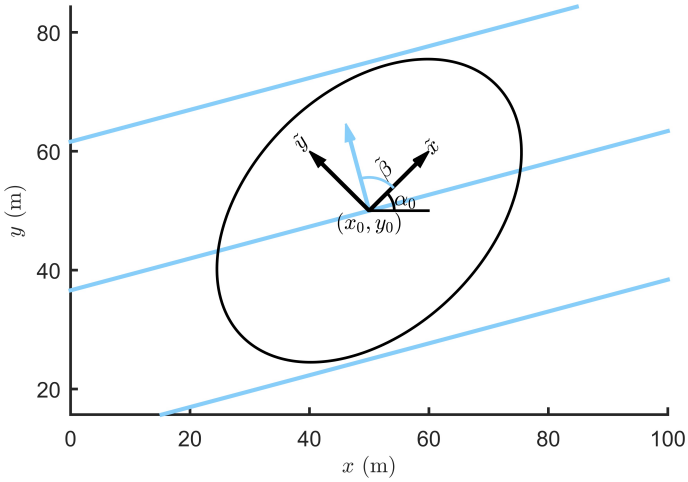

Figure 2.1: Local coordinate system of a rigid body and definition of wave propagation direction.

2.3 Stochastic modelling of first order wave excitation loads

2.3.1 Exciting forces and moments on a rigid body

The hydrodynamic forces on a floating body can be decomposed into two parts, the wave excitation forces and the motion induced forces. We will now look at how the wave excitation forces can be modelled as a stochastic process. Consider a rigid body with a local coordinate system $(\tilde{x}, \tilde{y})$ which is located with its origin at the point (x_0, y_0) and rotated counterclockwise with an angle α_0 relative to the global coordinate system (x, y) as shown in Fig. 2.1. Thus (x_0, y_0) and α_0 specifies the location and orientation of the body. With this definition the global and local coordinates are related by

$$\begin{bmatrix} x \\ y \end{bmatrix} = \begin{bmatrix} x_0 + \tilde{x}\cos\alpha_0 - \tilde{y}\sin\alpha_0 \\ y_0 + \tilde{x}\sin\alpha_0 + \tilde{y}\cos\alpha_0 \end{bmatrix}. \tag{2.17}$$

Within the framework of linear potential theory, the hydrodynamic forces on a body of arbitrary shape can be computed using a panel method as implemented in software such as WAMIT [76] or WADAM [15]. The wave excitation forces are then reported in terms of the complex transfer function from the wave elevation to the wave load. This means that for a regular

incident wave of amplitude A given in local coordinates by

$$\eta(\tilde{x},\tilde{y},t) = A\exp\left\{i\omega t - i\kappa\left(\tilde{x}\cos\tilde{\beta}+\tilde{y}\sin\tilde{\beta}\right)\right\}, \tag{2.18}$$

the forces and moments due to this wave will be given by $A\tilde{\boldsymbol{f}}_0(\tilde{\beta},\omega)e^{i\omega t}$, where $\tilde{\boldsymbol{f}}_0(\tilde{\beta},\omega)$ is the complex transfer function. Here $\tilde{\beta}$ is the wave propagation direction given as the angle relative to the $\tilde{x}$-axis, see Fig. 2.1. The vector $\tilde{\boldsymbol{f}}_0$ contains six components, the transfer functions for three forces and three moments.

Provided the load due to any regular wave, the excitation load for the irregular wave (2.3) can be obtained by superposition. Inserting the relation (2.17) into (2.3) yields the sea elevation referring to the local coordinates of the body:

$$\eta\left(\tilde{x},\tilde{y},t\right) = \int_{-\infty}^{\infty} e^{i\omega t - i\kappa(\tilde{x}\cos(\theta-\alpha_0)+\tilde{y}\sin(\theta-\alpha_0))}e^{-i\kappa(x_0\cos\theta+y_0\sin\theta)}dB\left(\kappa,\omega\right). \tag{2.19}$$

Now since θ is the wave propagation direction relative to the global x-axis, we see from Fig. 2.1 that $\alpha_0+\tilde{\beta}=\theta$ which means that $\theta-\alpha_0$ can be identified as the local wave propagation direction $\tilde{\beta}$ in (2.18). Thus the first exponential in the above expression is recognized as the exponential of the incident wave (2.18). Hence (2.19) can be considered as a linear combination of (infinitely many) regular waves of amplitude $dB(\kappa,\omega)$ and, assuming the linear operations of calculating the wave load and taking the integral can be interchanged, we obtain an expression for the wave excitation load due to the irregular wave (2.3):

$$\tilde{\boldsymbol{q}}_0\left(t\right) = \int_{-\infty}^{\infty} \tilde{\boldsymbol{f}}_0\left(\theta-\alpha_0,\omega\right)e^{i\omega t-i\kappa(x_0\cos\theta+y_0\sin\theta)}dB\left(\kappa,\omega\right).$$

This expression gives the loads referring to the local coordinate system of the body, but the loads referring to the global coordinates are easily obtained by a linear transformation

$$\boldsymbol{q}_0\left(t\right) = \boldsymbol{T}_0\tilde{\boldsymbol{q}}_0\left(t\right) = \int_{-\infty}^{\infty} \boldsymbol{f}_0\left(\theta-\alpha_0,\omega\right)e^{i\omega t-i\kappa(x_0\cos\theta+y_0\sin\theta)}dB\left(\kappa,\omega\right). \tag{2.20}$$

where $\boldsymbol{T}_0$ is the transformation matrix and $\boldsymbol{f}_0=\boldsymbol{T}_0\tilde{\boldsymbol{f}}_0$.

2.3.2 Cross-spectral densities for wave excitation loads

We now consider the wave excitation loads for N bodies at the locations $(x_1, y_1), (x_2, y_2), \ldots, (x_N, y_N)$, with orientation angles $\alpha_1, \alpha_2, \ldots, \alpha_N$ relative to the global x-axis. The loads are conveniently organized into a total load vector

$$\boldsymbol{q} = \begin{bmatrix} \boldsymbol{q}_1^T & \boldsymbol{q}_2^T & \cdots & \boldsymbol{q}_N^T \end{bmatrix}^T.$$

Here $\boldsymbol{q}_n$ refers to the wave excitation loads on body number n which are given by (2.20) using the transfer function $\boldsymbol{f}_n$ corresponding to the body. Because each vector $\boldsymbol{q}_n$ contains six components, the total number of components in $\boldsymbol{q}$ will be $6N$. Each individual component can therefore be denoted by q_ν, where $\nu \in \{1, 2, \ldots, 6N\}$. Organizing the transfer functions $\boldsymbol{f}_n$ in the same manner, the individual loads are obtained from (2.20) as

$$q_\nu(t) = \int_{-\infty}^{\infty} f_\nu(\theta - \alpha_n, \omega)\, e^{i\omega t - i\kappa(x_n \cos\theta + y_n \sin\theta)} dB(\kappa, \omega). \tag{2.21}$$

The body number n corresponding to the index ν is given by $n = \lceil \nu/6 \rceil$, where $\lceil \cdot \rceil$ denotes the ceiling function giving the smallest integer not less than the argument.

Using the formulation (2.21) as starting point, the same derivation as in Section 2.2.1 can be carried out, yielding the cross-spectral density between the loads q_μ and q_ν as

$$\begin{aligned} &\frac{S_{q_\mu q_\nu}(\omega)}{S_{\eta\eta}(\omega)} \\ &= \int_{-\pi}^{\pi} \Psi(\theta, \omega)\, f_\mu(\theta - \alpha_m, \omega) \overline{f_\nu(\theta - \alpha_n, \omega)} e^{-i\kappa(\omega)(\Delta x \cos\theta + \Delta y \sin\theta)} d\theta, \end{aligned} \tag{2.22}$$

where the overline denotes complex conjugation.

2.3.3 Series expansion of the complex coherency

Using the same approach as in Section 2.2.3, the expression (2.22) for the cross-spectral density can be written as

$$\frac{S_{q_\mu q_\nu}(\omega)}{S_{\eta\eta}(\omega)} = \int_{-\pi}^{\pi} D(\theta-\beta,\omega) f_\mu\left(\theta-\beta+\bar{\theta}-\alpha_m,\omega\right)\overline{f_\nu\left(\theta-\beta+\bar{\theta}-\alpha_n,\omega\right)} e^{i\kappa L\cos\theta} d\theta. \tag{2.23}$$

Now the transfer functions are usually known only by their values at a finite number of heading angles. Then in order to perform the integration (2.23) we can use functions $f_\mu(\theta,\omega)$ that interpolates the transfer functions at the given values of the heading angle θ. For our purposes it is convenient to use trigonometric interpolation [31, 38], which means that the transfer functions are given by trigonometric polynomials

$$f_\mu(\theta,\omega) = \sum_{k=-N_f}^{N_f} a_k^\mu(\omega)\, e^{ik\theta}. \tag{2.24}$$

If the transfer function values are given at heading angles uniformly distributed between 0 and 2π, the coefficients $a_k^\mu(\omega)$ can be efficiently computed using fast Fourier transform (FFT). If the number of heading angles is N_θ we have that $N_f = \lfloor N_\theta/2 \rfloor$.

With transfer functions given by (2.24) we find that

$$f_\mu\left(\phi+\bar{\theta}-\alpha_m,\omega\right) = \sum_{k=-N_f}^{N_f}\left(e^{ik\left(\bar{\theta}-\alpha_m\right)} a_k^\mu(\omega)\right) e^{ik\phi}$$

and

$$\begin{aligned}\overline{f_\nu\left(\phi+\bar{\theta}-\alpha_n,\omega\right)} &= \sum_{k=-N_f}^{N_f}\left(\overline{e^{ik\left(\bar{\theta}-\alpha_n\right)} a_k^\nu(\omega)}\right) e^{-ik\phi} \\ &= \sum_{k=-N_f}^{N_f}\left(\overline{e^{-ik\left(\bar{\theta}-\alpha_n\right)} a_{-k}^\nu(\omega)}\right) e^{ik\phi}.\end{aligned}$$

With a directional distribution given by (2.10) we have then available the individual Fourier series of each of the factors in the product

$$D(\phi,\omega)f_\mu\left(\phi+\bar{\theta}-\alpha_m,\omega\right)\overline{f_\nu\left(\phi+\bar{\theta}-\alpha_n,\omega\right)}.$$

It can be shown that the Fourier coefficients of a product can be obtained by taking the convolution of the Fourier coefficients of the factors. Thus we are able to find coefficients $C_k^{\mu\nu}(\omega)$ such that

$$D(\phi,\omega)f_\mu\left(\phi+\bar{\theta}-\alpha_m,\omega\right)\overline{f_\nu\left(\phi+\bar{\theta}-\alpha_n,\omega\right)}=\sum_{k=-\infty}^{\infty}C_k^{\mu\nu}\left(\omega\right)e^{ik\phi}. \quad (2.25)$$

Having the product $D(\phi,\omega)f_\mu\left(\phi+\bar{\theta}-\alpha_m,\omega\right)\overline{f_\nu\left(\phi+\bar{\theta}-\alpha_n,\omega\right)}$ developed as a Fourier series in ϕ makes the derivation of the series expansion (2.12) from Section 2.2.4 directly applicable. Inserting the Fourier expansion (2.25) into (2.23) yields the cross-spectral densities

$$S_{q_\mu q_\nu}(\omega)=2\pi S_{\eta\eta}\left(\omega\right)\sum_{k=-\infty}^{\infty}C_k^{\mu\nu}(\omega)i^k e^{-ik\beta}J_k\left(\kappa(\omega)L\right). \quad (2.26)$$

In the special case that the Fourier series of the directional distribution is finite, it can be written as

$$D\left(\phi,\omega\right)=\sum_{k=-N_D}^{N_D}c_k\left(\omega\right)e^{ik\phi},$$

and the series expansion (2.26) will be finite. Specifically we have then that

$$S_{q_\mu q_\nu}(\omega)=2\pi S_{\eta\eta}\left(\omega\right)\sum_{k=-N_{\mathrm{tot}}}^{N_{\mathrm{tot}}}C_k^{\mu\nu}(\omega)i^k e^{-ik\beta}J_k\left(\kappa(\omega)L\right),$$

where $N_{\mathrm{tot}}=2N_f+N_D$.

It is worth noticing that for the cross-spectral densities between loads at the same location we have that $m=n$ and thus $L=0$. Using the fact that $J_k(0)=0$ for $k\in\{\pm1,\pm2,\dots\}$ and $J_0(0)=1$ yields the result

$$S_{q_\mu q_\nu}(\omega)=2\pi S_{\eta\eta}\left(\omega\right)C_0^{\mu\nu}(\omega),$$

which holds whenever $m = n$, or equivalently $\lceil \mu/6 \rceil = \lceil \nu/6 \rceil$. The auto-spectral densities are thus given by

$$S_{q_\mu q_\mu}(\omega) = 2\pi S_{\eta\eta}(\omega) C_0^{\mu\mu}(\omega), \tag{2.27}$$

which gives the following formula for the complex coherencies:

$$\gamma_{q_\mu q_\nu}(\omega) = \frac{S_{q_\mu q_\nu}(\omega)}{\sqrt{S_{q_\mu q_\mu}(\omega) S_{q_\nu q_\nu}(\omega)}} = \sum_{k=-\infty}^{\infty} \frac{C_k^{\mu\nu}(\omega)}{\sqrt{C_0^{\mu\mu}(\omega) C_0^{\nu\nu}(\omega)}} i^k e^{-ik\beta} J_k(\kappa(\omega) L). \tag{2.28}$$

2.4 Computational methods for the complex coherencies

2.4.1 Approximation by the trapezoidal rule

By definition the complex coherencies are given by

$$\gamma_{q_\mu q_\nu}(\omega) = \frac{S_{q_\mu q_\nu}(\omega)}{\sqrt{S_{q_\mu q_\mu}(\omega) S_{q_\nu q_\nu}(\omega)}} = \frac{S_{q_\mu q_\nu}(\omega)/S_{\eta\eta}(\omega)}{\sqrt{S_{q_\mu q_\mu}(\omega)/S_{\eta\eta}(\omega)} \sqrt{S_{q_\nu q_\nu}(\omega)/S_{\eta\eta}(\omega)}}.$$

Inserting the expression (2.22) yields

$$\gamma_{q_\mu q_\nu}(\omega) = \frac{\int_{-\pi}^{\pi} \Psi(\theta,\omega) f_\mu(\theta - \alpha_m, \omega) \overline{f_\nu(\theta - \alpha_n, \omega)} e^{-i\kappa(\omega)(\Delta x \cos\theta + \Delta y \sin\theta)} d\theta}{\sqrt{\int_{-\pi}^{\pi} \Psi(\theta,\omega) |f_\mu(\theta - \alpha_m, \omega)|^2 d\theta \int_{-\pi}^{\pi} \Psi(\theta,\omega) |f_\nu(\theta - \alpha_n, \omega)|^2 d\theta}}. \tag{2.29}$$

We denote by $\widetilde{\gamma_{q_\mu q_\nu}}(\omega)$ the approximation obtained when the above expression is computed using the trapezoidal rule with $\tilde{N}$ integration points. Traditionally, the number of integration points $\tilde{N}$ is chosen to be the same for all values of μ, ν and ω, this will be referred to as the traditional trapezoidal rule method. As we will see the number of integration points should rather be adapted according to the value of ω, this will be referred to as the adaptive trapezoidal rule method.

We now consider two pontoons located at the points $(x_1, y_1) = (0, 0)$ and $(x_2, y_2) = (L, 0)$ with orientations $\alpha_1 = \alpha_2 = \pi/2$. The indices referring to the pontoon numbers are thus $m, n \in \{1, 2\}$ and the global indices are

$\mu, \nu \in \{1, 2, \ldots, 12\}$. The coherency matrix will then be a 12-by-12 matrix whose elements are $\gamma_{q_\mu q_\nu}(\omega)$. The transfer functions of the pontoons are evaluated by the software WADAM [15] at 36 different heading angles, so the transfer functions $f_\mu(\theta, \omega)$ are given by (2.24) with $N_f = 18$. The spreading function $\Psi(\theta, \omega)$ is given by a directional distribution of the *cos-2s* type as described in Section 2.2.5 with a constant spreading parameter $s(w) = s$. Note, however, that the methods described will be equally applicable for other directional distributions.

Figures 2.2 and 2.3 show the resulting coherence functions $|\widetilde{\gamma_{q_1 q_7}}(\omega)|$ when the complex coherency $\widetilde{\gamma_{q_1 q_7}}(\omega)$ is computed using the traditional trapezoidal rule method for different distances L between the pontoons. The mean wave direction is $\bar{\theta} = \pi/2$ and the spreading parameter is $s = 1$ in Fig. 2.2, and $s = 20$ in Fig. 2.3. Figures 2.2 and 2.3 demonstrate that relatively large errors may occur if the number of integrations points $\tilde{N}$ is not large enough. These errors are the same as the spurious hats observed in [44]. The spurious hats can be explained by observing that the factor $\exp\{-i\kappa(\omega)(\Delta x \cos\theta + \Delta y \sin\theta)\}$ will make the upper integral in (2.29) highly oscillatory when the value of $\kappa(\omega)\sqrt{\Delta x^2 + \Delta y^2} = \kappa(\omega)L$ is large, and therefore the trapezoidal rule with $\tilde{N}$ integration points will be far too crude an approximation. Large values of $\kappa(\omega)$ occur when ω is large. When we consider $L \leq 1000$ m and $\omega \leq 4$ rad/s as in Figs. 2.2 and 2.3, we have that the maximal value of $\kappa(\omega)L$ is $(\kappa L)_{max} = 1631.5$. When the number of integration points $\tilde{N}$ is slightly larger than this, we observe that the spurious hats do not occur. Indeed if we plot the line defined by $\kappa(\omega)L = \tilde{N}$ along with the coherence function as in Fig. 2.4 we see that the spurious hats starts occurring when the value of $\kappa(\omega)L$ becomes close to $\tilde{N}$. These observations suggest that the number of integration points used when calculating the coherency by the trapezoidal rule should be adapted according to the value of $\kappa(\omega)L$. This adaptive trapezoidal rule method is implemented in MATLAB [74] by calculating all the complex coherencies $\gamma_{q_\mu q_\nu}(\omega)$, $\mu, \nu = 1, 2, \ldots, 6N$, at each frequency ω using a number of integration points given by

$$\tilde{N} = \max\{\lceil \alpha(\kappa(\omega)L_{max}) \rceil, \tilde{N}_{min}\}, \tag{2.30}$$

where L_{max} is the maximal distance between any two pontoons and α is a factor determining the accuracy of the integration. The number $\tilde{N}_{min}$ is the number of integration points used when the value of $\kappa(\omega)L_{max}$ is small, meaning that the integrals are not highly oscillatory. In this paper

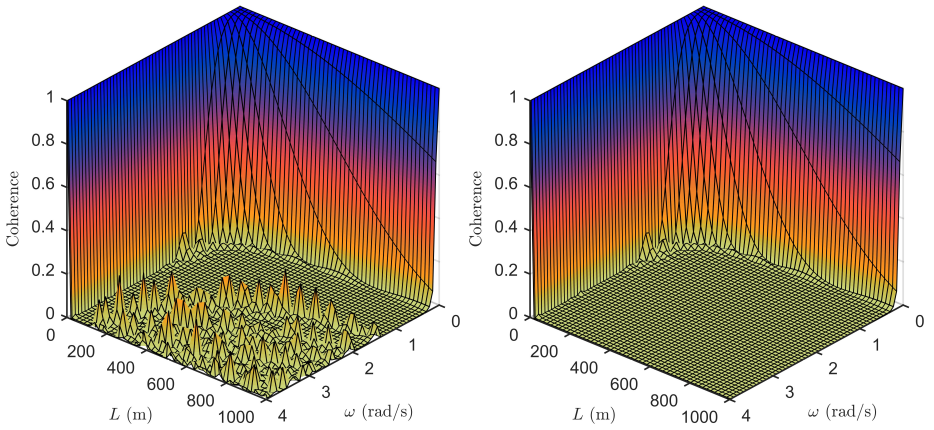

Figure 2.2: The coherence function $\left|\widetilde{\gamma_{q_1 q_7}}(\omega)\right|$ computed using the traditional trapezoidal rule method (2.29) for different distances L with spreading $s = 1$ and mean wave direction $\bar{\theta} = \pi/2$. The number of integration points are $\tilde{N} = 200$ (left) and $\tilde{N} = 1650$ (right).

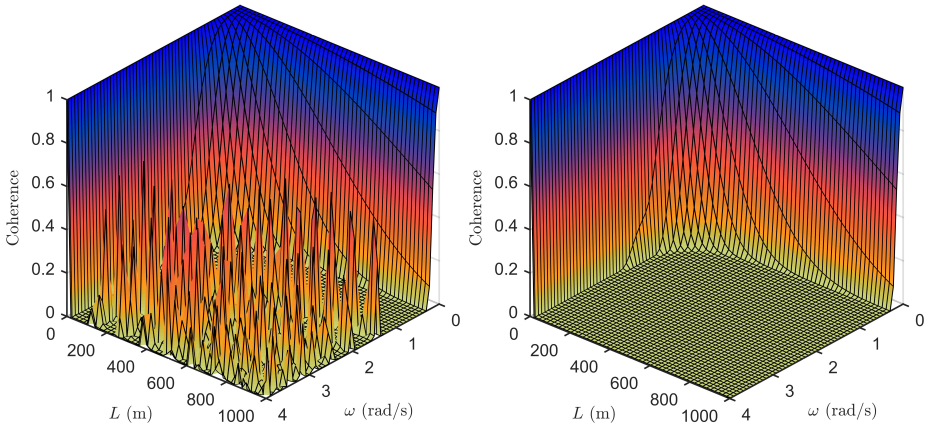

Figure 2.3: The coherence function $\left|\widetilde{\gamma_{q_1 q_7}}(\omega)\right|$ computed using the traditional trapezoidal rule method (2.29) for different distances L with spreading $s = 20$ and mean wave direction $\bar{\theta} = \pi/2$. The number of integration points are $\tilde{N} = 200$ (left) and $\tilde{N} = 1650$ (right).

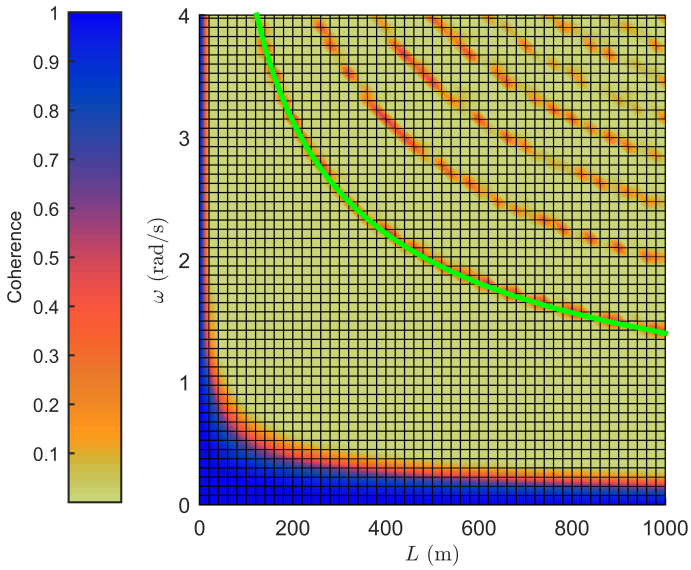

Figure 2.4: The coherence function $\left|\widetilde{\gamma_{q_1 q_7}}(\omega)\right|$ computed using the traditional trapezoidal rule method (2.29) with $\tilde{N} = 200$ integration points, along with the line defined by $\kappa(\omega)L = \tilde{N}$. The shading indicates the value of the coherence, identifying the spurious hats in the upper right corner.

the value $\tilde{N}_{min} = 100$ is used, but a larger value may be necessary if the transfer functions $f_\mu(\theta, \omega)$ are less well-behaved. With $\tilde{N}$ given by (2.30) the number of integration points is the same for all integrals at a given frequency. We could, however, choose $\tilde{N}$ according to the value of $\kappa(\omega)L$ for each individual integral. This is not done here because the former method allows for a faster implementation in MATLAB.

2.4.2 Approximation by the series expansion method

The new method proposed in this paper utilizes the series expansion (2.28) for computing the complex coherencies. If the directional distribution is given by a finite number of Fourier coefficients the series expansion will be finite as shown in Section 2.3.3 and the coherency matrix can be computed exactly. If the number of Fourier coefficients is infinite or excessively large, the complex coherencies can still be approximated by truncating the series expansion (2.28). The idea behind this approximation is that only the terms with index $|k| \leq \hat{N}$, for some number $\hat{N}$, will contribute to the

total sum within the required precision. The complex coherencies are then approximated by

$$\widehat{\gamma_{q_\mu q_\nu}}(\omega) = \sum_{k=-\hat{N}}^{\hat{N}} \frac{C_k^{\mu\nu}(\omega)}{\sqrt{C_0^{\mu\mu}(\omega)C_0^{\nu\nu}(\omega)}} i^k e^{-ik\beta} J_k\left(\kappa(\omega)L\right). \tag{2.31}$$

This will be referred to as the series expansion method.

Figures 2.5 and 2.6 show the resulting coherence functions $|\widehat{\gamma_{q_1 q_7}}(\omega)|$ when the complex coherency $\widehat{\gamma_{q_1 q_7}}(\omega)$ is computed using the series expansion method (2.31) for different distances L between the pontoons. The mean wave direction is $\bar{\theta} = \pi/2$ and the spreading parameter is $s = 1$ in Fig. 2.5, and $s = 20$ in Fig. 2.6. Since s is an integer we obtain the exact coherence functions using $\hat{N} = N_{tot} = 37$ for the case $s = 1$ and $\hat{N} = N_{tot} = 56$ for the case $s = 20$, see Section 2.3.3. Figures 2.5 and 2.6 also indicate that when the complex coherency is approximated using the series expansion method with $\hat{N} < N_{tot}$ we obtain reasonable approximations even when $\hat{N}$ is quite small. Using (2.31) the coherence is approximated more smoothly, with no spurious hats, which is an appealing feature of this method.

2.4.3 The error of the approximation methods

In order to say something about the accuracy of the different ways to approximate the complex coherencies, we compare the exact coherency matrix obtained when the spreading parameter s is an integer with the coherency matrices obtained using the adaptive trapezoidal rule method and the series expansion method. The errors are measured by $\tilde{E} = \max_{\mu,\nu,\omega} \left|\gamma_{q_\mu q_\nu}(\omega) - \widetilde{\gamma_{q_\mu q_\nu}}(\omega)\right|$ and $\hat{E} = \max_{\mu,\nu,\omega} \left|\gamma_{q_\mu q_\nu}(\omega) - \widehat{\gamma_{q_\mu q_\nu}}(\omega)\right|$ for approximation by the adaptive trapezoidal rule and the series expansion respectively.

Figure 2.7 shows how the error $\tilde{E}$ of the adaptive trapezoidal rule method varies with the integration point parameter α in (2.30) for three different values of s and three different mean wave directions $\bar{\theta}$. We observe that the convergence is extremely fast as long as $\alpha > 1$, i.e. the number of integration points $\tilde{N}$ is larger than $\kappa(\omega)L$. This rapid convergence can be explained by the excellent convergence properties of the trapezoidal rule for periodic functions. Since we are using trigonometric interpolation for the transfer functions, the integrand will be infinitely many times continuously differentiable for integer s and geometric convergence is achieved [78]. We

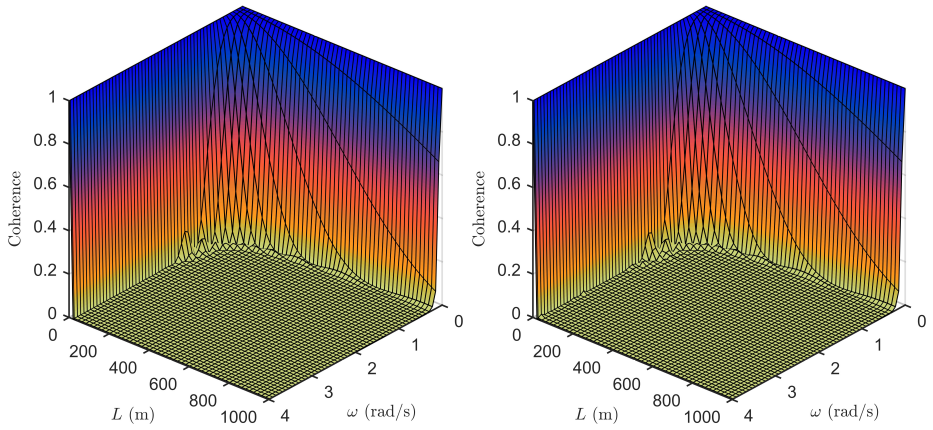

Figure 2.5: The coherence function $\left|\widehat{\gamma_{q_1 q_7}}(\omega)\right|$ computed using the series expansion method (2.31) for different distances L with spreading $s = 1$ and mean wave direction $\bar{\theta} = \pi/2$. The number of included terms are given by $\hat{N} = 5$ (left) and $\hat{N} = N_{tot} = 37$ (right).

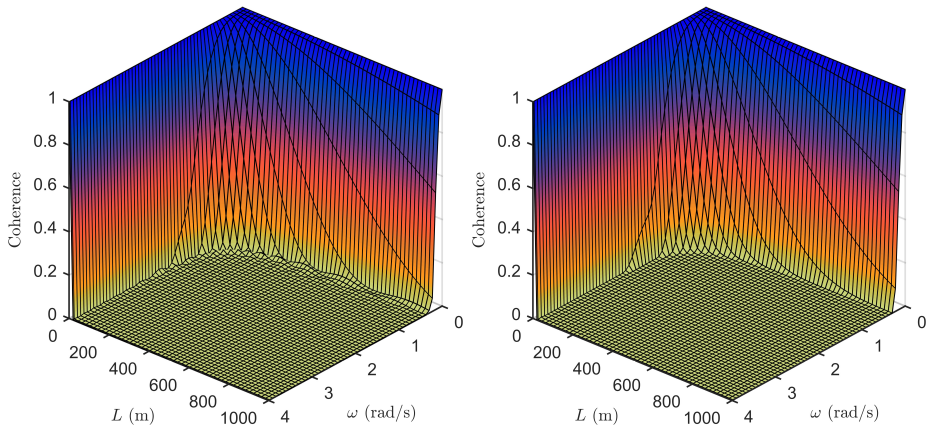

Figure 2.6: The coherence function $\left|\widehat{\gamma_{q_1 q_7}}(\omega)\right|$ computed using the series expansion method (2.31) for different distances L with spreading $s = 20$ and mean wave direction $\bar{\theta} = \pi/2$. The number of terms are given by $\hat{N} = 5$ (left) and $\hat{N} = N_{tot} = 56$ (right).

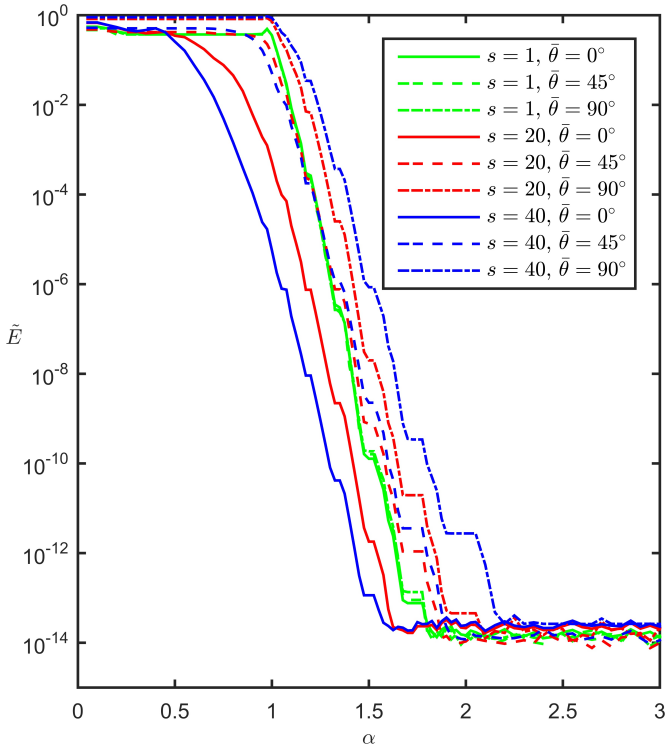

Figure 2.7: The error $\tilde{E}$ of the adaptive trapezoidal rule method as a function of the integration point parameter α in (2.30) for different values of the spreading s and the mean wave direction $\bar{\theta}$.

also observe a faster convergence when $\bar{\theta} = 0$ with increasing effect as s gets larger. This happens because for large s the directional distribution $D(\theta, \omega)$ will be practically zero except for a small band around $\theta = 0$, thus cancelling the rapid oscillations of the exponential factor when $\bar{\theta} = 0$.

Figure 2.8 shows how the error $\hat{E}$ of the series expansion method varies with $\hat{N}$ for three different values of s and three different mean wave directions $\bar{\theta}$. We see that it is not necessary to use all the available coefficients in order to get a good approximation, especially for larger values of s.

For non-integer values of s the *cos-2s* directional distribution will not have a finite Fourier series and we will not have an exact formula for the complex coherencies. However, by including only the Fourier coefficients (2.16) that are larger than e.g. 10^{-16} in absolute value we should obtain the exact solution up to round-off errors. Thus we can calculate the errors $\tilde{E}$ and $\hat{E}$ of the

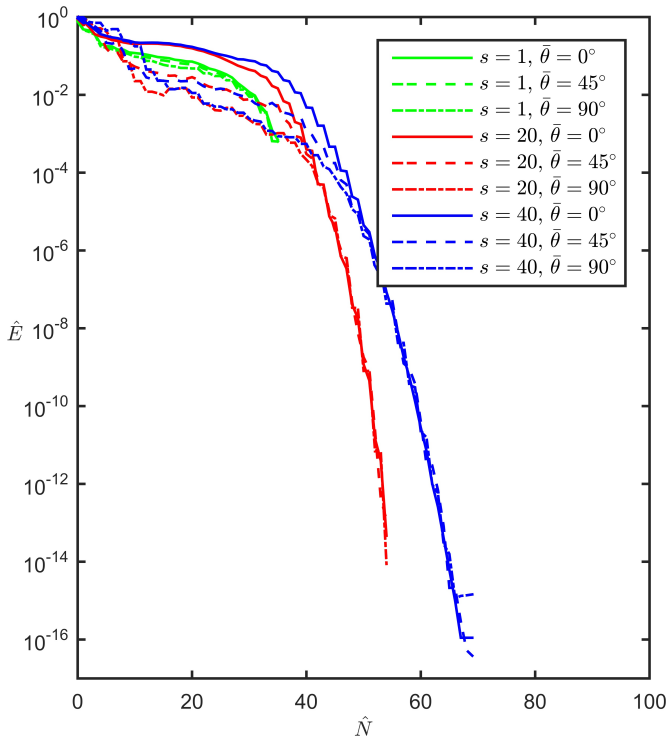

Figure 2.8: The error $\hat{E}$ of the series expansion method as a function of the number $\hat{N}$ of included terms in (2.31) for different values of the spreading s and the mean wave direction $\bar{\theta}$.

two methods like before. Figure 2.9 shows how the error $\tilde{E}$ of the adaptive trapezoidal rule method varies with the integration point parameter α for $\bar{\theta} = \pi/2$ and different non-integer values of s. When s is not an integer the directional distribution will no longer be infinitely many times continuously differentiable and the rapid convergence demonstrated in Fig. 2.7 is no longer guaranteed. However, it appears that the error behaves the same as for integer valued s up to a certain point, and we see from Fig. 2.9 that for $s > 4$ we have rapid convergence until round-off error dominates like before. Figure 2.10 shows how the error $\hat{E}$ of the series expansion method varies with $\hat{N}$ for $\bar{\theta} = 0$ and different non-integer values of s. Again we see that the convergence is slow for small values of s. This can be explained by observing that the Fourier coefficients (2.16) of the directional distribution approaches zero very fast for large enough s but more and more slowly as s decreases.

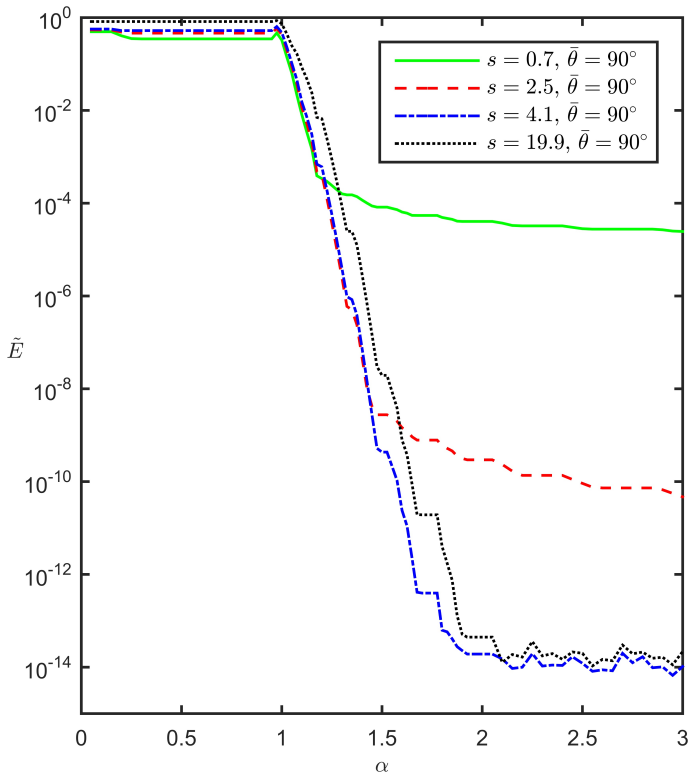

Figure 2.9: The error $\tilde{E}$ of the adaptive trapezoidal rule method as a function of the integration point parameter α for the mean wave direction $\bar{\theta} = \pi/2$ and different non-integer values of the spreading s.

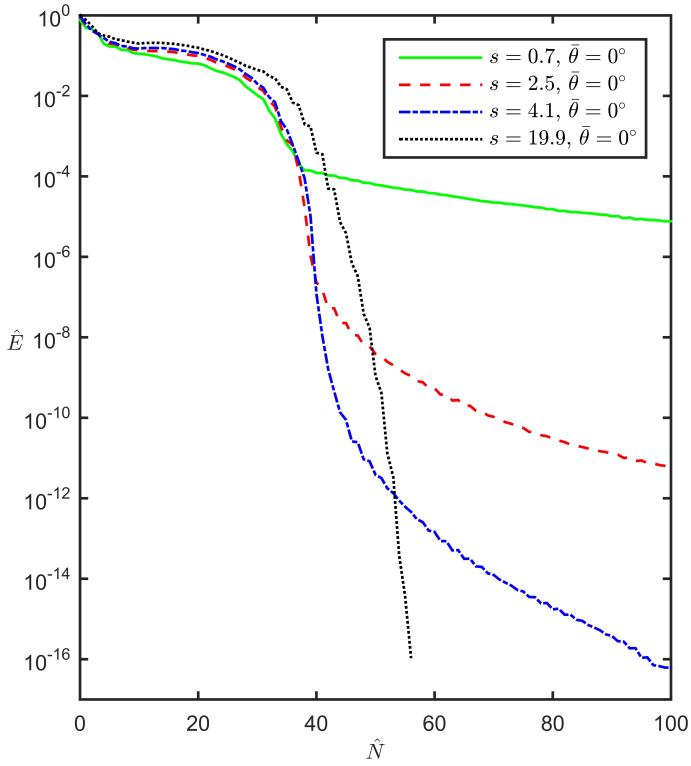

Figure 2.10: The error $\hat{E}$ of the series expansion method as a function of the number $\hat{N}$ of included terms in (2.31) for the mean wave direction $\bar{\theta} = 0$ and different non-integer values of the spreading s.

Figure 2.11: Chained floating bridge, illustration by Multiconsult.

2.5 Wave excitation loads on pontoon type floating bridges

The cross-spectral density matrix of wave excitation loads is often needed as input for dynamic response analysis of floating bridges, both in the frequency and time domain [41, 42, 45]. For time domain analyses simulated realizations of the wave loading process can be obtained from the cross-spectral density matrix using the method found in [69]. An approach for modelling the stochastic dynamic behaviour of pontoon type floating bridges is discussed in [42], where the structural response of the bridge is calculated in the frequency domain using the equation

$$\boldsymbol{S_u}(\omega) = \boldsymbol{H}(\omega)\,\boldsymbol{S_q}(\omega)\,\boldsymbol{H}(\omega)^H,$$

with superscript H denoting the conjugate transpose. Here $\boldsymbol{S_u}(\omega)$ and $\boldsymbol{S_q}(\omega)$ are the cross-spectral density matrices of the response $\boldsymbol{u}(t)$ and the wave excitation load $\boldsymbol{q}(t)$ respectively. $\boldsymbol{H}(\omega)$ is the transfer function matrix which takes into account the structural mass, damping and stiffness of the

bridge structure, as well as hydrostatic stiffness, added mass and added damping due to the pontoons. The method proposed in this paper can be used to efficiently calculate the cross-spectral density matrix $\boldsymbol{S_q}(\omega)$ needed in this approach.

In the case of pontoon type floating bridges the structure will experience wave loads only where the pontoons are located, each pontoon is considered a rigid body and is thus loaded in six degrees of freedom (dofs). This means that with N pontoons the cross-spectral density matrix $\boldsymbol{S_q}(\omega)$ of the wave excitation loads will be a $6N$-by-$6N$ matrix whose elements are the cross-spectral densities $S_{q_\mu q_\nu}(\omega)$. The calculation of the cross-spectral density matrix must be performed for every wave situation considered, which in applications such as long-term response analyses can be a very large amount [68]. This motivates the need for an efficient calculation method.

In order to get some idea of how the different approximation methods perform with respect to computation time, the cross-spectral density matrix is computed for two different pontoon type floating bridges, the Bergsøysund bridge with $N = 7$ pontoons and a chained floating bridge with $N = 18$ pontoons [65]. The chained floating bridge is illustrated in Fig. 2.11. The same pontoon type is used for both bridges, but the number of pontoons and their locations are different. The locations of the pontoons are shown in Figs. 2.12 and 2.13 for the Bergsøysund bridge and the chained floating bridge respectively. An example of a transfer function calculated using WADAM is given in Fig. 2.14. The transfer functions are calculated for single pontoons, thus neglecting interaction effects among multiple bodies. This is justified by to the fact that the distance between pontoons is large compared to the dimensions of the pontoons. The cross-spectral density matrix is computed by first calculating all $(6N)^2$ coherencies $\gamma_{q_\mu q_\nu}(\omega)$ with an approximation error less than 10^{-3} as measured by $\tilde{E}$ and $\hat{E}$, see Section 2.4.3. Then the auto-spectral densities $S_{q_\nu q_\nu}(\omega)$ are calculated using (2.27) and the cross-spectral densities are found by the relation

$$S_{q_\mu q_\nu}(\omega) = \gamma_{q_\mu q_\nu}(\omega) \sqrt{S_{q_\mu q_\mu}(\omega)\, S_{q_\nu q_\nu}(\omega)}.$$

In this example the *cos-2s* directional distribution from Section 2.2.5 is used with a constant spreading parameter $s(\omega) = s$, and the one-dimensional wave spectral density $S_{\eta\eta}(\omega)$ is given by the Pierson-Moskowitz spectrum [73].

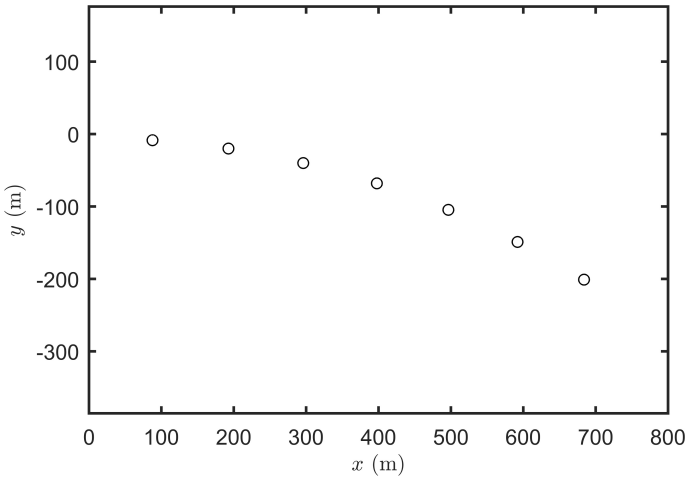

Figure 2.12: Pontoon locations for the Bergsøysund floating bridge.

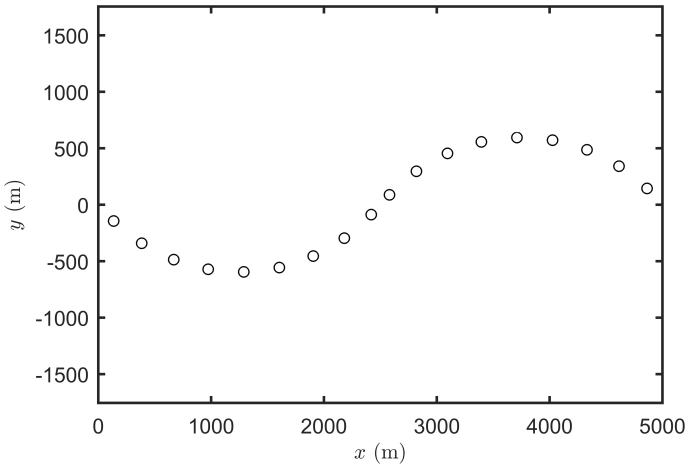

Figure 2.13: Pontoon locations for the chained floating bridge.

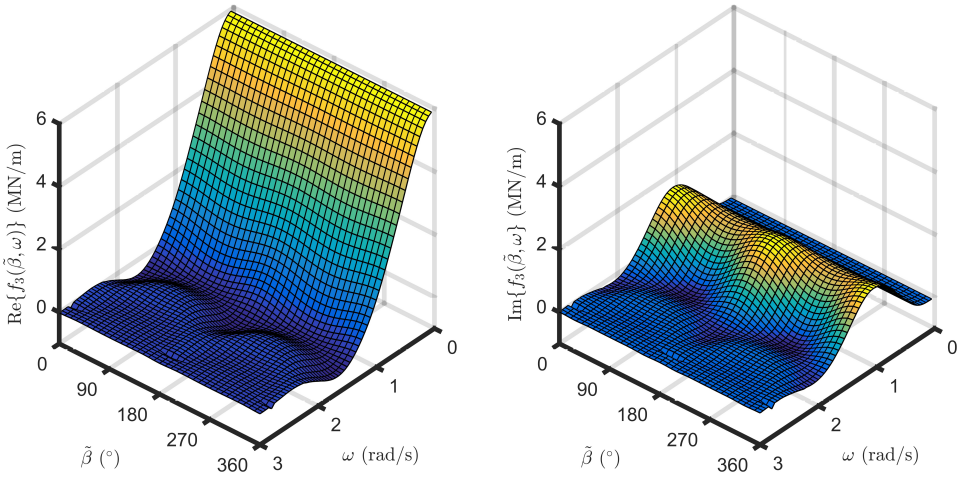

Figure 2.14: The transfer function for the heave force (vertical direction) on one pontoon, given by its real part (left) and imaginary part (right).

Table 2.1: The computation time for the different methods of calculating the cross-spectral density matrix. L_{max} is the maximal distance between two pontoons.

	$s = 1$	$s = 20$
Bergsøysund bridge – 7 pontoons, L_{max} = 626 m		
Traditional trapezoidal rule method	5.0 s	5.1 s
Adaptive trapezoidal rule method	1.5 s	1.6 s
Series expansion method	1.1 s	1.1 s
Chained floating bridge – 18 pontoons, L_{max} = 4735 m		
Traditional trapezoidal rule method	576 s	595 s
Adaptive trapezoidal rule method	171 s	176 s
Series expansion method	6.8 s	7.1 s

The approximation methods discussed in this paper are implemented in MATLAB and the computation times for the cases $s = 1$ and $s = 20$ are given in Table 2.1. Since the runtime in MATLAB is very sensitive to the specific implementation, it is emphasized that the numbers in Table 2.1 are only meant to give some idea of the computational effort. It is clear, however, that the adaptive trapezoidal rule method and the series expansion method both achieve a great improvement in computational time, as compared to the traditional trapezoidal rule method. We also notice that the increase in computational effort due to larger distances between pontoons is much smaller for the series expansion method. In Table 2.1 we see that for the trapezoidal rule methods the computational time increases by a factor of approximately 100, while for the series expansion method the increase is only by a factor of approximately 6.

It should be pointed out that in many practical applications the cross-spectral densities between points at large distances are practically zero, making it a reasonable approximation to set them equal to zero. This will of course greatly improve the computation time and the trapezoidal rule methods may still be feasible. However, an assessment of whether this approximation is reasonable must then be carried out for each particular case. The new method proposed in this paper eliminates the need for such an assessment.

2.6 Conclusions

A new method has been presented for the calculation of cross-spectral densities in the stochastic modelling of ocean waves and wave loads, based on a series expansion solution of the integral expressing the cross-spectral density. The method is developed for first order wave excitation loads but it is readily extended to the computation of other cross-spectral densities, e.g. for wave elevation, wave kinematics or second order load. The only difference will be which transfer functions that are used. In addition to presenting the new method, the traditional trapezoidal rule method has been improved by developing an adaptive way of choosing the number of integration points.

The accuracy of the adaptive trapezoidal rule method and the series expansion method has been investigated. The adaptive trapezoidal rule method shows very rapid convergence after a certain point, before which the error is relatively large due to so-called spurious hats. The series expansion method also displays a generally rapid convergence, in addition to avoiding the spurious hat errors altogether.

When applied to two different pontoon type floating bridges the adaptive trapezoidal rule method and the series expansion method both achieve a great improvement in computational effort compared to the traditional trapezoidal rule method. When the dimensions of the floating bridge increase, i.e. the number of pontoons and their relative distances increase, the series expansion method is superior with respect to computation time.

2.A Appendix A

This section includes the derivation of the expression for the cross-spectral density of the wave elevation given in Section 2.2.1. This derivation can also be found in [71].

When it is modelled as a homogeneous stationary stochastic process, the sea elevation at the point (x, y) at time t, denoted $\eta(x, y, t)$, is written as

$$\eta(x, y, t) = \int_{-\infty}^{\infty} e^{i\omega t - i\kappa(x\cos\theta + y\sin\theta)} dB(\boldsymbol{\kappa}, \omega), \tag{2.32}$$

where $\boldsymbol{\kappa} = [\kappa\cos\theta, \kappa\sin\theta]$ is the wave number vector, ω is the frequency and $B(\boldsymbol{\kappa}, \omega)$ is the spectral process associated with the wave elevation. The assumption of homogeneity and stationarity implies that the spectral process must have zero mean and orthogonal increments, giving the cross-correlation function

$$\begin{aligned} R_{mn}(\tau) &= E\left[\eta(x_m, y_m, t+\tau)\,\overline{\eta(x_n, y_n, t)}\right] \\ &= \int_{-\infty}^{\infty}\int_{\theta}\int_{\kappa} e^{i\omega\tau} e^{-i\kappa(\Delta x\cos\theta + \Delta y\sin\theta)} S_{\eta\eta}^{(3)}(\kappa, \theta, \omega)\, d\kappa d\theta d\omega. \end{aligned} \tag{2.33}$$

Here $\Delta x = x_m - x_n$ and $\Delta y = y_m - y_n$ is the separation of the locations (x_m, y_m) and (x_n, y_n) in space and $S_{\eta\eta}^{(3)}(\kappa, \theta, \omega)$ is the three-dimensional wave spectral density. The cross-spectral density is obtained as the Fourier transform of the cross-correlation function (2.33) with respect to the time lag τ:

$$\begin{aligned} S_{mn}(\omega) &= \frac{1}{2\pi}\int_{-\infty}^{\infty} R_{mn}(\Delta x, \Delta y, \tau)\, e^{-i\omega\tau} d\tau \\ &= \int_{\theta}\int_{\kappa} e^{-i\kappa(\Delta x\cos\theta + \Delta y\sin\theta)} S_{\eta\eta}^{(3)}(\kappa, \theta, \omega)\, d\kappa d\theta. \end{aligned} \tag{2.34}$$

The formula for the cross-spectral density can be simplified using the dispersion relation which relates the frequency ω and the wave number κ by a one-to-one mapping $\kappa = \kappa(\omega)$, or equivalently $\omega = \omega(\kappa)$. Now κ and ω are no longer independent variables in the integration in (2.34) and the formula finally reduces to

$$S_{mn}(\omega) = \int_{\theta} e^{-i\kappa(\omega)(\Delta x\cos\theta + \Delta y\sin\theta)} S_{\eta\eta}^{(2)}(\theta, \omega)\, d\theta,$$

where $S_{\eta\eta}^{(2)}(\theta, \omega)$ is the directional wave spectral density.

2.B Appendix B

This section is devoted to proving the identity (2.15), which is stated in Theorem 1 below. The proof of Theorem 1 relies upon two parts, which we summarize in two propositions.

Proposition 1 *For $n \in \{1, 2, 3, \dots\}$ and $\phi \in \mathbb{R}$ we have the following Fourier series expansions for even- and odd-numbered powers of the cosine function respectively:*

$$\cos^{2n}\phi = \frac{1}{2^{2n}}\binom{2n}{n} + \frac{1}{2^{2n-1}}\sum_{k=1}^{n}\binom{2n}{n+k}\cos(2k\phi) \tag{2.35a}$$

$$\cos^{2n-1}\phi = \frac{1}{2^{2n-2}}\sum_{k=1}^{n}\binom{2n-1}{n+k-1}\cos((2k-1)\phi) \tag{2.35b}$$

Proof For $\tilde{n} \in \mathbb{N}$ we can use the complex representation of the cosine function and the binomial theorem to obtain

$$\begin{aligned}
\cos^{\tilde{n}}\phi &= \frac{1}{2^{\tilde{n}}}\left(e^{i\phi} + e^{-i\phi}\right)^{\tilde{n}} = \frac{1}{2^{\tilde{n}}}\sum_{k=0}^{\tilde{n}}\binom{\tilde{n}}{k}e^{i(\tilde{n}-k)\phi}e^{-ik\phi} \\
&= \frac{1}{2^{\tilde{n}}}\sum_{k=0}^{\tilde{n}}\binom{\tilde{n}}{k}\left(\cos(\tilde{n}-k)\phi + i\sin(\tilde{n}-k)\phi\right)\left(\cos k\phi - i\sin k\phi\right) \\
&= \frac{1}{2^{\tilde{n}}}\sum_{k=0}^{\tilde{n}}\binom{\tilde{n}}{k}\left(\cos(\tilde{n}-k)\phi\cos k\phi + \sin(\tilde{n}-k)\phi\sin k\phi\right) \\
&\quad + i\frac{1}{2^{\tilde{n}}}\sum_{k=0}^{\tilde{n}}\binom{\tilde{n}}{k}\left(\sin(\tilde{n}-k)\phi\cos k\phi - \cos(\tilde{n}-k)\phi\sin k\phi\right) \\
&= \frac{1}{2^{\tilde{n}}}\sum_{k=0}^{\tilde{n}}\binom{\tilde{n}}{k}\cos((\tilde{n}-2k)\phi) - i\frac{1}{2^{\tilde{n}}}\sum_{k=0}^{\tilde{n}}\binom{\tilde{n}}{k}\sin((\tilde{n}-2k)\phi).
\end{aligned}$$

Assuming $\phi \in \mathbb{R}$ it is obvious that $\cos^{\tilde{n}}\phi$ is a real number, which means that the imaginary part of the right hand side above must vanish, resulting in the expression

$$\cos^{\tilde{n}}\phi = \frac{1}{2^{\tilde{n}}}\sum_{k=0}^{\tilde{n}}\binom{\tilde{n}}{k}\cos((\tilde{n}-2k)\phi). \tag{2.36}$$

If $\tilde{n}$ is an even number it can be written as $\tilde{n} = 2n$ for some $n \in \{1, 2, 3, \dots\}$ and we have then

$$\cos^{2n}\phi = \frac{1}{2^{2n}} \sum_{k=0}^{2n} \binom{2n}{k} \cos\left(2\left(n-k\right)\phi\right). \tag{2.37}$$

For the binomial coefficients we have the symmetry property

$$\binom{2n}{2n-k} = \binom{2n}{k}, \qquad k \in \{0, 1, 2, \dots, 2n\}, \tag{2.38}$$

which along with the symmetry of the cosine function gives that term number $2n-k$ in the sum (2.37) is equal to term number k. Thus each term is repeated twice, except for the middle term where $k = n$, and the sum can be written as

$$\begin{aligned}\cos^{2n}\phi &= \frac{1}{2^{2n}}\binom{2n}{n} + \frac{1}{2^{2n-1}} \sum_{k=0}^{n-1} \binom{2n}{k} \cos\left(2\left(n-k\right)\phi\right) \\ &= \frac{1}{2^{2n}}\binom{2n}{n} + \frac{1}{2^{2n-1}} \sum_{k=1}^{n} \binom{2n}{n-k} \cos\left(2kx\right),\end{aligned}$$

where the last equality is simply a reordering of the terms. Finally (2.35a) is obtained by again using the symmetry property (2.38) of the binomial coefficient.

If on the other hand $\tilde{n}$ is an odd number in (2.36) we can write $\tilde{n} = 2n - 1$ for some $n \in \{1, 2, 3, \dots\}$, and (2.35b) is obtained using the same approach as for even $\tilde{n}$, observing that two and two terms are equal. □

Proposition 2 *For $k \in \{0, 1, 2, 3, \dots\}$ and $s \in \mathbb{R}$ with $s \geq 0$ the following holds:*

$$\sum_{n=0}^{\infty} \frac{1}{2^{2n+k-1}} \binom{s}{2n+k} \binom{2n+k}{n+k} = \frac{1}{2^{s-1}} \binom{2s}{s+k}. \tag{2.39}$$

Here the binomial coefficients are interpreted in the generalized sense, being defined using the gamma function by

$$\binom{a}{b} = \frac{\Gamma(a+1)}{\Gamma(a-b+1)\Gamma(b+1)}, \qquad a, b \in \mathbb{R}.$$

Proof The key for calculating the series is the method of hypergeometric summation [37]. First we use Algorithm 2.8 in [37] to write the series in (2.39) as a hypergeometric function. Expressing the binomial coefficients using the gamma function, the n-th term in the series can be written as

$$a_n = \frac{1}{2^{2n+k-1}} \binom{s}{2n+k} \binom{2n+k}{n+k} = \frac{1}{2^{2n+k-1}} \frac{\Gamma(s+1)}{\Gamma(s-2n-k+1)\, n!\, (n+k)!}.$$

This gives the term ratio

$$\frac{a_{n+1}}{a_n} = \frac{(s-2n-k)(s-2n-k-1)}{4(n+1)(n+k+1)} = \frac{\left(n+\frac{k-s}{2}\right)\left(n+\frac{k+1-s}{2}\right)}{(n+1)(n+k+1)},$$

where we have used the property that $\Gamma(x+1) = x\Gamma(x)$ for any x. Thus the term ratio is written as $\frac{a_{n+1}}{a_n} = \frac{u_n}{v_n}$, where u_n and v_n are polynomials in n factorized in linear factors. Observing that the initial term is

$$a_0 = \frac{1}{2^{k-1}} \frac{\Gamma(s+1)}{\Gamma(s-k+1)\, k!} = \frac{1}{2^{k-1}} \binom{s}{k},$$

it follows from Algorithm 2.8 in [37] that we can rewrite the series using the Gauss hypergeometric series as

$$\sum_{n=0}^{\infty} \frac{1}{2^{2n+k-1}} \binom{s}{2n+k} \binom{2n+k}{n+k} = \frac{1}{2^{k-1}} \binom{s}{k} {}_2F_1\left(\frac{k-s}{2}, \frac{k+1-s}{2}; k+1; 1\right). \tag{2.40}$$

The Gauss hypergeometric series is defined as

$${}_2F_1(a,b;c;z) = \frac{\Gamma(c)}{\Gamma(a)\Gamma(b)} \sum_{n=0}^{\infty} \frac{\Gamma(a+n)\Gamma(b+n)}{\Gamma(c+n)} \frac{z^n}{n!},$$

and according to property 15.1.20 in [1] we have for $z = 1$ that

$${}_2F_1(a,b;c;1) = \frac{\Gamma(c)\Gamma(c-a-b)}{\Gamma(c-a)\Gamma(c-b)}$$

holds whenever $\mathrm{Re}(c-a-b) > 0$ and $c \notin \{0, -1, -2, -3, \dots\}$. Using this property (2.40) yields

$$\sum_{n=0}^{\infty} \frac{1}{2^{2n+k-1}} \binom{s}{2n+k} \binom{2n+k}{n+k} = \frac{1}{2^{k-1}} \binom{s}{k} \frac{\Gamma(k+1)\Gamma\left(s+\frac{1}{2}\right)}{\Gamma\left(\frac{s+k+2}{2}\right)\Gamma\left(\frac{s+k+1}{2}\right)}, \tag{2.41}$$

which is valid for $\mathrm{Re}\left(k+1-\frac{k-s}{2}-\frac{k+1-s}{2}\right) = \mathrm{Re}(s)+\frac{1}{2} > 0$ and $k \notin \{-1,-2,-3,\dots\}$. These conditions are clearly satisfied when $s \in \mathbb{R}$ with $s \geq 0$ and $k \in \{0,1,2,3,\dots\}$. Finally we rewrite the expression obtained in (2.41) using property 6.1.18 in [1], the duplication formula for the gamma function, finding that

$$\begin{aligned}\sum_{n=0}^{\infty} \frac{1}{2^{2n+k-1}} \binom{s}{2n+k} \binom{2n+k}{n+k} &= \frac{2^{s+1}\Gamma\left(s+\frac{1}{2}\right)\Gamma(k+1)}{\sqrt{\pi}\Gamma(s+k+1)} \binom{s}{k} \\ &= \frac{2^{s+1}\Gamma\left(s+\frac{1}{2}\right)\Gamma(k+1)\Gamma(s+1)}{\sqrt{\pi}\Gamma(s+k+1)\Gamma(s-k+1)\Gamma(k+1)} \\ &= \frac{1}{2^{s-1}} \frac{\Gamma(2s+1)}{\Gamma(s+k+1)\Gamma(s-k+1)} \\ &= \frac{1}{2^{s-1}} \binom{2s}{s+k},\end{aligned}$$

which concludes the proof. □

With the aid of Proposition 1 and Proposition 2 we can now prove the identity (2.15) which we state here as a Theorem.

Theorem 1 *Let s be any non-negative real number. Then for any $\phi \in \mathbb{R}$ the following equality holds:*

$$\begin{aligned}\left(\cos^2\frac{\phi}{2}\right)^s &= \frac{1}{2^{2s}}\binom{2s}{s} + \frac{1}{2^{2s-1}} \sum_{k=1}^{\infty} \binom{2s}{s+k} \cos(k\phi) \\ &= \frac{1}{2^{2s}} \frac{\Gamma(2s+1)}{\Gamma^2(s+1)} + \frac{1}{2^{2s-1}} \sum_{k=1}^{\infty} \frac{\Gamma(2s+1)}{\Gamma(s-k+1)\Gamma(s+k+1)} \cos(k\phi).\end{aligned}$$

Proof Let s be any non-negative real number and define the function $f : \mathbb{R} \to \mathbb{R}$ by

$$f(\phi) = \left(\cos^2\frac{\phi}{2}\right)^s = \frac{1}{2^s}(1+\cos\phi)^s, \qquad \phi \in \mathbb{R}.$$

Now $f(\phi)$ can be expanded using the binomial series as

$$f(\phi) = \frac{1}{2^s} \sum_{n=0}^{\infty} \binom{s}{n} \cos^n\phi, \tag{2.42}$$

which is convergent for any value of ϕ, since $s \geq 0$. In order to further expand $f(\phi)$ into a Fourier series we split the series (2.42) into two series of even and odd powers of the cosine function respectively, and utilize the formulas (2.35a) and (2.35b) from Proposition 1. This yields

$$\begin{aligned}
2^s f(\phi) &= 1 + \sum_{n=1}^{\infty} \binom{s}{2n} \cos^{2n}\phi + \sum_{n=1}^{\infty} \binom{s}{2n-1} \cos^{2n-1}\phi \\
&= 1 + \sum_{n=1}^{\infty} \frac{1}{2^{2n}} \binom{s}{2n} \binom{2n}{n} + \sum_{n=1}^{\infty} \sum_{k=1}^{n} \frac{1}{2^{2n-1}} \binom{s}{2n} \binom{2n}{n+k} \cos(2k\phi) \\
&\quad + \sum_{n=1}^{\infty} \sum_{k=1}^{n} \frac{1}{2^{2n-2}} \binom{s}{2n-1} \binom{2n-1}{n+k-1} \cos((2k-1)\phi).
\end{aligned}$$

Changing the order of summation gives

$$\begin{aligned}
2^s f(\phi) &= \frac{1}{2} \sum_{n=0}^{\infty} \frac{1}{2^{2n-1}} \binom{s}{2n} \binom{2n}{n} \\
&\quad + \sum_{k=1}^{\infty} \left(\sum_{n=k}^{\infty} \frac{1}{2^{2n-1}} \binom{s}{2n} \binom{2n}{n+k} \right) \cos(2k\phi) \\
&\quad + \sum_{k=1}^{\infty} \left(\sum_{n=k}^{\infty} \frac{1}{2^{2n-2}} \binom{s}{2n-1} \binom{2n-1}{n+k-1} \right) \cos((2k-1)\phi),
\end{aligned}$$

and if we change the summation index such that all sums start from $n = 0$ we obtain

$$\begin{aligned}
2^s f(\phi) &= \frac{1}{2} \sum_{n=0}^{\infty} \frac{1}{2^{2n-1}} \binom{s}{2n} \binom{2n}{n} \\
&\quad + \sum_{k=1}^{\infty} \left(\sum_{n=0}^{\infty} \frac{1}{2^{2n+2k-1}} \binom{s}{2n+2k} \binom{2n+2k}{n+2k} \right) \cos(2k\phi) \\
&\quad + \sum_{k=1}^{\infty} \left(\sum_{n=0}^{\infty} \frac{1}{2^{2n+2k-2}} \binom{s}{2n+2k-1} \binom{2n+2k-1}{n+2k-1} \right) \cos((2k-1)\phi) \\
&= \frac{1}{2} \sum_{n=0}^{\infty} \frac{1}{2^{2n-1}} \binom{s}{2n} \binom{2n}{n} \\
&\quad + \sum_{k=1}^{\infty} \left(\sum_{n=0}^{\infty} \frac{1}{2^{2n+k-1}} \binom{s}{2n+k} \binom{2n+k}{n+k} \right) \cos(k\phi),
\end{aligned}$$

where the last equality is obtained by combining the sums with even and odd indices. Finally the Fourier coefficients are found by computing the series according to Proposition 2 and we end up with

$$\begin{aligned}\left(\cos^2\frac{\phi}{2}\right)^s &= \frac{1}{2^{2s}}\binom{2s}{s} + \frac{1}{2^{2s-1}}\sum_{k=1}^{\infty}\binom{2s}{s+k}\cos(k\phi) \\ &= \frac{1}{2^{2s}}\frac{\Gamma(2s+1)}{\Gamma^2(s+1)} + \frac{1}{2^{2s-1}}\sum_{k=1}^{\infty}\frac{\Gamma(2s+1)}{\Gamma(s-k+1)\,\Gamma(s+k+1)}\cos(k\phi),\end{aligned}$$

which is what we wanted to prove. □

Paper II:

CHAPTER 3

Full long-term extreme response analysis of marine structures using inverse FORM

Finn-Idar G. Giske, Bernt J. Leira, Ole Øiseth

Published in
Probabilistic Engineering Mechanics 50(2017), pp. 1-8.
doi:10.1016/j.probengmech.2017.10.007

Abstract

An exact and an approximate formulation for the long-term extreme response of marine structures are discussed and compared. It is well known that the approximate formulation can be evaluated in a simplified way by using the first order reliability method (FORM), known for its computational efficiency. In this paper it is shown how this can be done for the exact formulation as well. Characteristic values of the long-term extreme response are calculated using inverse FORM (IFORM) for both formulations. A new method is proposed for the numerical solution of the IFORM problem, resolving some convergence issues of a well-established iteration algorithm. The proposed method is demonstrated for a single-degree-of-freedom (SDOF) example and the accuracy of the long-term extreme response approximations is investigated, revealing that the IFORM methods provide good estimates in a very efficient manner. The reduced number of required short-term response calculations provided by the IFORM methods is expected to make full long-term extreme response analysis feasible also for more complex systems.

3.1 Introduction

For the evaluation of extreme responses in the design of marine structures, a full long-term response analysis is recognized as the most accurate approach [60, 68]. However, the computational effort is in many cases a limiting factor, and simplified approaches such as the environmental contour methods [29, 30, 79] are frequently used in practice. Over the last decade new methods have been proposed in an effort to make the full long-term approach more efficient, either by reducing the required number of short-term response calculations [68, 75, 80] or by computing the short-term quantities more efficiently [20, 57, 58]. In this paper we continue the development of robust and efficient methods for full long-term response analysis.

A comparison of different models for long-term extreme response can be found in [68]. In the present paper we focus on the models based on all short-term extreme peaks. For these models the long-term distribution of the short-term extreme value is formulated as an average of the short-term extreme value distributions weighted by the distribution of the environmental parameters. An exact formulation is obtained when an ergodic averaging is used, but using the population mean yields a very common approximate formulation.

In Section 3.2 of this paper we compare the exact and the approximate formulation, and show that the latter is non-conservative as it underestimates the long-term extreme responses. Nevertheless, the approximate formulation is commonly used because it readily lends itself to being solved very efficiently in an approximate manner by the first-order reliability method (FORM) known from structural reliability. However, as we show in Section 3.3, the exact formulation can also be solved using FORM. To the authors' knowledge this has not been done before.

Section 3.4 deals with the numerical solution of characteristic values for the extreme response using inverse FORM (IFORM). IFORM was introduced in [79] for calculation of extreme response using environmental contours. The IFORM method has also been extended to a more general reliability context [13, 47]. In [68] the IFORM solution for the extreme response of marine structures was found using a simple iteration algorithm proposed in [47]. This iteration algorithm has some convergence issues though, and these are addressed in the present paper. A new method is proposed for dealing with the convergence issues, using a sufficient increase condition

along with a backtracking approach for the maximization problem being solved. It should be mentioned that an exact arc search algorithm [17] can also be used to obtain convergence, but this approach is expected to require a larger number of short-term response calculations. Furthermore, the proposed method is simpler in its form and will be easier to implement.

In Sections 3.5 and 3.6 a single-degree-of-freedom (SDOF) example is given, demonstrating the use of the proposed method. Some numerical results are also presented in order to compare the method with the standard iteration algorithm, and to assess the accuracy of the approximate formulation and the IFORM approximations.

3.2 Long-term extreme response modelling

For the assessment of long-term extreme responses of marine structures, it is common to model the environmental conditions as a sequence of short-term states during which the environmental processes are assumed stationary [60]. Each short-term state is defined by a collection of environmental parameters $\boldsymbol{S} = [S_1, S_2, \ldots, S_n]$, with a joint probability density function (PDF) $f_{\boldsymbol{S}}(\boldsymbol{s})$ which we assume is given. We note that in order to be able to estimate $f_{\boldsymbol{S}}(\boldsymbol{s})$ in practice, an ergodicity assumption is required for the environmental parameters [59]. The long-term situation is composed of a large number N of short-term conditions, each of duration $\tilde{T}$, giving a long-term time duration of $T = N\tilde{T}$.

We denote by $\tilde{R}$ the largest peak of the response process during an arbitrary short-term condition, and by $\tilde{R}_{LT}$ the largest peak during the entire long-term period. Assuming that the short-term extreme values are independent, the long-term extreme value distribution $F_{\tilde{R}_{LT}}(r)$ is obtained as

$$F_{\tilde{R}_{LT}}(r) = F_{\tilde{R}}(r)^N, \tag{3.1}$$

where $F_{\tilde{R}}(r)$ is the cumulative distribution function (CDF) of the short-term extreme value $\tilde{R}$.

3.2.1 Formulations based on the short-term extreme peaks

Let the CDF of the largest peak during a short-term condition with environmental parameters $\boldsymbol{s}$ be given by $F_{\tilde{R}|\boldsymbol{S}}(r|\boldsymbol{s})$. The exact long-term CDF $F_{\tilde{R}}(r)$ of the short-term extreme value is obtained when an ergodic aver-

aging is used [39, 59], see also Section 12.4.2 of [60]. Thus we have the formulation

$$F_{\tilde{R}}(r) = \exp\left\{\int_{\boldsymbol{s}} \left(\ln F_{\tilde{R}|\boldsymbol{S}}(r|\boldsymbol{s})\right) f_{\boldsymbol{S}}(\boldsymbol{s})\, d\boldsymbol{s}\right\}. \tag{3.2}$$

The claim of exactness for the formulation (3.2) is perhaps somewhat unfortunate, since e.g. the assumption of stationary environmental processes is clearly not exact. The term "exact" is simply used here in the sense that the formulation (3.2) is the mathematically correct approach within the assumptions.

Usually, we are only interested in $F_{\tilde{R}}(r)$ for large values of r, which means that $F_{\tilde{R}|\boldsymbol{S}}(r|\boldsymbol{s}) \approx 1$. Using the linear approximations of the logarithm and the exponential function yields

$$\begin{aligned} F_{\tilde{R}}(r) &\approx \exp\left\{-\int_{\boldsymbol{s}} \left(1 - F_{\tilde{R}|\boldsymbol{S}}(r|\boldsymbol{s})\right) f_{\boldsymbol{S}}(\boldsymbol{s})\, d\boldsymbol{s}\right\} \\ &\approx 1 - \int_{\boldsymbol{s}} \left(1 - F_{\tilde{R}|\boldsymbol{S}}(r|\boldsymbol{s})\right) f_{\boldsymbol{S}}(\boldsymbol{s})\, d\boldsymbol{s}. \end{aligned}$$

From the properties of a PDF we know that the integral of $f_{\boldsymbol{S}}(\boldsymbol{s})$ over all values of $\boldsymbol{s}$ equals unity, and we obtain the approximation $F_{\tilde{R}}(r) \approx \bar{F}_{\tilde{R}}(r)$, where $\bar{F}_{\tilde{R}}(r)$ is the population mean

$$\bar{F}_{\tilde{R}}(r) = \int_{\boldsymbol{s}} F_{\tilde{R}|\boldsymbol{S}}(r|\boldsymbol{s})\, f_{\boldsymbol{S}}(\boldsymbol{s})\, d\boldsymbol{s}. \tag{3.3}$$

The formulation (3.3) is a common approximation for the long-term CDF of the short-term extreme value, partly because it readily lends itself to being solved very efficiently by the FORM method. Furthermore, it is easy to mistakenly consider (3.3) as exact, because the formulation intuitively appears to be correct.

3.2.2 Connection with the average upcrossing rate formulation

If we assume that upcrossings of high levels are statistically independent, the short-term extreme peak distribution is given by

$$F_{\tilde{R}|\boldsymbol{S}}(r|\boldsymbol{s}) = \exp\left\{-\nu(r|\boldsymbol{s})\, \tilde{T}\right\}, \tag{3.4}$$

where $\nu(r|\boldsymbol{s})$ denotes the short-term mean frequency of r-upcrossings. For details we refer to Section 10.5 of [60]. Note that the expression (3.4) is only valid for high levels, i.e. for relatively large values of r. Inserting the expression (3.4) into (3.2) yields

$$F_{\tilde{R}}(r) = \exp\left\{-\tilde{T}\int_{\boldsymbol{s}} \nu(r|\boldsymbol{s})\, f_{\boldsymbol{S}}(\boldsymbol{s})\, d\boldsymbol{s}\right\}, \tag{3.5}$$

and the relation (3.1) for the long-term extreme value distribution $F_{\tilde{R}_{LT}}(r)$ gives that

$$F_{\tilde{R}_{LT}}(r) = \exp\left\{-T\int_{\boldsymbol{s}} \nu(r|\boldsymbol{s})\, f_{\boldsymbol{S}}(\boldsymbol{s})\, d\boldsymbol{s}\right\}, \tag{3.6}$$

where $T = N\tilde{T}$ is the long-term period. The expression (3.6) is also a common model for the long-term extreme response [59]. The fact that (3.2) and (3.6) are equivalent formulations is in agreement with what is found in [68].

3.2.3 Non-conservativity of the approximate formulation

As a simple consequence of Jensen's inequality, it can be show that $\bar{F}_{\tilde{R}}(r) > F_{\tilde{R}}(r)$. Indeed, since the natural logarithm is a strictly concave function, Jensen's inequality yields

$$\ln\left(E\left[F_{\tilde{R}|\boldsymbol{S}}(r|\boldsymbol{S})\right]\right) > E\left[\ln\left(F_{\tilde{R}|\boldsymbol{S}}(r|\boldsymbol{S})\right)\right],$$

where $E[\cdot]$ denotes the expectation operator. From (3.2) and (3.3) we realize that $\ln\left(F_{\tilde{R}}(r)\right) = E\left[\ln\left(F_{\tilde{R}|\boldsymbol{S}}(r|\boldsymbol{S})\right)\right]$ and $\bar{F}_{\tilde{R}}(r) = E\left[F_{\tilde{R}|\boldsymbol{S}}(r|\boldsymbol{S})\right]$, which means that $\ln\left(\bar{F}_{\tilde{R}}(r)\right) > \ln\left(F_{\tilde{R}}(r)\right)$ and hence $\bar{F}_{\tilde{R}}(r) > F_{\tilde{R}}(r)$.

From the result $\bar{F}_{\tilde{R}}(r) > F_{\tilde{R}}(r)$, it follows that exceedance probabilities will be smaller for the approximate formulation (3.3) compared to the exact formulation (3.2). This means that the formulation (3.3) will underestimate the long-term extreme values, making it a non-conservative approximation. Although the underestimation might not be significant, it is important to be aware of such an issue.

3.3 FORM formulations for long-term extremes

In this section we will show how the integrals of both formulations (3.2) and (3.3) can be solved in an approximate manner using the first order reliability method (FORM) found in connection with structural reliability analysis. In order to employ the FORM method, the formulations have to be rewritten in terms of a reliability problem. A reliability problem in the general sense is an integral written in the form

$$p_f = \int\limits_{G(\boldsymbol{v})\leq 0} f_{\boldsymbol{V}}(\boldsymbol{v})\, d\boldsymbol{v},$$

where $\boldsymbol{V}$ is a random vector with joint PDF $f_{\boldsymbol{V}}(\boldsymbol{v})$ [53]. Using reliability analysis terminology, the function $G(\boldsymbol{v})$ is referred to as the limit state function and the value of the integral p_f is called the failure probability.

3.3.1 Expressing the approximate formulation in terms of a reliability problem

That the integral (3.3) can be rewritten as a reliability problem, is well known. This is done by first rewriting

$$\bar{F}_{\tilde{R}}(r) = \int_{\boldsymbol{s}} F_{\tilde{R}|\boldsymbol{S}}(r|\boldsymbol{s})\, f_{\boldsymbol{S}}(\boldsymbol{s})\, d\boldsymbol{s} = \int_{\boldsymbol{s}} \int_{\tilde{r}\leq r} f_{\tilde{R}|\boldsymbol{S}}(\tilde{r}|\boldsymbol{s})\, d\tilde{r} f_{\boldsymbol{S}}(\boldsymbol{s})\, d\boldsymbol{s}.$$

We then define the random vector $\boldsymbol{V} = [\boldsymbol{S}, \tilde{R}]$, whose joint PDF will be $f_{\boldsymbol{V}}(\boldsymbol{v}) = f_{\tilde{R}|\boldsymbol{S}}(\tilde{r}|\boldsymbol{s})\, f_{\boldsymbol{S}}(\boldsymbol{s})$. Thus we have

$$\bar{F}_{\tilde{R}}(r) = \int\limits_{\tilde{r}\leq r} f_{\boldsymbol{V}}(\boldsymbol{v})\, d\boldsymbol{v} = 1 - \int\limits_{r-\tilde{r}\leq 0} f_{\boldsymbol{V}}(\boldsymbol{v})\, d\boldsymbol{v},$$

and defining the limit state function $G_r(\boldsymbol{v}) = r - \tilde{r} = r - v_{n+1}$ we end up with

$$\bar{F}_{\tilde{R}}(r) = 1 - \int\limits_{G_r(\boldsymbol{v})\leq 0} f_{\boldsymbol{V}}(\boldsymbol{v})\, d\boldsymbol{v} = 1 - p_f(r), \tag{3.7}$$

where $p_f(r)$ is the failure probability.

3.3.2 Expressing the exact formulation in terms of a reliability problem

The integral in (3.2) can not directly be rewritten as a reliability problem using the same approach as in Section 3.3.1, due to the fact that the factor

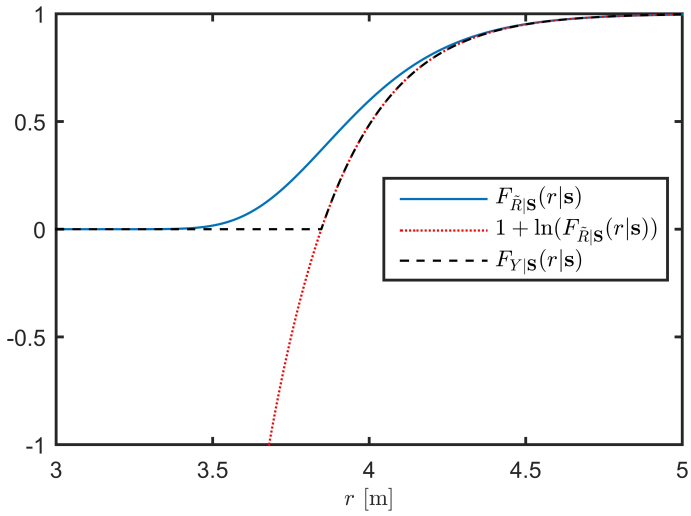

Figure 3.1: An example of the CDF $F_{Y|\boldsymbol{S}}(y|\boldsymbol{s})$ as given by (3.9), along with the short-term extreme value distribution $F_{\tilde{R}|\boldsymbol{S}}(r|\boldsymbol{s})$ and $1+\ln\left(F_{\tilde{R}|\boldsymbol{S}}(r|\boldsymbol{s})\right)$.

$\left(\ln F_{\tilde{R}|\boldsymbol{S}}\left(r|\boldsymbol{s}\right)\right)$ is not a CDF. However, the expression (3.2) can be rewritten as

$$F_{\tilde{R}}\left(r\right)=\exp\left\{\int_{\boldsymbol{s}}\left(1+\ln\left(F_{\tilde{R}|\boldsymbol{S}}\left(r|\boldsymbol{s}\right)\right)\right)f_{\boldsymbol{S}}\left(\boldsymbol{s}\right)d\boldsymbol{s}-1\right\}. \tag{3.8}$$

Now, for reasonably high levels r we have that the value of $F_{\tilde{R}|\boldsymbol{S}}\left(r|\boldsymbol{s}\right)$ will be close to one, but always less than one, and hence its logarithm is negative and close to zero. This means that $1+\ln\left(F_{\tilde{R}|\boldsymbol{S}}\left(r|\boldsymbol{s}\right)\right)$ can be viewed as a CDF for values of r such that $F_{\tilde{R}|\boldsymbol{S}}\left(r|\boldsymbol{s}\right)\geq\exp\{-1\}$, and for any given short-term condition $\boldsymbol{S}$ we can introduce the random variable Y whose CDF is given by

$$F_{Y|\boldsymbol{S}}\left(y|\boldsymbol{s}\right)=\max\left\{1+\ln\left(F_{\tilde{R}|\boldsymbol{S}}\left(y|\boldsymbol{s}\right)\right),0\right\}. \tag{3.9}$$

An example of the CDF $F_{Y|\boldsymbol{S}}(y|\boldsymbol{s})$ is given in Fig. 3.1, demonstrating how $1+\ln\left(F_{\tilde{R}|\boldsymbol{S}}(r|\boldsymbol{s})\right)$ can be viewed as a CDF for sufficiently large r. When considering long-term extreme values r, the main contribution to the integral in (3.8) will be for values of $\boldsymbol{s}$ where $F_{Y|\boldsymbol{S}}\left(r|\boldsymbol{s}\right)=1+\ln\left(F_{\tilde{R}|\boldsymbol{S}}\left(r|\boldsymbol{s}\right)\right)$, and we obtain

$$F_{\tilde{R}}\left(r\right)\approx\exp\left\{\int_{\boldsymbol{s}}F_{Y|\boldsymbol{S}}\left(r|\boldsymbol{s}\right)f_{\boldsymbol{S}}\left(\boldsymbol{s}\right)d\boldsymbol{s}-1\right\}. \tag{3.10}$$

For long-term extreme values r, (3.10) is expected to be a much better approximation to the exact long-term CDF than the formulation (3.3). This is because $F_{Y|\boldsymbol{S}}(r|\boldsymbol{s})$ exactly represents $1 + \ln\left(F_{\tilde{R}|\boldsymbol{S}}\left(r|\boldsymbol{s}\right)\right)$ for the relevant values of r, whereas $F_{\tilde{R}|\boldsymbol{S}}(r|\boldsymbol{s})$ is an approximation also for larger values of r as seen in Fig. 3.1. Now the integral (3.10) can be rewritten using the same approach as in Section 3.3.1, giving

$$F_{\tilde{R}}\left(r\right) \approx \exp\left\{-\int\limits_{G_r(\boldsymbol{v})\leq 0} f_{\boldsymbol{V}}\left(\boldsymbol{v}\right) d\boldsymbol{v}\right\} = \exp\left\{-p_f\left(r\right)\right\}, \tag{3.11}$$

where the failure probability $p_f(r)$ now is obtained using $V_{n+1} = Y$ instead of $V_{n+1} = \tilde{R}$ as in Section 3.3.1.

3.3.3 Finding the failure probability using FORM

The problem of finding the failure probability $p_f(r)$ in (3.7) and (3.11) can be solved for a given exceedance level r using the FORM method. The random vector $\boldsymbol{V}$ is transformed into a vector $\boldsymbol{U}$ of independent standard normal variables by the Rosenblatt transformation $\boldsymbol{U} = T(\boldsymbol{V})$ [53], defined by the equations

$$\Phi\left(U_1\right) = F_{V_1}\left(V_1\right), \tag{3.12a}$$
$$\Phi\left(U_i\right) = F_{V_i|V_1,\ldots,V_{i-1}}\left(V_i|V_1,\ldots,V_{i-1}\right), i = 2,\ldots,n, \tag{3.12b}$$
$$\Phi\left(U_{n+1}\right) = F_{V_{n+1}|V_1,\ldots,V_n}\left(V_{n+1}|V_1,\ldots,V_n\right), \tag{3.12c}$$

where Φ denotes the standard normal CDF. Given a point $\boldsymbol{u}$ in the standard normal space, the inverse transformation evaluated at $\boldsymbol{u}$, i.e. $\boldsymbol{v} = T^{-1}(\boldsymbol{u})$, can be found by solving the equations (3.12) successively, obtaining

$$v_1\left(\boldsymbol{u}\right) = F_{V_1}^{-1}\left(\Phi\left(u_1\right)\right), \tag{3.13a}$$
$$v_i\left(\boldsymbol{u}\right) = F_{V_i|V_1,\ldots,V_{i-1}}^{-1}\left(\Phi\left(u_i\right)|v_1\left(\boldsymbol{u}\right),\ldots,v_{i-1}\left(\boldsymbol{u}\right)\right), \tag{3.13b}$$
$$v_{n+1}\left(\boldsymbol{u}\right) = F_{V_{n+1}|V_1,\ldots,V_n}^{-1}\left(\Phi\left(u_{n+1}\right)|v_1\left(\boldsymbol{u}\right),\ldots,v_n\left(\boldsymbol{u}\right)\right). \tag{3.13c}$$

The failure probability integral is then rewritten in terms of the transformed variables as

$$p_f(r) = \int\limits_{G_r(\boldsymbol{v})\leq 0} f_{\boldsymbol{V}}\left(\boldsymbol{v}\right) d\boldsymbol{v} = \int\limits_{g_r(\boldsymbol{u})\leq 0} f_{\boldsymbol{U}}\left(\boldsymbol{u}\right) d\boldsymbol{u}, \tag{3.14}$$

where the transformed limit state function is $g_r(\boldsymbol{u}) = G_r\left(T^{-1}(\boldsymbol{u})\right) = r - v_{n+1}(\boldsymbol{u})$. Now if $g_r(\boldsymbol{u})$ is a linear function, we have that

$$p_f(r) = \int\limits_{g_r(\boldsymbol{u})\leq 0} f_{\boldsymbol{U}}(\boldsymbol{u})\, d\boldsymbol{u} = \Phi(-\beta), \tag{3.15}$$

where β is the distance from the origin to the $(n+1)$-dimensional hyperplane defined by $g_r(\boldsymbol{u}) = 0$.

The idea behind the FORM procedure is that, assuming that the failure probability is small, the formula (3.15) will still hold in an approximate sense even if $g_r(\boldsymbol{u})$ is not linear. The value β must then be found by solving the optimization problem

$$\beta = \min |\boldsymbol{u}|; \text{ subject to } g_r(\boldsymbol{u}) = 0. \tag{3.16}$$

The minimizer $\boldsymbol{u}^*$ satisfying $|\boldsymbol{u}^*| = \beta$ is also found in the procedure, and the transformed point $\boldsymbol{v}^* = T^{-1}(\boldsymbol{u}^*)$ is referred to as the design point.

If $\bar{\beta}_r$ denotes the solution of the minimization problem (3.16) when $V_{n+1} = \tilde{R}$, we have from (3.7) and (3.15) that

$$\bar{F}_{\tilde{R}}(r) \approx 1 - \Phi(-\bar{\beta}_r). \tag{3.17}$$

Similarly, if β_r denotes the solution of the minimization problem (3.16) when $V_{n+1} = Y$, we have from (3.11) and (3.15) that

$$F_{\tilde{R}}(r) \approx \exp\left\{-\Phi(-\beta_r)\right\}. \tag{3.18}$$

3.4 Solution of the extreme response by use of inverse FORM (IFORM)

3.4.1 Finding the design point using inverse FORM

As seen in Section 3.3, the CDFs $\bar{F}_{\tilde{R}}(r)$ and $F_{\tilde{R}}(r)$ can be evaluated at a given level r using FORM. However, when designing a structure one is commonly faced with the inverse problem of finding the characteristic response level r corresponding to a given exceedance probability. For instance, the M-year extreme response r_M is defined as the response level with a return

period of M years. This is found by requiring that the exceedance probability per year is $1/M$, i.e. $F_{\tilde{R}_{LT}}(r_M) = 1 - 1/M$ for a long-term period of one year. Using the relation (3.1), the equation for r_M can be expressed in terms of the short-term extreme value distribution as

$$F_{\tilde{R}}(r_M) = \left(1 - \frac{1}{M}\right)^{1/N} \approx 1 - \frac{1}{MN},$$

since the number of short-term periods N is large. If the short-term period $\tilde{T}$ is three hours and the long-term period T is one year, we have $N = 365 \cdot 8 = 2920$. As an example, the 100-year extreme response r_{100} then corresponds to the exceedance probability $1 - F_{\tilde{R}}(r_{100}) = 1/292000$.

When the exceedance probability is specified, the corresponding reliability index β in the FORM procedure is given by solving for $\bar{\beta}_r$ in (3.17) or β_r in (3.18) for the approximate and exact formulations respectively. Instead we have to find the value r_M such that the limit surface defined by $g_{r_M}(\boldsymbol{u}) = r_M - v_{n+1}(\boldsymbol{u}) = 0$, where $v_{n+1}(\boldsymbol{u})$ is given in (3.13), has a minimal distance β to the origin. According to [17, 79] this inverse FORM (IFORM) problem can be formulated as

$$r_M = \max v_{n+1}(\boldsymbol{u}); \text{ subject to } |\boldsymbol{u}| = \beta. \tag{3.19}$$

Using the method of Lagrange multipliers, we recognize that for both the problems (3.16) and (3.19) an optimal point $\boldsymbol{u}^*$ must satisfy

$$\frac{\boldsymbol{u}^*}{|\boldsymbol{u}^*|} = \frac{\nabla v_{n+1}(\boldsymbol{u}^*)}{|\nabla v_{n+1}(\boldsymbol{u}^*)|}, \tag{3.20}$$

in addition to the constraint of the specific problem. Thus, if $\boldsymbol{u}^*$ is a solution to the problem (3.19), it satisfies (3.20) and $|\boldsymbol{u}^*| = \beta$. Furthermore, r_M is given by $r_M = v_{n+1}(\boldsymbol{u}^*)$, so $g_{r_M}(\boldsymbol{u}^*) = r_M - v_{n+1}(\boldsymbol{u}^*) = 0$ and the constraint in (3.16) is also satisfied. Assuming that (3.16) has a unique solution, this shows that $\boldsymbol{u}^*$ is the minimizer for the problem (3.16) and β is indeed the minimal distance from the origin to the limit surface $g_{r_M}(\boldsymbol{u}) = r_M - v_{n+1}(\boldsymbol{u}) = 0$. In other words, a solution to the problem (3.19) is a solution to the IFORM problem.

3.4.2 Existing solution algorithms for the IFORM problem

A solution algorithm for the IFORM problem (3.19), which aims at solving (3.20) with $|\boldsymbol{u}^*| = \beta$ in an iterative manner, is proposed in [47] and applied

in [68]. This iteration is given by

$$\boldsymbol{u}^{k+1} = \beta \frac{\nabla v_{n+1}\left(\boldsymbol{u}^k\right)}{\left|\nabla v_{n+1}\left(\boldsymbol{u}^k\right)\right|}. \tag{3.21}$$

It can be shown that this is the same as using the steepest ascent method (equivalent to the steepest descent method for minimization) searching for the optimal point, i.e. the maximizer of $v_{n+1}(\boldsymbol{u})$, on the hypersphere with radius β. The gradient $\nabla v_{n+1}(\boldsymbol{u}^k)$ is projected onto the tangent plane of the sphere at the point $\boldsymbol{u}^k$, giving the direction on the sphere along which the function $v_{n+1}(\boldsymbol{u})$ increases most rapidly. The optimal point is then searched for along an arc on the sphere that follows this search direction. The updated point $\boldsymbol{u}^{k+1}$ is found as the point that maximizes $v_{n+1}(\boldsymbol{u})$ along this arc, when approximating the gradient $\nabla v_{n+1}(\boldsymbol{u})$ as constant equal to $\nabla v_{n+1}(\boldsymbol{u}^k)$. This is illustrated very nicely in [17].

The iteration (3.21) is very simple and easy to use. However, it may fail to converge to the optimal point. Due to the approximation of constant gradient $\nabla v_{n+1}(\boldsymbol{u})$ along the search direction, the updated point $\boldsymbol{u}^{k+1}$ is not guaranteed to give a sufficient increase of $v_{n+1}(\boldsymbol{u})$ and it may even give a decrease. This problem was addressed in [17] by performing an exact arc search whenever an iteration point given by (3.21) would give a decrease. The exact arc search must be performed by solving a one-dimensional optimization problem, which might require a relatively large number of function evaluations without a significant gain in the convergence rate. In the context of the present paper we strive to limit the number of function evaluations, since each function evaluation corresponds to a possibly very time-consuming short-term response analysis. Hence, a simpler method for achieving convergence is preferred.

It should be mentioned that, as an alternative, the IFORM problem (3.19) can be recast in terms of angles, resulting in in "box-like" constraints [79]. A variety of optimization algorithms can be used to solve such a problem efficiently. In this paper, however, we pursue a further development of the simple iteration (3.21) which is easy to implement.

3.4.3 A new solution algorithm for the IFORM problem

A simple method that resolves the convergence issues, while keeping the number of function evaluation to a minimum, is obtained by using a suffi-

cient increase condition along with a backtracking approach, similar to what is explained in Chapter 3.1 of [61]. We require that the increase of $v_{n+1}(\boldsymbol{u})$ when going from $\boldsymbol{u}^k$ to the updated point $\boldsymbol{u}^{k+1}$ is proportional to the step length and the directional derivative at $\boldsymbol{u}^k$ along the search direction, this is known as the Armijo condition [3, 61]. In our case the sufficient increase condition requires $\boldsymbol{u}^{k+1}$ to satisfy

$$v_{n+1}\left(\boldsymbol{u}^{k+1}\right) - v_{n+1}\left(\boldsymbol{u}^{k}\right) \geq cd\alpha. \tag{3.22}$$

Here $c \in (0,1)$ is a proportionality constant chosen as $c = 10^{-4}$ in this paper, d is the directional derivative at $\boldsymbol{u}^k$ and α is the step length measured as the distance between $\boldsymbol{u}^k$ and $\boldsymbol{u}^{k+1}$ along the sphere. These are given respectively by

$$d = \frac{1}{\beta}\sqrt{\beta^2 \left|\nabla v_{n+1}\left(\boldsymbol{u}^k\right)\right|^2 - \left(\boldsymbol{u}^k \cdot \nabla v_{n+1}\left(\boldsymbol{u}^k\right)\right)^2}, \tag{3.23}$$

and

$$\alpha = \beta \cos^{-1} \frac{\boldsymbol{u}^k \cdot \nabla v_{n+1}\left(\boldsymbol{u}^k\right)}{\beta \left|\nabla v_{n+1}\left(\boldsymbol{u}^k\right)\right|}, \tag{3.24}$$

where the dot denotes the dot product of two vectors.

A solution algorithm for the IFORM problem (3.19) where the iteration points satisfy the sufficient increase condition (3.22) is given by Algorithm 1. At each iteration the algorithm starts by trying $\boldsymbol{u}^{k+1}$ as given by (3.21), and if sufficient increase is not achieved, the backtracking approach is employed by halving the step length successively until the sufficient increase condition is satisfied. In Algorithm 1 choices have to be made for the initial point $\boldsymbol{u}^1$ and for the tolerance *Tol* of the convergence criterion $\frac{|\boldsymbol{u}^{k+1} - \boldsymbol{u}^k|}{|\boldsymbol{u}^{k+1}|} < Tol$. In this paper $\boldsymbol{u}^1 = [\boldsymbol{0}, \beta]$ and $Tol = 10^{-3}$ have been used. These choices serve to demonstrate the efficiency of the method, but other choices may be more appropriate and give faster convergence.

Algorithm 1 Solution algorithm for the IFORM problem (3.19) where the iteration points satisfy the sufficient increase condition (3.22).

Choose $Tol > 0$ and $\boldsymbol{u}^1$ with $|\boldsymbol{u}^1| = \beta$;
Set $Convergence \leftarrow$ FALSE;
Set $k \leftarrow 1$;
while $Convergence =$ FALSE **do**
  Choose $c \in (0, 1)$;
  Evaluate $v_{n+1}(\boldsymbol{u}^k)$ and $\nabla v_{n+1}(\boldsymbol{u}^k)$;
  Calculate directional derivative d using (3.23);
  Calculate initial step length α using (3.24);
  $\boldsymbol{u}^{k+1} \leftarrow \beta \frac{\nabla v_{n+1}(\boldsymbol{u}^k)}{|\nabla v_{n+1}(\boldsymbol{u}^k)|}$;
  Evaluate $v_{n+1}(\boldsymbol{u}^{k+1})$;
  while $v_{n+1}\left(\boldsymbol{u}^{k+1}\right) - v_{n+1}\left(\boldsymbol{u}^k\right) < cd\alpha$ **do**
    $\alpha \leftarrow \alpha/2$;
    $\boldsymbol{u}^{k+1} \leftarrow \beta \frac{\boldsymbol{u}^{k+1}+\boldsymbol{u}^k}{|\boldsymbol{u}^{k+1}+\boldsymbol{u}^k|}$;
    Evaluate $v_{n+1}(\boldsymbol{u}^{k+1})$;
  end while
  if $\frac{|\boldsymbol{u}^{k+1}-\boldsymbol{u}^k|}{|\boldsymbol{u}^{k+1}|} < Tol$ **then**
    $\boldsymbol{u}^* \leftarrow \boldsymbol{u}^{k+1}$;
    $Convergence \leftarrow$ TRUE;
  end if
  Set $k \leftarrow k + 1$;
end while

3.5 An SDOF example

3.5.1 The response model

As an example we consider the stochastic response $R(t)$ of a linear, time-invariant single-degree-of-freedom (SDOF) system due to a wave elevation process $\eta(t)$, which is assumed to be stationary and Gaussian with zero mean for given environmental parameters $\boldsymbol{s}$. This means that, given $\boldsymbol{s}$, $R(t)$ will also be stationary and Gaussian with zero mean. The SDOF system is described in the frequency domain by the transfer function

$$H_{\eta R}(\omega) = \left(1 - \left(\frac{\omega}{\omega_n}\right)^2 + i2\zeta\frac{\omega}{\omega_n}\right)^{-1},$$

where $\zeta = 0.05$ is the damping ratio and ω_n is the natural frequency. We use the environmental parameters $\boldsymbol{S} = [H_s, T_z]$, where H_s is the significant wave height and T_z is the zero-crossing period, and specify the wave elevation process by the generalized Pierson-Moskowitz spectrum [73] given by

$$S_{\eta|\boldsymbol{S}}(\omega|\boldsymbol{s}) = S_{\eta|H_s,T_z}(\omega|h_s,t_z) = \frac{{h_s}^2 t_z}{8\pi^2}\left(\frac{\omega t_z}{2\pi}\right)^{-5}\exp\left\{-\frac{1}{\pi}\left(\frac{\omega t_z}{2\pi}\right)^{-4}\right\}.$$

Now the response spectrum $S_{R|\boldsymbol{S}}(\omega|\boldsymbol{s})$ is obtained by the well known relationship [60]

$$S_{R|\boldsymbol{S}}(\omega|\boldsymbol{s}) = |H_{\eta R}(\omega)|^2 S_{\eta|\boldsymbol{S}}(\omega|\boldsymbol{s}).$$

Figure 3.2 shows the wave spectrum $S_\eta(\omega)$ plotted in the nondimensional scale $\omega T_z/2\pi$. Figure 3.3 shows the absolute value $|H_{\eta R}(\omega)|$ of the transfer function for different values of $\omega_n T_z/2\pi$ using the same scale as for the wave spectrum.

3.5.2 The environmental model

The CDF of the significant wave height H_s is given by a 2-parameter Weibull distribution

$$F_{H_s}(h) = 1 - \exp\left\{-\left(\frac{h}{\alpha}\right)^\beta\right\}, \tag{3.25}$$

and the zero-crossing period T_z has a conditioned lognormal distribution

$$F_{T_z|H_s}(t|h) = \Phi\left(\frac{\ln t - \mu(h)}{\sigma(h)}\right), \tag{3.26}$$

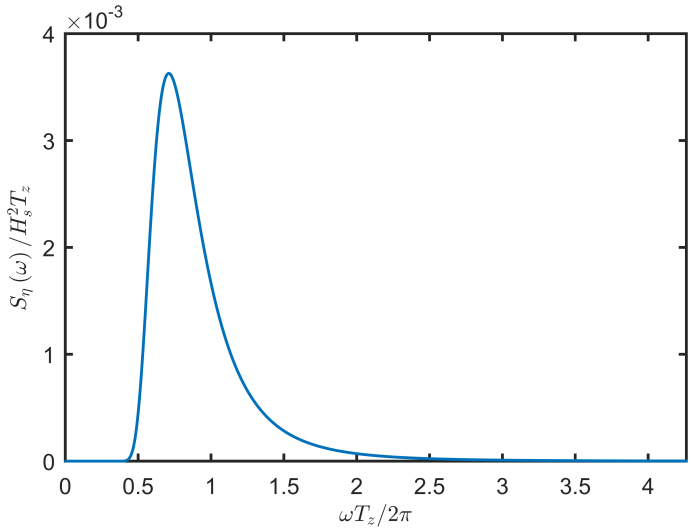

Figure 3.2: The generalized Pierson-Moskowitz spectrum.

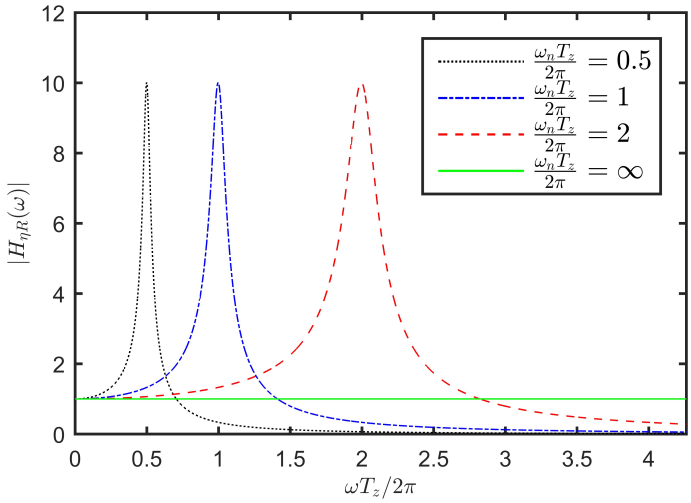

Figure 3.3: The absolute value $|H_{\eta R}(\omega)|$ of the transfer function.

where $\mu(h) = a_0 + a_1 h^{a_2}$ and $\sigma(h) = b_0 + b_1 e^{b_2 h}$. This is a model for the environmental parameters that is recommended in [14], and in this paper we use the parameter values $\alpha = 1.76$, $\beta = 1.59$, $a_0 = 0.70$, $a_1 = 0.282$, $a_2 = 0.167$, $b_0 = 0.07$, $b_1 = 0.3449$ and $b_2 = -0.2073$. The PDFs $f_{H_s}(h)$ and $f_{T_z|H_s}(t|h)$ can be obtained by differentiating (3.25) and (3.26) with respect to h and t respectively, giving the joint PDF of the environmental parameters as

$$f_{\boldsymbol{S}}(\boldsymbol{s}) = f_{H_s,T_z}(h,t) = f_{H_s}(h)\, f_{T_z|H_s}(t|h)\,.$$

This way of establishing the joint environmental model is referred to as the conditional modelling approach [8, 14]. The joint PDF $f_{\boldsymbol{S}}(\boldsymbol{s}) = f_{H_s,T_z}(h,t)$ is presented in Fig. 3.4.

3.5.3 The short-term extreme value distribution

Since $R(t)|\boldsymbol{S}$ is stationary and Gaussian with zero mean, the mean frequency of r-upcrossings is given by

$$\nu(r|\boldsymbol{s}) = \frac{1}{2\pi}\sqrt{\frac{m_2(\boldsymbol{s})}{m_0(\boldsymbol{s})}}\exp\left\{-\frac{r^2}{2m_0(\boldsymbol{s})}\right\},$$

where the ith moment $m_i(\boldsymbol{s})$ of the response spectrum $S_{R|\boldsymbol{S}}(\omega|\boldsymbol{s})$ is defined as

$$m_i(\boldsymbol{s}) = \int_0^\infty \omega^i S_{R|\boldsymbol{S}}(\omega|\boldsymbol{s})\, d\omega. \tag{3.27}$$

Now if $\tilde{R}|\boldsymbol{S}$ denotes the largest value of the response process $R(t)$ during a short term period of $\tilde{T} = 3$h with given environmental parameters, and we assume independent upcrossings of high levels, then the short-term extreme peak CDF is given by (3.4). Thus we have the expression

$$F_{\tilde{R}|\boldsymbol{S}}(r|\boldsymbol{s}) = \exp\left\{-\nu(r|\boldsymbol{s})\,\tilde{T}\right\} = \exp\left\{-\frac{\tilde{T}}{2\pi}\sqrt{\frac{m_2(\boldsymbol{s})}{m_0(\boldsymbol{s})}}\exp\left\{-\frac{r^2}{2m_0(\boldsymbol{s})}\right\}\right\}, \tag{3.28}$$

which holds for reasonably large values of r.

3.5.4 The FORM formulations

In this example we have that $\boldsymbol{V} = [\boldsymbol{S}, V_3] = [H_s, T_z, V_3]$, where $V_3 = \tilde{R}$ for the FORM formulation (3.7) in Section 3.3.1, whereas $V_3 = Y$ for the FORM

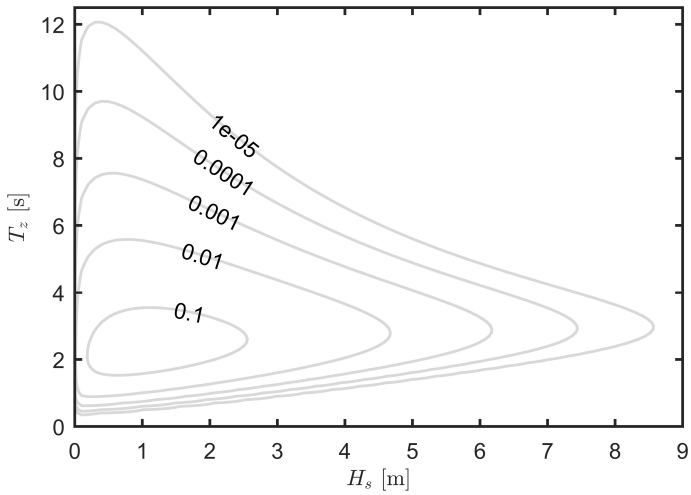

Figure 3.4: The joint PDF of the environmental parameters presented by its isoprobability contours.

formulation (3.11) in Section 3.3.2. Now given a point $\boldsymbol{u} = [u_1, u_2, u_3]$ in the standard normal space, the corresponding point $\boldsymbol{v} = [h(\boldsymbol{u}), t(\boldsymbol{u}), v_3(\boldsymbol{u})] = T^{-1}(\boldsymbol{u})$ is evaluated using (3.13), which in this case takes the form

$$
\begin{aligned}
h(\boldsymbol{u}) &= F_{H_s}^{-1}\left(\Phi\left(u_1\right)\right) = \alpha[-\ln\left(1-\Phi\left(u_1\right)\right)]^{1/\beta}, \\
t(\boldsymbol{u}) &= F_{T_z|H_s}^{-1}\left(\Phi\left(u_2\right)|h(\boldsymbol{u})\right) = \exp\left\{\mu\left(h\left(\boldsymbol{u}\right)\right) + \sigma\left(h\left(\boldsymbol{u}\right)\right) u_2\right\}, \\
v_3(\boldsymbol{u}) &= F_{V_3|T_z,H_s}^{-1}\left(\Phi\left(u_3\right)|h(\boldsymbol{u}), t(\boldsymbol{u})\right).
\end{aligned}
$$

Using (3.28) we find that when $V_3 = \tilde{R}$ we have

$$
\begin{aligned}
v_3\left(\boldsymbol{u}\right) &= \tilde{r}\left(\boldsymbol{u}\right) \\
&= \sqrt{-2m_0\left(h\left(\boldsymbol{u}\right), t\left(\boldsymbol{u}\right)\right) \ln\left(-\frac{2\pi}{\tilde{T}}\sqrt{\frac{m_0\left(h\left(\boldsymbol{u}\right), t\left(\boldsymbol{u}\right)\right)}{m_2\left(h\left(\boldsymbol{u}\right), t\left(\boldsymbol{u}\right)\right)}}\ln\Phi\left(u_3\right)\right)},
\end{aligned}
$$

and in the case $V_3 = Y$ we find from (3.9) that

$$
F_{Y|\boldsymbol{S}}^{-1}\left(\Phi\left(u_3\right)|\boldsymbol{s}\right) = F_{\tilde{R}|\boldsymbol{S}}^{-1}\left(e^{\Phi(u_3)-1}|\boldsymbol{s}\right),
$$

which yields

$$v_3(\boldsymbol{u}) = y(\boldsymbol{u}) = \sqrt{-2m_0\left(h(\boldsymbol{u}), t(\boldsymbol{u})\right) \ln\left(\frac{2\pi}{\tilde{T}}\sqrt{\frac{m_0\left(h(\boldsymbol{u}), t(\boldsymbol{u})\right)}{m_2\left(h(\boldsymbol{u}), t(\boldsymbol{u})\right)}}\left(1-\Phi\left(u_3\right)\right)\right)}.$$

We note that each evaluation of the function $v_3(\boldsymbol{u})$ requires one short-term response analysis since the response spectrum $S_{R|\boldsymbol{S}}(\omega|\boldsymbol{s})$ must be calculated for the environmental variables $\boldsymbol{s} = [h(\boldsymbol{u}), t(\boldsymbol{u})]$ in order to calculate the required moments $m_0(h(\boldsymbol{u}), t(\boldsymbol{u}))$ and $m_2(h(\boldsymbol{u}), t(\boldsymbol{u}))$. Having established the expression for $v_3(\boldsymbol{u})$ the transformed limit state function $g_r(\boldsymbol{u})$ in (3.14) is given by

$$g_r(\boldsymbol{u}) = r - v_3(\boldsymbol{u}).$$

3.6 Numerical results

Algorithm 1 was implemented in MATLAB [74] for calculation of the IFORM approximations to the M-year extreme response of the SDOF example described in Section 3.5. The IFORM solutions obtained when the exact formulation (3.2) and the approximate formulation (3.3) were used are denoted by r_M^{I} and $\bar{r}_M^{\mathrm{I}}$ respectively.

3.6.1 One-parameter environmental distribution

For illustration purposes we first consider a simplified environmental model obtained by regarding the zero-crossing period T_z as deterministic, given by the conditional median $T_z|H_s = \exp\{\mu(H_s)\}$. This means that H_s is the only environmental variable, and the solution of the IFORM problem (3.19) can be illustrated in two dimensions. In this case the IFORM problem (3.19) is that of finding the maximal value of $v_{n+1}(\boldsymbol{u})$ when $\boldsymbol{u}$ is constrained to the circle of radius β. When the exact formulation is used we have that $v_{n+1}(\boldsymbol{u}) = y(\boldsymbol{u})$. For the 100-year response r_{100}^{I} the value of β corresponds to an exceedance probability of $1/(2920 \cdot 100)$ and, as described in Section 3.4.1, β can be found from (3.18) as

$$\beta = -\Phi^{-1}\left(-\ln\left[1-\frac{1}{292000}\right]\right) = 4.498.$$

Figure 3.5 shows how r_{100}^{I} is obtained for the case $\omega_n = 2.0$ rad/s by using Algorithm 1. The circle of radius β is shown along with the level curves of

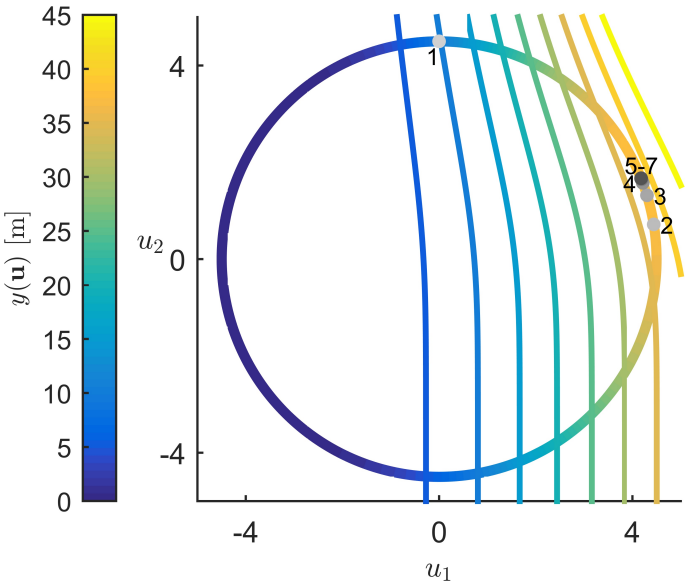

Figure 3.5: The iteration points obtained when solving the maximization problem (3.19) for finding the 100-year response r_{100}^{I} in the case that the simplified environmental model is used and $\omega_n = 2.0$ rad/s. The circle of radius β is shown along with the level curves of the function $y(\boldsymbol{u})$, with a colouring corresponding to the value of $y(\boldsymbol{u})$.

the function $y(\boldsymbol{u})$, with a colouring corresponding to the value of $y(\boldsymbol{u})$. We observe that after six iterations we have convergence to the optimal point $\boldsymbol{u}^*$ where the level curve of $y(\boldsymbol{u})$ through the point is tangent to the circle. In this case the standard iteration (3.21) did converge, and the backtracking part of Algorithm 1 remained idle. At $\boldsymbol{u}^* = [4.17, 1.67]$ the function $y(\boldsymbol{u})$ attains its maximal value on the circle, 38.13 m, and the design point is obtained as $\boldsymbol{v}^* = T^{-1}(\boldsymbol{u}^*) = [h^*, y^*] = [8.01 \text{ m}, 38.13 \text{ m}]$. Thus $r_{100}^{\mathrm{I}} = 38.13$ m when the simplified environmental model is used.

3.6.2 The backtracking approach

In order to demonstrate the need for the backtracking approach in Algorithm 1 for stabilizing the iteration (3.21), the 100-year response r_{100}^{I} was calculated for the case $\omega_n = 2.0$ rad/s. In Fig. 3.6 it is shown how the maximization problem (3.19) is solved in an iterative manner. When both H_s and T_z are considered as random variables in the environmental

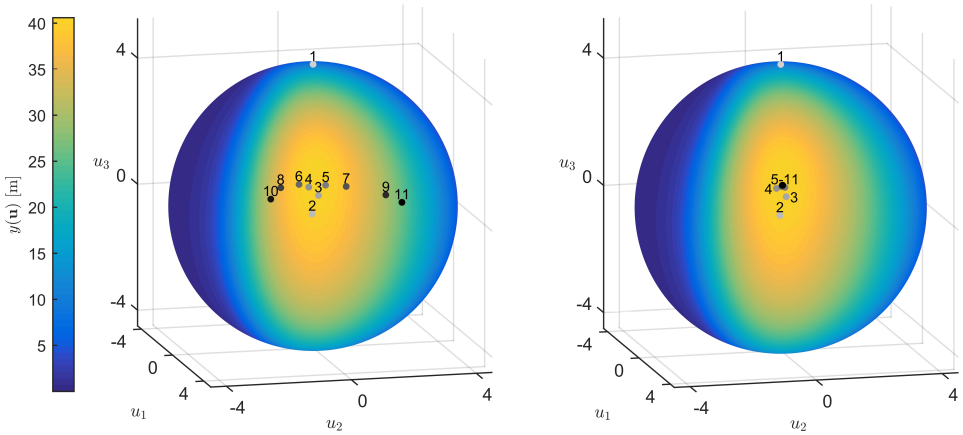

Figure 3.6: The iteration points obtained when solving the maximization problem (3.19) for finding the 100-year response r_{100}^{I} in the case $\omega_n = 2.0$ rad/s. The iteration (3.21) is used with (right) and without (left) the backtracking approach.

model, we seek the maximal value of $v_{n+1}(\boldsymbol{u})$ on the sphere of radius β. The left part of Fig. 3.6 shows the iteration points obtained when the standard iteration (3.21) was used, without applying the backtracking approach. In this case the iteration clearly diverges, failing to converge towards the optimal point. The result of employing the backtracking approach is shown to the right in Fig. 3.6. We observe that the backtracking prevents the diverging behaviour and the iteration converges after ten iterations to the optimal point $\boldsymbol{u}^* = [4.09, -0.96, 1.60]$, which yields the design point $\boldsymbol{v}^* = T^{-1}(\boldsymbol{u}^*) = [h^*, t^*, v_3^*] = [7.84 \text{ m}, 2.62 \text{ s}, 40.54 \text{ m}]$ and thus $r_{100}^{\mathrm{I}} = 40.54$ m.

3.6.3 The long-term extreme response approximations

In order to investigate the accuracy of the IFORM approximations r_M^{I} and $\bar{r}_M^{\mathrm{I}}$ for the extreme response, the formulations (3.2) and (3.3) were calculated in an exact manner using numerical integration and the exact values r_M and $\bar{r}_M$ were obtained. Thus r_M is the exact M-year extreme response, $\bar{r}_M$ is the extreme response given by the approximate formulation, and r_M^{I} and $\bar{r}_M^{\mathrm{I}}$ are the respective IFORM approximations. We would also like to investigate how accurate the approximate formulation (3.3) is with respect to extreme responses.

In Table 3.1, Table 3.2 and Table 3.3 the M-year extreme response r_M and its approximations are calculated for $M = 10$, $M = 100$ and $M = 1000$ respectively, and the relative errors of the approximations are also displayed. The extreme response is calculated for different values of ω_n, thereby varying the characteristics of the SDOF system. Also, for the IFORM approximations the number of required short-term response calculations n_{st} is given, i.e. the number of evaluations of the function $v_{n+1}(\boldsymbol{u})$ in Algorithm 1. For each iteration $n + 2$ evaluations are needed to calculate $v_{n+1}(\boldsymbol{u}^k)$ and $\nabla v_{n+1}(\boldsymbol{u}^k)$ using a finite difference approximation, in addition to the evaluations of $v_{n+1}(\boldsymbol{u}^{k+1})$ which is one for each backtracking step.

Comparing the results obtained using full numerical integration we see that the approximate formulation (3.3) does indeed underestimate the extreme response values, demonstrating what was shown in Section 3.2.3. However, the error of the approximation is in most cases within a few percent, and it decreases with increasing return period, i.e. decreasing exceedance probability.

For the IFORM approximations we notice that the difference between using the exact and the approximate formulation is in fact very small, and both IFORM methods give reasonably good estimates for the M-year response r_M. In most of the cases considered here, using IFORM actually improves the estimate compared to full integration of the approximate formulation. However, whether this is the case will be structure dependent. Regarding the number of short-term structural response analyses n_{st}, this appears to be around 50, although some cases display faster or slower convergence resulting in smaller or larger values of n_{st}. This number of analyses is expected to be the same if a more complex structure is considered, making a full long-term response analysis feasible also when short-term response calculations are time demanding.

Finally, a plot showing the design points obtained in the calculation of the IFORM approximations r_M^{I} is given in Fig. 3.7 along with the distribution of the environmental parameters. This demonstrates that the IFORM solution by Algorithm 1 also produces a set of environmental variables representing the main contribution to the long-term extreme response, and this set can be quite different for the different cases.

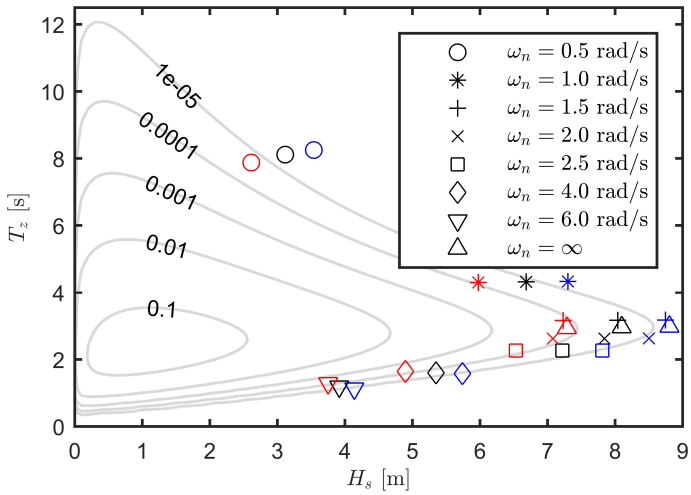

Figure 3.7: The design points corresponding to the M-year response for $M = 10$ (red), $M = 100$ (black) and $M = 1000$ (blue), along with the PDF of the environmental parameters.

3.7 Concluding remarks

An exact and an approximate formulation for the long-term extreme response of marine structures have been discussed and compared in this paper. It has been shown that the approximate formulation is non-conservative in the sense that it underestimates the long-term extreme response values. It has also been shown how both formulations can be solved in an approximate manner using FORM, and extreme response values can be obtained by IFORM. Finally, a new solution algorithm for the IFORM problem has been proposed which resolves some convergence issues of a well-established iteration algorithm.

Numerical results have also been presented, demonstrating the proposed solution algorithm and comparing it with the standard iteration algorithm. The different approximations for the long-term extreme response have been compared for an SDOF example in order to assess the accuracy of the approximations. It is found that both IFORM approximations give reasonably good estimates for the long-term extreme response. The number of required short-term response analyses for the IFORM method is found to be within acceptable limits, making a full long-term extreme response analysis feasible also for more complex structures.

Table 3.1: The 10-year extreme response r_M, $M = 10$, and its approximations $\bar{r}_M$, r_M^{I} and $\bar{r}_M^{\mathrm{I}}$, along with the relative errors of the approximations. For the IFORM approximations the number of required short-term response calculations n_{st} is also given.

	Full integration			IFORM approximations					
	Ex. for.	Approx. for.		Exact formulation			Approximate formulation		
ω_n [rad/s]	r_M [m]	$\bar{r}_M$ [m]	$\frac{\bar{r}_M - r_M}{r_M}$	r_M^{I} [m]	$\frac{r_M^{\mathrm{I}} - r_M}{r_M}$	n_{st}	$\bar{r}_M^{\mathrm{I}}$ [m]	$\frac{\bar{r}_M^{\mathrm{I}} - r_M}{r_M}$	n_{st}
0.5	9.78	8.29	−15.2%	9.63	−1.5%	117	9.53	−2.5%	105
1.0	26.97	25.84	−4.2%	27.37	1.5%	74	27.27	1.1%	64
1.5	35.96	34.74	−3.4%	36.04	0.2%	68	35.94	−0.1%	59
2.0	35.46	34.33	−3.2%	35.39	−0.2%	47	35.30	−0.4%	38
2.5	31.69	30.69	−3.2%	31.54	−0.5%	45	31.45	−0.8%	37
4.0	21.18	20.32	−4.1%	20.79	−1.9%	30	20.71	−2.2%	27
6.0	13.79	13.01	−5.7%	13.01	−5.7%	41	12.94	−6.2%	37
∞	8.54	8.28	−3.0%	8.26	−3.2%	25	8.24	−3.5%	21

Table 3.2: The 100-year extreme response r_M, $M = 100$, and its approximations $\bar{r}_M$, r_M^{I} and $\bar{r}_M^{\mathrm{I}}$, along with the relative errors of the approximations. For the IFORM approximations the number of required short-term response calculations n_{st} is also given.

	Full integration			IFORM approximations					
	Ex. for.	Approx. for.		Exact formulation			Approximate formulation		
ω_n [rad/s]	r_M [m]	$\bar{r}_M$ [m]	$\frac{\bar{r}_M - r_M}{r_M}$	r_M^{I} [m]	$\frac{r_M^{\mathrm{I}} - r_M}{r_M}$	n_{st}	$\bar{r}_M^{\mathrm{I}}$ [m]	$\frac{\bar{r}_M^{\mathrm{I}} - r_M}{r_M}$	n_{st}
0.5	11.93	11.06	−7.3%	12.45	4.3%	124	12.38	3.7 %	105
1.0	31.06	30.43	−2.0%	31.88	2.6%	85	31.83	2.5 %	75
1.5	41.00	40.31	−1.7%	41.53	1.3%	63	41.48	1.2 %	54
2.0	40.22	39.60	−1.5%	40.59	0.9%	47	40.54	0.8 %	38
2.5	35.86	35.31	−1.5%	36.11	0.7%	46	36.07	0.6 %	37
4.0	23.98	23.49	−2.0%	24.00	0.1%	47	23.96	−0.1 %	38
6.0	15.70	15.17	−3.4%	15.39	−2.0%	53	15.34	−2.3 %	48
∞	9.67	9.52	−1.5%	9.49	−1.8%	29	9.48	−1.9 %	21

Table 3.3: The 1000-year extreme response r_M, $M = 1000$, and its approximations $\bar{r}_M$, r_M^{I} and $\bar{r}_M^{\mathrm{I}}$, along with the relative errors of the approximations. For the IFORM approximations the number of required short-term response calculations n_{st} is also given.

	Full integration			IFORM approximations					
	Ex. for.	Approx. for.		Exact formulation			Approximate formulation		
ω_n [rad/s]	r_M [m]	$\bar{r}_M$ [m]	$\frac{\bar{r}_M - r_M}{r_M}$	r_M^{I} [m]	$\frac{r_M^{\mathrm{I}} - r_M}{r_M}$	n_{st}	$\bar{r}_M^{\mathrm{I}}$ [m]	$\frac{\bar{r}_M^{\mathrm{I}} - r_M}{r_M}$	n_{st}
0.5	14.13	13.64	−3.5%	15.05	6.5%	135	15.01	6.2%	90
1.0	35.21	34.86	−1.0%	36.29	3.1%	85	36.27	3.0%	75
1.5	46.09	45.73	−0.8%	46.92	1.8%	53	46.90	1.7%	43
2.0	45.03	44.71	−0.7%	45.68	1.4%	47	45.66	1.4%	42
2.5	40.07	39.78	−0.7%	40.57	1.3%	42	40.55	1.2%	42
4.0	26.79	26.53	−1.0%	27.09	1.1%	48	27.07	1.0%	48
6.0	17.65	17.31	−1.9%	17.70	0.3%	75	17.67	0.1%	65
∞	10.81	10.73	−0.7%	10.70	−1.0%	26	10.70	−1.0%	25

Paper III:

Is not included due to copyright

Paper IV:

CHAPTER 5

Long-term extreme response analysis of a long-span pontoon bridge

Finn-Idar G. Giske, Knut Andreas Kvåle,
Bernt J. Leira, Ole Øiseth

Published in *Marine Structures* 58(2018), pp. 154-171.
doi:10.1016/j.marstruc.2017.11.010

Abstract

For the assessment of extreme load effects needed in design of marine structures, a full long-term analysis is recognized as the most accurate approach. However, due to the very large number of structural response analyses traditionally needed for this approach, the computational effort is usually considered to increase above acceptable levels for complex structures such as floating bridges. In this paper, a framework for full long-term extreme response analysis is demonstrated for a long-span pontoon bridge subjected to wave loads. This framework utilizes some recently developed approaches which are based on the inverse first- and second-order reliability methods (IFORM and ISORM). Using the IFORM and ISORM approaches, characteristic values of the long-term extreme response are calculated in an efficient manner. By comparing with results obtained by full numerical integration, the accuracy of the methods is investigated. Particularly the ISORM method is seen to provide high accuracy. The full long-term analysis is also compared with the environmental contour method.

5.1 Introduction

Fjord crossing technology is currently a research topic of high interest in Norway. Due to the width and depth of the fjords considered, floating bridges represent very relevant concepts as they utilize bouyancy for vertical support. The design of more extreme yet reliable fjord crossing structures motivates development of the methods for long-term stochastic extreme response analysis.

For the evaluation of extreme response of marine structures due to environmental loads, a full long-term analysis is recognized as the most accurate design approach [60]. In principle, the full long-term approach takes into account all possible combinations of environmental parameters. This means that for straightforward methods such as full numerical integration and crude Monte Carlo simulation, a very large number of short-term response calculations have to be conducted. For complex structures like floating bridges, each short-term calculation is usually very time consuming, and the full long-term approach is often considered infeasible.

As an alternative to performing full long-term analyses, the environmental contour method [29, 30] is a widely used simplified approach. First, environmental contours corresponding to specified annual exceedance probabilities are determined without any consideration of the structural response. Traditionally the contours are determined using an inverse first-order reliability method (IFORM) approach [79], but alternative methods do exist [32, 33, 55]. The most critical point along the contour is then determined, and an estimate for the long-term extreme response is finally obtained. Only a few short-term response calculations are used, making the environmental contour method highly efficient. However, some sort of calibration against full long-term analysis is required [60]. Also, due to simplified modelling of response variability, the environmental contour method may perform poorly for certain types of structures [2, 48].

In recent years, efforts have been made to reduce the number of short-term calculations required for full long-term extreme response evaluation. These are based on the observation that many combinations of environmental parameters contribute little or nothing to the long-term extreme response. A copula based environmental modelling approach is proposed in [80], and the copula concept is further utilized in an adaptive refinement algorithm for more efficient long-term integration. In [68] an IFORM approach [79] is

used to provide an estimate of the long-term extreme response. The IFORM method also indicates where the largest contribution to the long-term response is located, and this information is used in an importance sampling Monte Carlo simulation approach, improving the accuracy of the extreme response estimate. Further investigation of IFORM as a method for long-term extreme response estimation is carried out in [21], and in [23] an inverse second-order reliability method (ISORM) approach is proposed. These developments provide methods for carrying out full long-term analyses with a limited amount of short-term response calculations.

IFORM and ISORM are efficient and easily implemented methods, which is important for their practical application to long-term extreme response analysis. Still, it should be noted that having the long-term extreme response analysis formulated in terms of a reliability problem, as described in [21], a variety of methods from the field of structural reliability can also be applied. In particular, efficient simulation methods such as importance sampling [4, 67] and subset simulation [5, 11] could be used iteratively to calculate characteristic response values. Alternatively, efficient methods for reliability-based design optimization (RBDO), e.g. [18], could be used for direct calculation.

The long-term analysis can also be made more efficient by improving the efficiency of each short-term response calculation. One example is the method described in [20], which is demonstrated in [25] for pontoon bridges.

In the present paper it is shown how these recent developments can be used to perform full long-term extreme response analyses for a pontoon floating bridge subjected to first-order wave loads. Specifically, the inverse reliability approaches IFORM and ISORM [21, 23] are applied. It is demonstrated that the efficiency of these methods make full long-term extreme response analyses feasible, also for complex structures such as floating bridges. Furthermore, the framework proposed in this paper can be used for calibration of the environmental contour method.

5.2 Modelling the stochastic dynamic response of pontoon bridges

5.2.1 Stochastic modelling of waves

For a short-term period of duration $\tilde{T}$, the sea elevation is modelled as a homogeneous and stationary stochastic process with zero mean. The sea elevation process is denoted $\eta(x, y, t)$, where x, y are the spatial variables and t is the time variable. Assuming linear wave theory, the wave number $\kappa(\omega)$ is a function of angular frequency defined by the dispersion relation $\omega^2 = \kappa g \tanh(\kappa d)$, and the cross-spectral density between the wave elevation at two points (x_m, y_m) and (x_n, y_n) can be expressed in terms of a one-dimensional wave spectrum $S_\eta(\omega)$ and a spreading function $\Psi(\theta, \omega)$ as

$$S_{mn}(\omega) = S_\eta(\omega) \int_{-\pi}^{\pi} \Psi(\theta, \omega)\, e^{-i\kappa(\omega)(\Delta x \cos\theta + \Delta y \sin\theta)} d\theta.$$

Here $\Delta x = x_m - x_n$ and $\Delta y = y_m - y_n$ are the spatial separations of the points. For details we refer to [20].

The sea elevation is further assumed to be a Gaussian process which means that the cross-spectral densities provide a complete description of the process. Hence the wave situation is completely described by the wave spectrum $S_\eta(\omega)$ and the spreading function $\Psi(\theta, \omega)$. Various theoretical models given in terms of environmental parameters exist in the literature [28, 73]. In this paper we use the generalized Pierson-Moskowitz spectrum [73] given by

$$S_\eta(\omega) = \frac{{H_s}^2 T_z}{8\pi^2} \left(\frac{\omega T_z}{2\pi}\right)^{-5} \exp\left\{-\frac{1}{\pi}\left(\frac{\omega T_z}{2\pi}\right)^{-4}\right\},$$

where H_s is the significant wave height and T_z is the zero-crossing period. The spreading function is of the *cos-2s* type, defined by a mean wave direction $\bar{\Theta}$ relative to the x-axis and an ω-dependent spreading parameter $s(\omega)$ as

$$\Psi(\theta, \omega) = \frac{2^{2s(\omega)} \Gamma^2(s(\omega)+1)}{2\pi\Gamma(2s(\omega)+1)} \left(\cos^2 \frac{\theta - \bar{\Theta}}{2}\right)^{s(\omega)},$$

where $\Gamma(\cdot)$ is the gamma function. Figure 5.1 shows the wave spectrum $S_\eta(\omega)$ plotted in the nondimensional scale $\omega T_z/2\pi$, and the spreading function is shown for different values of $s(\omega)$. In this paper we have used a constant spreading $s(\omega) = 10$, but it could equally well be defined as ω-dependent.

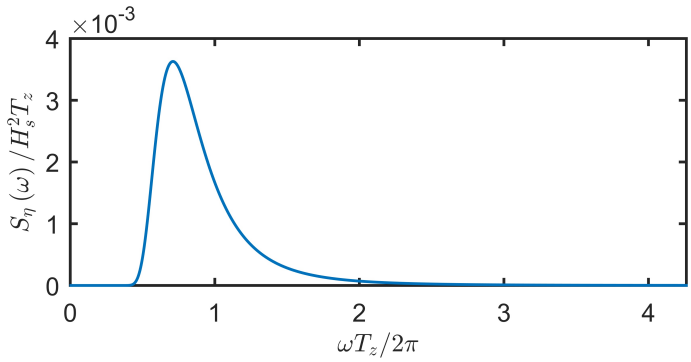

(a) The generalized Pierson-Moskowitz spectrum.

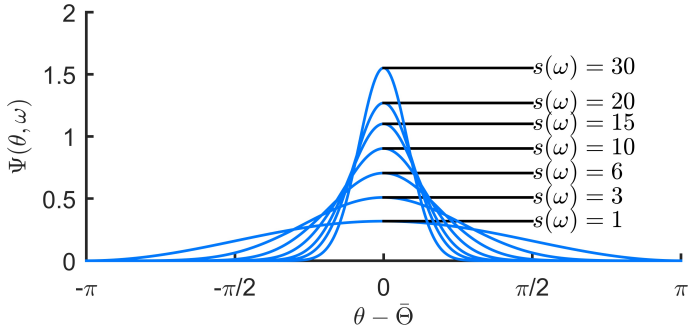

(b) The *cos-2s* spreading function.

Figure 5.1: Definition of the directional spectrum.

5.2.2 Stochastic modelling of first-order wave excitation loads

For pontoon floating bridges the structure will experience wave loads only where the pontoons are located. Considering the pontoons as rigid bodies, the bridge will experience loads in six degrees of freedom (DOFs) from each pontoon, three translational DOFs and three rotational DOFs. Thus, for a bridge with N pontoons we have loading in $6N$ DOFs, and we can define a wave excitation load vector $\boldsymbol{q}(t) = [\boldsymbol{q}_1(t), \boldsymbol{q}_2(t), \ldots, \boldsymbol{q}_N(t)]$, where $\boldsymbol{q}_m(t)$ denotes the 6-element load vector of pontoon number m. The individual components of the load vector $\boldsymbol{q}(t)$ can be denoted by $q_\mu(t)$, assigning a global index $\mu \in \{1, 2, \ldots, 6N\}$ to each DOF.

Consider pontoon m with a local coordinate system $(\tilde{x}, \tilde{y})$, which is located with its origin at the point (x_m, y_m) and rotated counterclockwise with an angle α_m relative to the global coordinate system (x, y) as shown in Fig. 5.2. The wave excitation loads due to a regular wave with angular frequency ω in the direction $\tilde{\beta}$ relative to the $\tilde{x}$-axis of the pontoon can be computed using linear potential theory software such as WADAM [16]. The loads are then reported in terms of the 6-element complex transfer function vector $\boldsymbol{f}_m(\tilde{\beta}, \omega)$. Considering only first-order wave loads, the wave excitation load process $\boldsymbol{q}_m(t)$ corresponding to the wave elevation process $\eta(x, y, t)$ can be obtained by superposition of loads from regular waves. This results in a stationary Gaussian load process $\boldsymbol{q}(t)$ with zero mean and a $6N$-by-$6N$ cross-spectral density matrix $\boldsymbol{S}_{\boldsymbol{q}}(\omega)$ whose elements are given by

$$S_{q_\mu q_\nu}(\omega) = S_\eta(\omega) \int_{-\pi}^{\pi} \Psi(\theta, \omega) f_\mu(\theta - \alpha_m, \omega) \overline{f_\nu(\theta - \alpha_n, \omega)} e^{-i\kappa(\omega)(\Delta x \cos\theta + \Delta y \sin\theta)} d\theta, \tag{5.1}$$

where the overline denotes complex conjugation. Here $f_\mu(\tilde{\beta}, \omega)$ is the μ-th component of the total transfer function vector

$$\boldsymbol{f}(\tilde{\beta}, \omega) = [\boldsymbol{f}_1(\tilde{\beta}, \omega), \boldsymbol{f}_2(\tilde{\beta}, \omega), \cdots, \boldsymbol{f}_N(\tilde{\beta}, \omega)],$$

i.e. the complex transfer function of the DOF μ.

A method for efficient calculation of the cross-spectral density matrix $\boldsymbol{S}_{\boldsymbol{q}}(\omega)$ based on the expression Eqn. (5.1) is given in [20, 25]. In [20] the derivation of the cross-spectral densities is also explained in more detail.

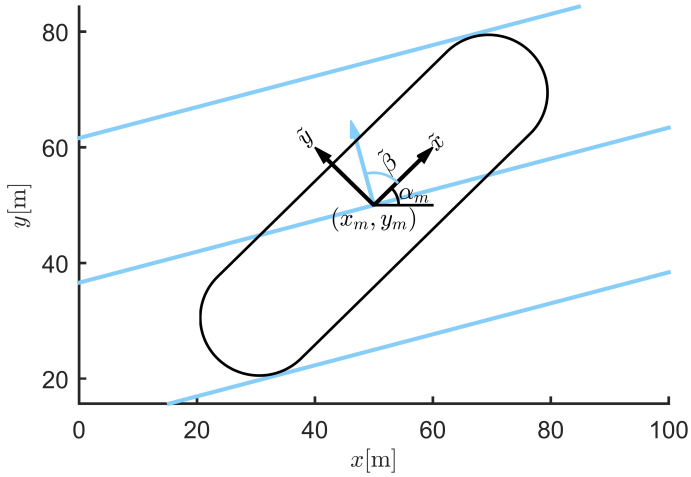

Figure 5.2: The local coordinate system of a pontoon.

5.2.3 Equations of motion

By employing the framework of the finite element method (FEM), the equations of motion describing the linear behaviour of a floating bridge can be written as

$$\boldsymbol{M}_s\ddot{\boldsymbol{u}}(t) + \boldsymbol{C}_s\dot{\boldsymbol{u}}(t) + \boldsymbol{K}_s\boldsymbol{u}(t) = \boldsymbol{q}_h(t),$$

where $\boldsymbol{M}_s$, $\boldsymbol{C}_s$ and $\boldsymbol{K}_s$ are the *structural* system matrices, excluding all fluid-structure interaction contributions; $\boldsymbol{u}(t)$ is the displacement vector; $\boldsymbol{q}_h(t)$ is the total hydrodynamic action, including both wave excitation and fluid-structure interaction contributions; t is the time variable; and $\dot{\boldsymbol{u}} \equiv \frac{\partial \boldsymbol{u}}{\partial t}$. The total hydrodynamic action may be decomposed as follows:

$$\boldsymbol{q}_h(t) = -\left(\int_{-\infty}^{\infty} \boldsymbol{M}_h(t-\tau)\ddot{\boldsymbol{u}}(t)d\tau + \int_{-\infty}^{\infty} \boldsymbol{C}_h(t-\tau)\dot{\boldsymbol{u}}(t)d\tau + \boldsymbol{K}_h\boldsymbol{u}(t)\right) + \boldsymbol{q}(t).$$

Here the first term represents the fluid-structure interaction, with $\boldsymbol{M}_h(t)$ and $\boldsymbol{C}_h(t)$ being the time-domain representations of added mass and added damping respectively, and $\boldsymbol{K}_h$ being the hydrostatic stiffness. The second term, $\boldsymbol{q}(t)$, is the wave excitation load. Convolution integrals in the time domain are equivalent to multiplication in the frequency domain, such that the total hydrodynamic action may be written as follows by enforcing frequency

domain notation:

$$\hat{\boldsymbol{q}}_h(\omega) = -\left(-\omega^2 \hat{\boldsymbol{M}}_h(\omega) + i\omega \hat{\boldsymbol{C}}_h(\omega) + \boldsymbol{K}_h\right) \hat{\boldsymbol{u}}(\omega) + \hat{\boldsymbol{q}}(\omega).$$

Here hats denote the frequency domain counterparts of the different quantities. Finally, the equation of motion of the system may be written on the following compact form, in the frequency domain:

$$\left(-\omega^2 \boldsymbol{M}(\omega) + i\omega \boldsymbol{C}(\omega) + \boldsymbol{K}\right) \hat{\boldsymbol{u}}(\omega) = \hat{\boldsymbol{q}}(\omega)$$

where $\boldsymbol{M}(\omega) = \boldsymbol{M}_s + \hat{\boldsymbol{M}}_h(\omega)$, $\boldsymbol{C}(\omega) = \boldsymbol{C}_s + \hat{\boldsymbol{C}}_h(\omega)$ and $\boldsymbol{K} = \boldsymbol{K}_s + \boldsymbol{K}_h$.

The second-order probabilistic properties of zero-mean response and wave excitation processes are fully described by cross-spectral densities. The stochastic frequency domain problem is easily solved by applying the power spectral density method. The cross-spectral density matrix of the response is then calculated as

$$\boldsymbol{S}_{\boldsymbol{u}}(\omega) = \boldsymbol{H}(\omega) \boldsymbol{S}_{\boldsymbol{q}}(\omega) \boldsymbol{H}(\omega)^H, \tag{5.2}$$

where $\boldsymbol{H}(\omega) = \left(-\omega^2 \boldsymbol{M}(\omega) + i\omega \boldsymbol{C}(\omega) + \boldsymbol{K}\right)^{-1}$ and $[\cdot]^H$ denotes the conjugate transpose. The cross-spectral density matrix $\boldsymbol{S}_{\boldsymbol{q}}(\omega)$ of the wave excitation load is found as explained in Section 5.2.2. More details on the subject may be found in e.g. [42, 45, 60, 62, 71].

5.3 Short-term response model for the case study bridge

The case study bridge consists of an S-shaped continuous girder box, which is supported on 20 pontoons. Figure 5.3 depicts the most important geometrical properties of the bridge. 16 symmetrically positioned cables provide side-support by fixation to the sea bed, cf. Fig. 5.4. The cross section of the girder is illustrated in Fig. 5.5. It is highlighted that the modelled bridge is considered merely as a useful example for the application of the methodology, and does not necessarily represent a feasible design.

5.3.1 Numerical response model set-up

The study carried out is performed using the approach presented in [42], and the reader is referred to that paper for a detailed description of the

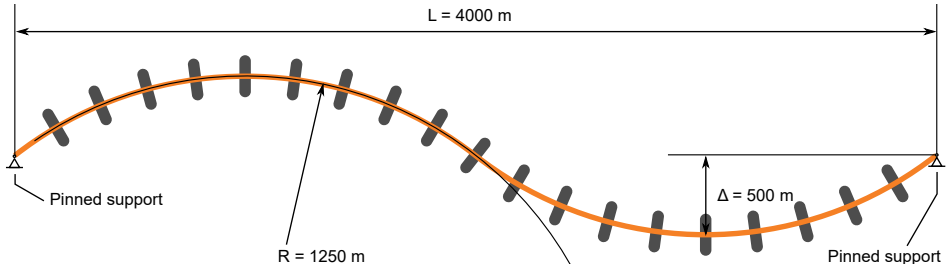

(a) Top view of main geometry.

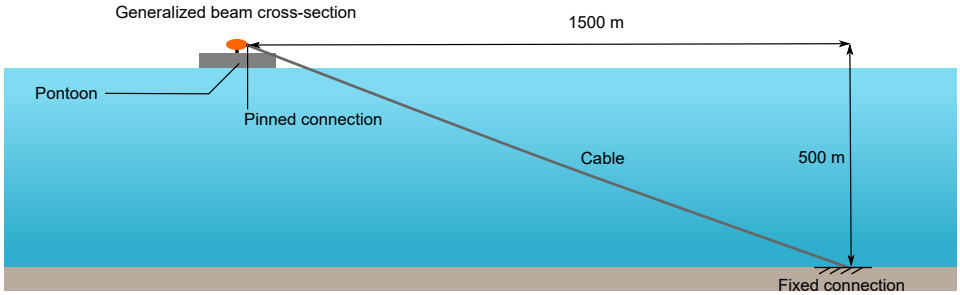

(b) Cable geometry.

Figure 5.3: Geometry of the bridge model.

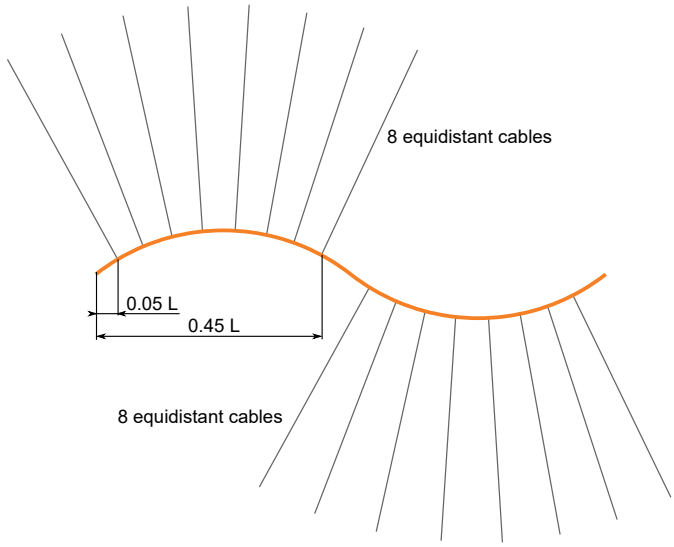

Figure 5.4: Position of cables. L refers to the horizontal distance, as defined in Fig. 5.3.

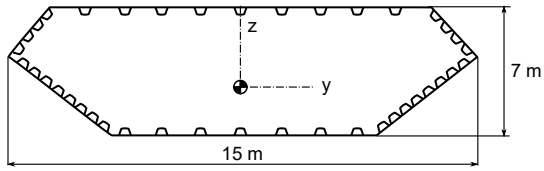

Figure 5.5: Main dimensions of cross section.

methodology for the numerical model set-up. The most important details are repeated here, for the convenience of the reader.

Two different sub-structures are used to create the full bridge model:

(I) A structural sub-structure, based on an Abaqus model incorporating all structural components and also including pontoon inertia and buoyancy.

(II) A hydrodynamic sub-structure, based on a WADAM model providing fluid-structure interaction terms, but excluding the buoyancy and pontoon inertia which are both included in (I).

To combine the two sub-structures, a modal decomposition is carried out in Abaqus [12]. The resulting mode shapes are referred to as the *dry* mode shapes, and are used as a new coordinate basis. The mode shapes are defined by the DOFs characterizing the rigid body motion of all pontoons. The frequency-dependent mass and damping contributions originating from the hydrodynamic model (II) are transformed to the coordinate basis defined by the dry mode shapes, before they are added to the modal system matrices from the structural model (I). It is noted that the results from the single pontoon analysis is duplicated and used for all pontoons, but necessary transformations and matrix book keeping are applied such that the orientation and additions are correct. The wave excitation cross-spectral density matrix $\boldsymbol{S_q}(\omega)$, given by Eqn. (5.1), is transformed to the coordinate basis given by the dry mode shapes, before the power spectral density method, cf. Eqn (5.2), is applied to calculate the spectral density of the response. In the final step, the response spectral density is transformed back to the physical DOFs of the pontoons. The main reason for carrying out this basis transformation is to avoid the extraction of all the free DOFs of the finite element model, as static condensation is not appropriate for dynamic prob-

Table 5.1: Parameters used for the generalized cross section.

Parameter	Value	Description
A	1.026 m^2	Cross-sectional area
I_y	10.79 m^4	Second moment of area about axis y
I_z	29.34 m^4	Second moment of area about axis z
J	24.92 m^4	Polar moment of area
z_c	3736 mm	Distance from bottom to neutral axis
y_c	0 mm	Distance from center to neutral axis

lems. It should be noted that although a reduced order model is obtained, this is not a mode by mode approach because the modes will be coupled due to the hydrodynamic contributions.

5.3.2 Structural model

The continuous girder box is modelled in Abaqus with beam elements, with a generalized cross section characterized by the parameters shown in Tab. 5.1. The cables are modelled as beam elements, with circular cross sections.

In an initial static step, pre-tensioning of cables, cable bouyancy, global gravity, and static uplift forces are applied to the structure. The cables are pre-tensioned by assuming a constant negative temperature, which corresponds to a pre-tension of approximately 5000 kN. Fluid inertial effects are included for the cables; however, no drag damping is considered.

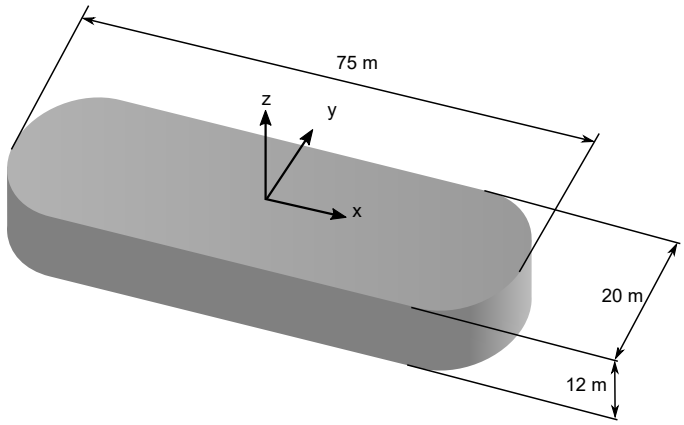

Figure 5.6: Main dimensions of pontoon and local coordinate system.

5.3.3 Hydrodynamic pontoon model

A single hydrodynamic analysis, carried out in WADAM, is used to establish all system matrix contributions from the fluid-structure interaction. The geometry of the pontoon is depicted in Fig. 5.6. In the model set-up, buoyancy and inertia of the pontoon itself were added as local contributions to the bridge at the locations of the pontoons. The added hydrodynamic mass and damping coefficients, referring to the local coordinate system of the pontoon, are plotted in Figs. 5.7 and 5.8.

5.3.4 Modal parameters and shapes

Due to the frequency dependency of the hydrodynamic contributions, the eigenvalue problem is solved by iteration, as described in [42]. The resulting 10 first undamped natural frequencies and critical damping ratios are shown in Tab. 5.2, and the real part of the corresponding mode shapes are depicted in Fig. 5.9. Figure 5.9 reveals that the first 10 modes all have lateral motion patterns. From frequencies above the natural frequency of mode 10 and up, numerous cable modes are present.

Table 5.2: Modal parameters from the numerical eigenvalue solution, corresponding to mode shapes illustrated in Fig. 5.9. The undamped natural frequency is denoted ω_n, and ξ is the corresponding critical damping ratio.

Mode number	ω_n [rad/s]	ξ [%]
Mode 1 (Fig. 5.9a)	0.11	1.53
Mode 2 (Fig. 5.9b)	0.15	1.28
Mode 3 (Fig. 5.9c)	0.16	1.18
Mode 4 (Fig. 5.9d)	0.18	1.02
Mode 5 (Fig. 5.9e)	0.20	0.88
Mode 6 (Fig. 5.9f)	0.24	0.79
Mode 7 (Fig. 5.9g)	0.28	0.75
Mode 8 (Fig. 5.9h)	0.33	0.81
Mode 9 (Fig. 5.9i)	0.38	1.06
Mode 10 (Fig. 5.9j)	0.45	1.87

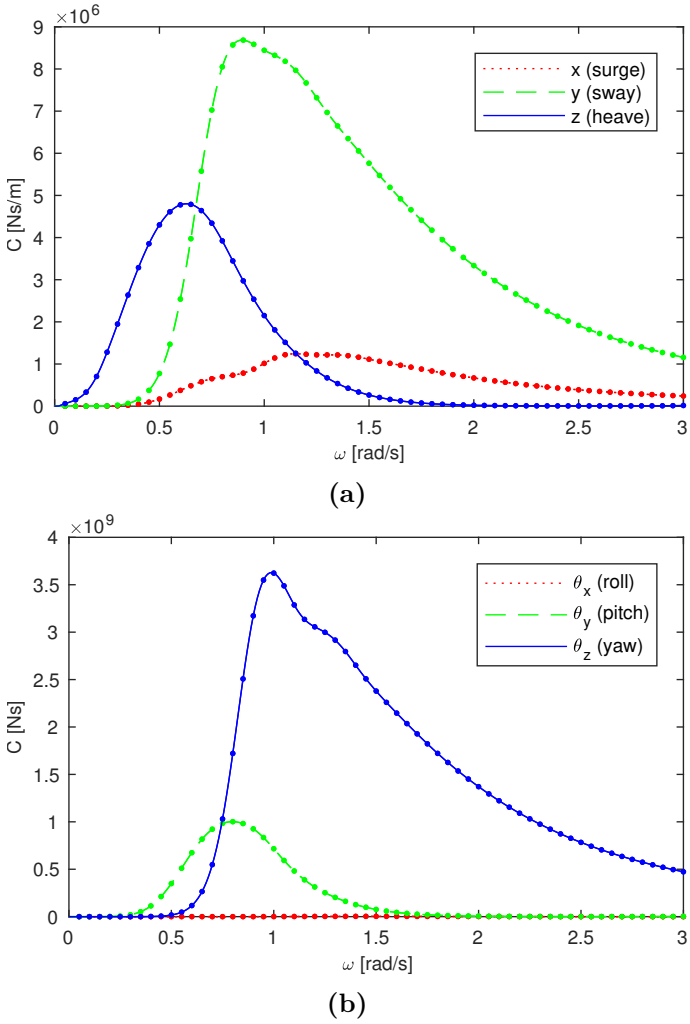

Figure 5.7: Translational (a) and rotational (b) damping coefficients of a single pontoon. Dots indicate the original data from WADAM, whilst lines represent interpolated data. The coordinates refer to the local coordinate system of the pontoon, as shown in Fig. 5.6.

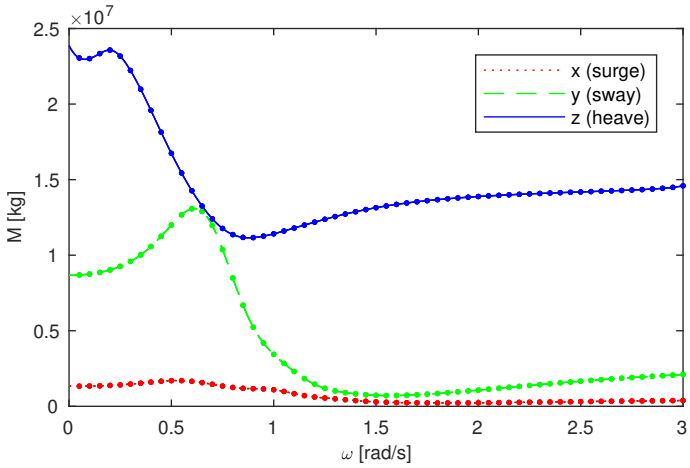

(a)

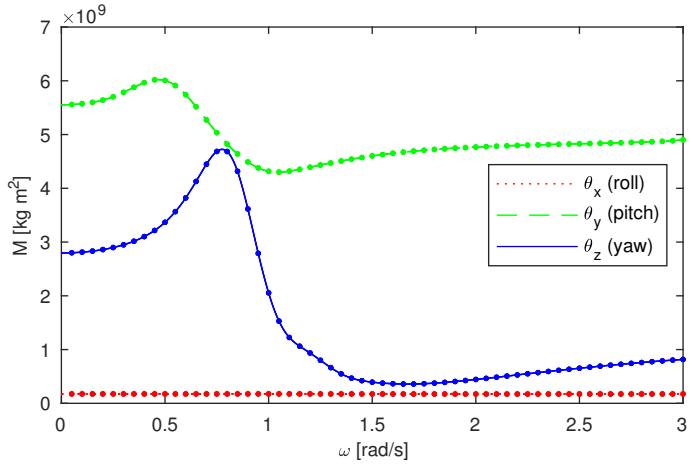

(b)

Figure 5.8: Translational (a) and rotational (b) mass coefficients of a single pontoon. Dots indicate the original data from WADAM, whilst lines represent interpolated data. The coordinates refer to the local coordinate system of the pontoon, as shown in Fig. 5.6.

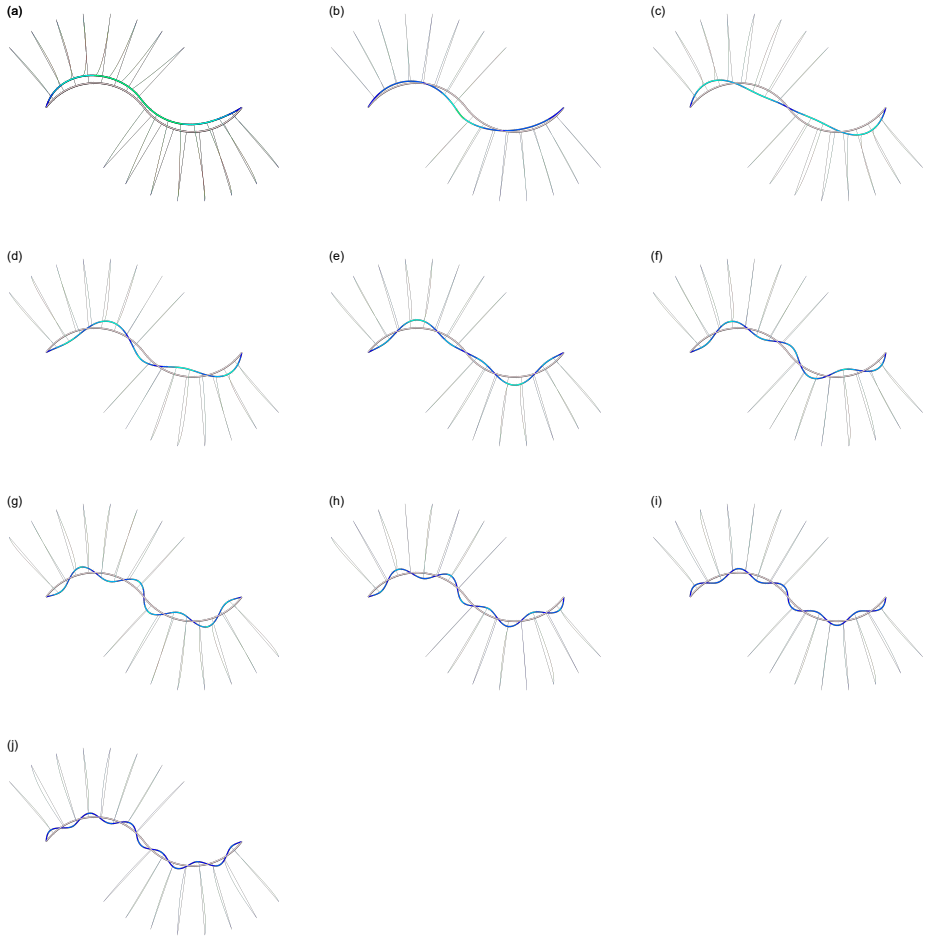

Figure 5.9: Mode shapes from numerical eigenvalue solution, corresponding to natural frequencies and damping ratios presented in Tab. 5.2. Note that the eigenvectors are complex, and their mode shape representation is therefore a snapshot. (a) Mode 1; (b) mode 2; (c) mode 3; (d) mode 4; (e) mode 5; (f) mode 6; (g) mode 7; (h) mode 8; (i) mode 9; (j) mode 10.

5.4 Long-term extreme response

For the modelling of long-term extreme response of marine structures, the long-term situation can be considered as a collection of $\tilde{N}$ short-term states, each of duration $\tilde{T}$. During each short-term state the environmental processes are assumed stationary and defined by a set of n environmental parameters $\boldsymbol{W} = [W_1, W_2, \ldots, W_n]$. In this paper, we only consider the sea elevation, which is defined in terms of the environmental parameters $\boldsymbol{W} = [H_s, T_z, \bar{\Theta}]$, cf. Section 5.2.1. We will assume that the joint probability density function (PDF) of the environmental parameters, denoted $f_{\boldsymbol{W}}(\boldsymbol{w})$, is given. This PDF can be estimated by fitting a probabilistic model to a scatter diagram of recorded sea states [60].

The methodology presented in this paper for the calculation of extreme response is illustrated for a single response process. Specifically, we consider the horizontal transverse displacement of pontoon number five from the left in Fig. 5.3. This is the displacement along the local $\tilde{x}$-axis of this pontoon (see Fig. 5.2), and will henceforth simply be referred to as the response process, denoted $R(t)$. Being the response of a linear and time-invariant dynamical system, $R(t)$ will be a stationary Gaussian process with zero mean because the load process is. Hence, the response $R(t)$ is fully characterized by its spectral density $S_R(\omega)$, which is obtained as a diagonal element of the cross-spectral density matrix $\boldsymbol{S_u}(\omega)$ given by Eqn. (5.2). Figure 5.10 shows an example of the response spectrum $S_R(\omega)$ for a short-term situation where the environmental variables are given by $\boldsymbol{W} = [H_s, T_z, \bar{\Theta}] = [1\text{ m}, 6\text{ s}, -\pi/2]$.

5.4.1 Short-term extreme value distribution

The maximal value of the response process $R(t)$ during a short-term period with given environmental variables $\boldsymbol{W}$ will be a random variable. This short-term extreme response is denoted by $\tilde{R}|\boldsymbol{W}$ and its cumulative distribution function (CDF) is $F_{\tilde{R}|\boldsymbol{W}}(r|\boldsymbol{w}) = \text{Prob}[\tilde{R} \leq r|\boldsymbol{W} = \boldsymbol{w}] = \text{Prob}[\tilde{R} \leq r|H_s = h_s, T_z = t_z, \bar{\Theta} = \bar{\theta}]$. As explained in detail in [60], the short-term extreme value distribution $F_{\tilde{R}|\boldsymbol{W}}(r|\boldsymbol{w})$ can be found by assuming independent upcrossings of high levels r as

$$F_{\tilde{R}|\boldsymbol{W}}(r|\boldsymbol{w}) = \exp\left\{-\frac{\tilde{T}}{2\pi}\sqrt{\frac{m_2(\boldsymbol{w})}{m_0(\boldsymbol{w})}}\exp\left\{-\frac{r^2}{2m_0(\boldsymbol{w})}\right\}\right\}, \qquad (5.3)$$

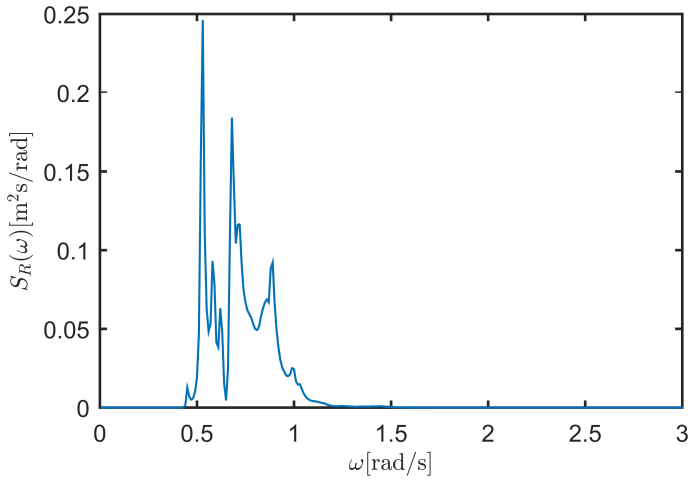

Figure 5.10: The response spectrum $S_R(\omega)$ when $\boldsymbol{W} = [H_s, T_z, \bar{\Theta}] = [1\text{ m}, 6\text{ s}, -\pi/2]$.

which holds for reasonably large values of r. Here the i-th moment $m_i(\boldsymbol{w})$ of the response spectrum $S_R(\omega)$ is defined as

$$m_i(\boldsymbol{w}) = \int_0^\infty \omega^i S_R(\omega) d\omega.$$

Note that $S_R(\omega)$ is dependent on the environmental parameters $\boldsymbol{w}$, though not written explicitly.

It should be noted that although Eqn. (5.1) and thereby Eqn. (5.3) are based on the assumption of homogeneity, which may be questioned for floating bridge applications, the general method presented in this paper is readily used along with other ways of calculating the short-term CDF $F_{\tilde{R}|\boldsymbol{W}}(r|\boldsymbol{w})$. The only required assumption is that the response process can be approximated as stationary for some short-term period $\tilde{T}$.

5.4.2 Long-term extreme response models

The long-term CDF of the short-term extreme value is denoted $F_{\tilde{R}}(r)$, and gives the distribution of the largest response value $\tilde{R}$ during an arbitrarily chosen short-term condition. This can be obtained as an average of all short-term CDFs $F_{\tilde{R}|\boldsymbol{W}}(r|\boldsymbol{w})$ weighted by the distribution $f_{\boldsymbol{W}}(\boldsymbol{w})$ of the environmental parameters. In order to estimate $f_{\boldsymbol{W}}(\boldsymbol{w})$ in the first place,

an ergodicity assumption is required for the environmental parameters [59], and hence $F_{\tilde{R}}(r)$ should be expressed as an ergodic average [59, 60]. This yields the long-term extreme response formulation

$$F_{\tilde{R}}(r) = \exp\left\{\int_{\boldsymbol{w}} \left(\ln F_{\tilde{R}|\boldsymbol{W}}(r|\boldsymbol{w})\right) f_{\boldsymbol{W}}(\boldsymbol{w})\, d\boldsymbol{w}\right\}. \tag{5.4}$$

A very common approximate formulation, is given by the population mean

$$F_{\tilde{R}}(r) \approx \int_{\boldsymbol{w}} F_{\tilde{R}|\boldsymbol{W}}(r|\boldsymbol{w}) f_{\boldsymbol{W}}(\boldsymbol{w})\, d\boldsymbol{w}. \tag{5.5}$$

The formulations Eqns. (5.4) and (5.5) are discussed in more detail in [21, 68].

The long-term CDF $F_{\tilde{R}}(r)$ can be evaluated by solving the integrals in Eqns. (5.4) and (5.5) numerically. Unfortunately, full numerical integration requires a very large amount of short-term response calculations, since the short-term CDF $F_{\tilde{R}|\boldsymbol{W}}(r|\boldsymbol{w})$ must be calculated for a very large number of environmental conditions. This motivates the use of inverse reliability methods for calculation of long-term extreme response.

5.4.3 Writing the long-term CDF in terms of a reliability problem

In order to use reliability methods for evaluating the long-term CDF $F_{\tilde{R}}(r)$, it must be rewritten in terms of a reliability problem. A reliability problem in the general sense [53] is an integral of the form

$$\int_{G(\boldsymbol{v})\leq 0} f_{\boldsymbol{V}}(\boldsymbol{v}) d\boldsymbol{v},$$

where $\boldsymbol{V}$ is a random vector with joint PDF $f_{\boldsymbol{V}}(\boldsymbol{v})$ and $G(\boldsymbol{v})$ is a function referred to as the limit state function.

For the approximate formulation Eqn. (5.5), it is well known that the long-term CDF can be expressed in terms of a reliability problem by rewriting

$$\int_{\boldsymbol{w}} F_{\tilde{R}|\boldsymbol{W}}(r|\boldsymbol{w})\, f_{\boldsymbol{W}}(\boldsymbol{w})\, d\boldsymbol{w} = \int_{\boldsymbol{w}} \int_{\tilde{r}\leq r} f_{\tilde{R}|\boldsymbol{W}}(\tilde{r}|\boldsymbol{w})\, d\tilde{r} f_{\boldsymbol{W}}(\boldsymbol{w})\, d\boldsymbol{w}.$$

Introducing the random vector $\bar{\boldsymbol{V}} = [\boldsymbol{W}, \tilde{R}]$, whose joint PDF is given by $f_{\bar{\boldsymbol{V}}}(\bar{\boldsymbol{v}}) = f_{\tilde{R}|\boldsymbol{W}}(\tilde{r}|\boldsymbol{w})\, f_{\boldsymbol{W}}(\boldsymbol{w})$, Eqn. (5.5) yields

$$F_{\tilde{R}}(r) \approx \int_{\tilde{r} \leq r} f_{\bar{\boldsymbol{V}}}(\bar{\boldsymbol{v}})\, d\bar{\boldsymbol{v}} = 1 - \int_{r \leq \tilde{r}} f_{\bar{\boldsymbol{V}}}(\bar{\boldsymbol{v}})\, d\bar{\boldsymbol{v}}.$$

Finally, we obtain

$$F_{\tilde{R}}(r) \approx 1 - \int_{G_r(\bar{\boldsymbol{v}}) \leq 0} f_{\bar{\boldsymbol{V}}}(\bar{\boldsymbol{v}})\, d\bar{\boldsymbol{v}}, \tag{5.6}$$

where $G_r(\bar{\boldsymbol{v}}) = r - \tilde{r} = r - \bar{v}_{n+1}$, with $\bar{v}_{n+1}$ being the $(n+1)$-th component of the vector $\bar{\boldsymbol{v}}$.

The exact formulation Eqn. (5.4) can be used directly to obtain a better approximation for the long-term CDF in terms of a reliability problem [21, 23, 24]. Equation (5.4) is rewritten by multiplying and dividing the integral by some freely chosen constant $C \geq 1$. Then unity is added and subtracted, keeping in mind that $\int_{\boldsymbol{w}} f_{\boldsymbol{W}}(\boldsymbol{w})\, d\boldsymbol{w} = 1$. Specifically, we obtain

$$F_{\tilde{R}}(r) = \exp\left\{-C\left(1 - \int_{\boldsymbol{w}} \left(1 + \frac{1}{C} \ln F_{\tilde{R}|\boldsymbol{W}}(r|\boldsymbol{w})\right) f_{\boldsymbol{W}}(\boldsymbol{w})\, d\boldsymbol{w}\right)\right\}.$$

Introducing the random variable Y defined by the CDF $F_{Y|\boldsymbol{W}}(y|\boldsymbol{w}) = \max\left\{1 + \frac{1}{C} \ln F_{\tilde{R}|\boldsymbol{W}}(y|\boldsymbol{w}), 0\right\}$, the factor $1 + \frac{1}{C} \ln F_{\tilde{R}|\boldsymbol{W}}(r|\boldsymbol{w})$ in the above integral can be replaced by $F_{Y|\boldsymbol{W}}(r|\boldsymbol{w})$. This yields the approximation

$$F_{\tilde{R}}(r) \approx \exp\left\{-C\left(1 - \int_{\boldsymbol{w}} F_{Y|\boldsymbol{W}}(r|\boldsymbol{w})\, f_{\boldsymbol{W}}(\boldsymbol{w})\, d\boldsymbol{w}\right)\right\}. \tag{5.7}$$

Here the domain where $1 + \frac{1}{C} \ln F_{\tilde{R}|\boldsymbol{W}}(r|\boldsymbol{w}) < 0$ is disregarded. This is a very good approximation for large values of r, since $F_{\tilde{R}|\boldsymbol{W}}(r|\boldsymbol{w})$ will be close to unity. Furthermore, by increasing the value of C, the approximation will improve. Now the approximation Eqn. (5.7) obtained directly from the exact formulation Eqn. (5.4) can be written in terms of a reliability problem using the same approach as for the approximate formulation. Finally, the long-term CDF is expressed as

$$F_{\tilde{R}}(r) \approx \exp\left\{-C \int_{G_r(\boldsymbol{v}) \leq 0} f_{\boldsymbol{V}}(\boldsymbol{v})\, d\boldsymbol{v}\right\}, \tag{5.8}$$

where $\boldsymbol{V} = [\boldsymbol{W}, Y]$ and $G_r(\boldsymbol{v}) = r - y = r - v_{n+1}$.

5.4.4 Calculation of extreme response using inverse reliability methods

When long-term extreme responses are calculated for design purposes, we usually seek the characteristic response value r_q which has a specified annual exceedance probability q. This may also be referred to as the response value with a return period of $1/q$ years, or simply the $1/q$-year response. The characteristic response r_q is found by requiring

$$1 - F_{\tilde{R}}(r_q) = \frac{q}{\tilde{N}},$$

where $\tilde{N} = 1 \text{ yr}/\tilde{T}$ is the number of short-term periods in one year. In this paper we have used $\tilde{T} = 3$ h, which gives $\tilde{N} = 365 \cdot 8 = 2920$. If we denote by $\tilde{r}_q$ the long-term extreme response obtained when using the approximate formulation Eqn. (5.5) for the long-term CDF, we have from Eqn. (5.6) that $\tilde{r}_q$ must satisfy

$$\int_{G_{\tilde{r}_q}(\bar{\boldsymbol{v}}) \leq 0} f_{\bar{\boldsymbol{V}}}(\bar{\boldsymbol{v}})\, d\bar{\boldsymbol{v}} = \frac{q}{\tilde{N}}. \tag{5.9}$$

Similarly, using Eqn. (5.8), which corresponds to the exact formulation Eqn. (5.4), yields the following equation for r_q:

$$\int_{G_{r_q}(\boldsymbol{v}) \leq 0} f_{\boldsymbol{V}}(\boldsymbol{v})\, d\boldsymbol{v} = -\frac{1}{C} \ln\left(1 - \frac{q}{\tilde{N}}\right). \tag{5.10}$$

Now the problem of finding $\tilde{r}_q$ and r_q that satisfies Eqns. (5.9) and (5.10) can be solved in an approximate manner using inverse reliability methods. Taking Eqn. (5.9) as an example, the random vector $\bar{\boldsymbol{V}}$ is transformed into a vector $\boldsymbol{U}$ of independent standard normal random variables by the Rosenblatt transformation $\boldsymbol{U} = T(\bar{\boldsymbol{V}})$, and Eqn. (5.9) becomes

$$\int_{g_{\tilde{r}_q}(\boldsymbol{u}) \leq 0} f_{\boldsymbol{U}}(\boldsymbol{u})\, d\boldsymbol{u} = \frac{q}{\tilde{N}}, \tag{5.11}$$

where $g_{\tilde{r}_q}(\boldsymbol{u}) = G_{\tilde{r}_q}(T^{-1}(\boldsymbol{u})) = \tilde{r}_q - \tilde{r}(\boldsymbol{u})$ is the transformed limit state function and $f_{\boldsymbol{U}}(\boldsymbol{u})$ is the multivariate standard normal PDF. Using the first-order reliability method (FORM) to approximate the integral in Eqn. (5.11), the inverse FORM (IFORM) problem can be derived as

$$\tilde{r}_q^{\text{F}} = \max \tilde{r}(\boldsymbol{u}); \text{ subject to } |\boldsymbol{u}| = \beta, \tag{5.12}$$

where $\beta = -\Phi^{-1}(q/\tilde{N})$ with $\Phi(\cdot)$ being the standard normal CDF. Thus, solving the IFORM problem Eqn. (5.12) provides an estimate $\tilde{r}_q^{\mathrm{F}}$ for the characteristic extreme response value $\tilde{r}_q$. In this work we have used the solution algorithm proposed in [21]. For details on the transformation to standard normal variables and the derivation of the IFORM problem the reader is referred to [21, 53, 79].

If, on the other hand, the second-order reliability method (SORM) is used to approximate the integral in Eqn. (5.11), an inverse SORM (ISORM) method can be derived. In [23] an ISORM approach is proposed where the IFORM problem Eqn. (5.12) is solved repeatedly, updating the value of β which is unknown in this case. The characteristic extreme response estimate provided by the ISORM method is denoted $\tilde{r}_q^{\mathrm{S}}$.

The inverse reliability methods IFORM and ISORM can be applied to Eqn. (5.10) using the same approach as described above, providing long-term extreme response estimates that approximate r_q. We denote these estimates by r_q^{F} and r_q^{S} respectively. The only differences will be that $\boldsymbol{V}$ is transformed instead of $\bar{\boldsymbol{V}}$, and that $\beta = -\Phi^{-1}\left(-\frac{1}{C}\ln\left(1-\frac{q}{\tilde{N}}\right)\right)$.

It is reported in [21, 23] that the use of reliability methods appears to give good accuracy for the calculated long-term extreme response while keeping the number of required short-term response calculations within reasonable levels.

5.4.5 Environmental contour method

Even though IFORM and ISORM represent efficient methods for extreme response evaluation, some cases may still call for a more simplified approach. The environmental contour method has been proposed as such a simplified approach for estimating characteristic long-term extreme response values [29]. It is developed in [79] based on the approximate formulation Eqn. (5.5) and the IFORM approximation. In fact, the method can be considered as a special case of the IFORM problem Eqn. (5.12) where the short-term extreme response is regarded as deterministic [79].

The environmental contour corresponding to a given annual exceedance probability q is found from the joint environmental PDF $f_{\boldsymbol{W}}(\boldsymbol{w})$ without any consideration of the structural response. Then, the most unfavourable combination of environmental parameters along this q-probability contour,

referred to as the design point, is identified. In this paper the design point, denoted by $\hat{\boldsymbol{w}}$, is taken as the point along the contour where the median, i.e. the 0.5-fractile, of the short-term distribution $F_{\tilde{R}|\boldsymbol{W}}(r|\boldsymbol{w})$ attains its maximal value. This maximization problem is the same as the IFORM problem Eqn. (5.12), but since the extreme response is regarded deterministic the dimension is reduced by one. Nevertheless, the same solution algorithm can be applied to obtain the design point $\hat{\boldsymbol{w}}$. In order to account for the randomness of the short-term extreme value, the characteristic response value is chosen as the p-fractile, $p > 0.5$, of the short-term extreme value distribution $F_{\tilde{R}|\boldsymbol{W}}(r|\hat{\boldsymbol{w}})$ at the design point. The appropriate value for p must be validated by a full long-term analysis [60].

It is worth mentioning that it is possible to derive an environmental contour method based on the IFORM solution of the exact formulation Eqn. (5.4). In that case, we would use the short-term distribution $F_{Y|\boldsymbol{W}}(y|\boldsymbol{w})$ instead of $F_{\tilde{R}|\boldsymbol{W}}(r|\boldsymbol{w})$, and the q-probability contour would be defined in the standard normal space by a radius $\beta = -\Phi^{-1}\left(-\frac{1}{C}\ln\left(1-\frac{q}{\tilde{N}}\right)\right)$ instead of $\beta = -\Phi^{-1}(q/\tilde{N})$. This would, however, introduce contours dependent on the parameter C, and the appealing simplicity of the contour method would be undermined.

5.5 Numerical results

5.5.1 Environmental models

The environmental parameters defining the short-term wave situation according to Section 5.2.1 are the significant wave height H_s, the zero-crossing period T_z and the mean wave direction $\bar{\Theta}$. Using the conditional modelling approach described in [8, 14], the CDF of the significant wave height H_s is given by a 2-parameter Weibull distribution

$$F_{H_s}(h) = 1 - \exp\left\{-\left(\frac{h}{\alpha}\right)^{\beta}\right\}, \tag{5.13}$$

and the zero-crossing period T_z has a conditional lognormal distribution

$$F_{T_z|H_s}(t|h) = \Phi\left(\frac{\ln t - \mu(h)}{\sigma(h)}\right), \tag{5.14}$$

where $\mu(h) = a_0 + a_1 h^{a_2}$ and $\sigma(h) = b_0 + b_1 e^{b_2 h}$. Here α, β and $a_0, a_1, a_2, b_0, b_1, b_2$ are the parameters of the distributions. For the mean wave direction

$\bar{\Theta}$, we use a distribution independent of H_s and T_z, given by the CDF

$$F_{\bar{\Theta}}(\theta) = \begin{cases} 0, & \text{for } \theta < -\pi, \\ 2\left(1+\frac{\theta}{\pi}\right)^2, & \text{for } -\pi \leq \theta < -\frac{\pi}{2}, \\ 1-2\left(\frac{\theta}{\pi}\right)^2, & \text{for } -\frac{\pi}{2} \leq \theta < 0, \\ 1, & \text{for } \theta \geq 0. \end{cases} \tag{5.15}$$

This means that the PDF $f_{\bar{\Theta}}(\theta)$, obtained by differentiating Eqn. (5.15) with respect to θ, is piecewise linear between $-\pi$ and 0 with a peak at $-\frac{\pi}{2}$. Similarly, the PDFs $f_{H_s}(h)$ and $f_{T_z|H_s}(t|h)$ can be obtained by differentiating Eqns. (5.13) and (5.14) with respect to h and t respectively, and the joint PDF of the environmental parameters is given as

$$f_{\boldsymbol{W}}(\boldsymbol{w}) = f_{H_s,T_z,\bar{\Theta}}(h,t,\theta) = f_{H_s}(h)\, f_{T_z|H_s}(t|h)\, f_{\bar{\Theta}}(\theta). \tag{5.16}$$

The environmental model Eqn. (5.16) where all three environmental parameters are random variables will be referred to as EM1. Different environmental models can be obtained by considering some of the environmental parameters as deterministic. If for instance the zero-crossing period is taken as the conditional median obtained from the CDF Eqn. (5.14), i.e. $T_z = \exp\{\mu(H_s)\}$, we obtain the environmental model

$$f_{\boldsymbol{W}}(\boldsymbol{w}) = f_{H_s,\bar{\Theta}}(h,\theta) = f_{H_s}(h)\, f_{\bar{\Theta}}(\theta). \tag{5.17}$$

This will be referred to as EM2. We also consider an environmental model where the mean wave direction is given as $\bar{\Theta} = -\pi/2$. This yields

$$f_{\boldsymbol{W}}(\boldsymbol{w}) = f_{H_s,T_z}(h,t) = f_{H_s}(h)\, f_{T_z|H_s}(t|h)\,, \tag{5.18}$$

which will be referred to as EM3. The environmental models EM1, EM2 and EM3 will all have the same values for the distribution parameters. We also consider a model EM4, which is given by Eqn. (5.18) with different parameter values. An overview of the environmental models and their distribution parameters is provided in Tab. 5.3.

The environmental models are illustrated in Fig. 5.11 by displaying the environmental contours corresponding to annual exceedance probabilities $q = 10^{-2}$ and $q = 10^{-4}$, i.e. the 100-year and 10 000-year contours. For the two-dimensional models EM2, EM3 and EM4, the isoprobability contours

Table 5.3: Overview of the considered environmental models.

		H_s			T_z							$\bar{\Theta}$
Name	Joint PDF	Value/CDF	α	β	Value/CDF	a_0	a_1	a_2	b_0	b_1	b_2	Value/CDF
EM1	Eqn. (5.16)	Eqn. (5.13)	0.587	1.59	Eqn. (5.14)	0.151	0.339	0.167	0.07	0.3449	−0.6219	Eqn. (5.15)
EM2	Eqn. (5.17)	Eqn. (5.13)	"	"	$\exp\{\mu(H_s)\}$	"	"	"	n/a	n/a	n/a	Eqn. (5.15)
EM3	Eqn. (5.18)	Eqn. (5.13)	"	"	Eqn. (5.14)	"	"	"	0.07	0.3449	−0.6219	$-\pi/2$
EM4	Eqn. (5.18)	Eqn. (5.13)	0.550	1.53	Eqn. (5.14)	−0.120	1.439	0.150	0.07	0.0978	−0.0382	$-\pi/2$

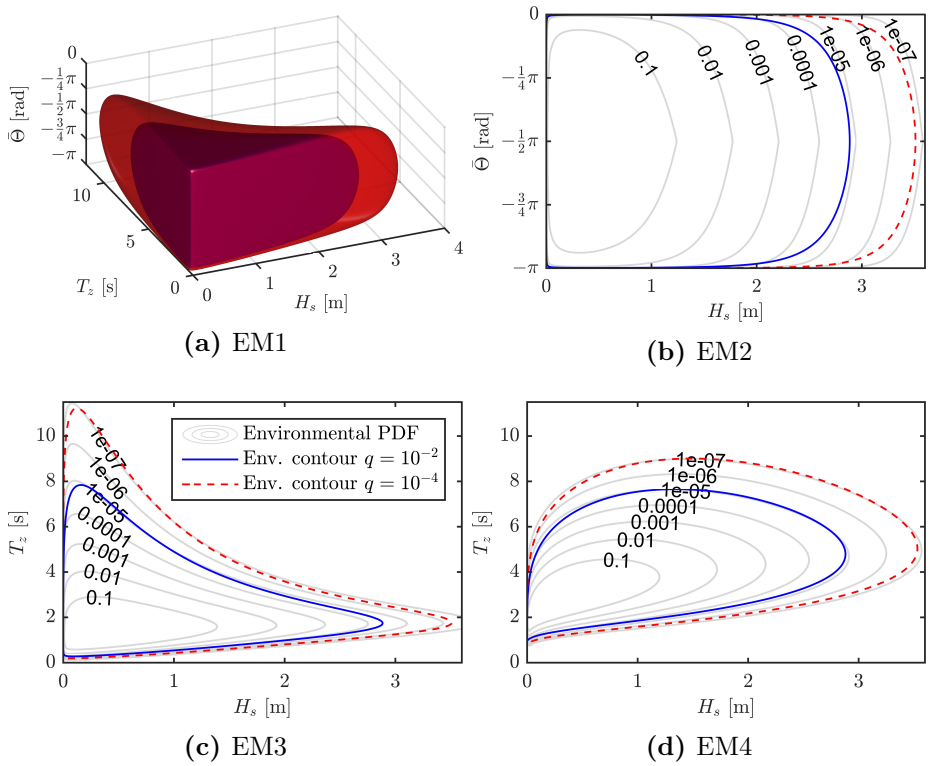

(a) EM1 **(b)** EM2

(c) EM3 **(d)** EM4

Figure 5.11: The contours corresponding to annual exceedance probabilities $q = 10^{-2}$ and $q = 10^{-4}$ for the different environmental models. For the two-dimensional models EM2, EM3 and EM4 the PDFs are illustrated by displaying the isoprobability contours. EM2 and EM3 are obtained from EM1 by regarding as deterministic T_z and $\bar{\Theta}$ respectively.

obtained from the PDFs Eqns. (5.17) and (5.18) are also shown. Note that EM2 and EM3 are obtained from EM1 by regarding as deterministic T_z and $\bar{\Theta}$ respectively. EM4 represent a different model entirely. However, for all the models considered, the significant wave heights H_s with return periods of 100 and 10 000 years are approximately 2.9 m and 3.5 m respectively.

5.5.2 Characteristic extreme response values

5.5.2.1 Inverse reliability methods

Estimates for the characteristic response value r_q were calculated using the methods described in Section 5.4.4. The value $\tilde{r}_q$ was obtained by numerically solving the integral in the approximate formulation Eqn. (5.5), and $\tilde{r}_q^{\mathrm{F}}$ and $\tilde{r}_q^{\mathrm{S}}$ denote the IFORM and ISORM approximations of $\tilde{r}_q$. Similarly, r_q was found by applying numerical integration to the formulation Eqn. (5.4) and the reliability method approximations are denoted r_q^{F} and r_q^{S}. For r_q^{F} and r_q^{S}, different values of the constant C in Eqns. (5.8) and (5.10) could be used. In this paper, $C = 1$ is used for r_q^{F}, while the values $C = 1$, $C = 10^4$ and $C = 10^6$ are used for r_q^{S}.

For the calculation of $\tilde{r}_q$ and r_q by numerical integration, the ranges of the integration variables were $H_s \in [0, 10]$ m, $T_z \in [0.4, 20]$ s, and $\bar{\Theta} \in [-\pi, 0]$. The applied bin sizes were $\Delta H_s = 0.1$ m, $\Delta T_z = 0.2$ s, $\Delta\bar{\Theta} = \pi/39$ for EM1, $\Delta H_s = 0.05$ m, $\Delta\bar{\Theta} = \pi/39$ for EM2 and $\Delta H_s = 0.05$ m, $\Delta T_z = 0.05$ s for EM3 and EM4. It should be noted that these ranges and bin sizes are chosen such that $\tilde{r}_q$ and r_q can be regarded as exact values, and the number of integration points may therefore be excessive.

The obtained values for the characteristic extreme response estimates are presented in Tabs. 5.4 and 5.5 for annual exceedance probabilities $q = 10^{-2}$ and $q = 10^{-4}$, respectively. When compared to the values $\tilde{r}_q$ and r_q, it is seen that the reliability method approximations provide reasonable estimates for the characteristic response value. Especially the ISORM method with C chosen as 10^4 or 10^6 yields very good estimates.

In Tabs. 5.4 and 5.5, the characteristic response values are seen to vary quite a lot between the different environmental models. This is a result of the response being very sensitive to the zero-crossing period T_z. In Fig. 5.11 it is seen that large values of T_z have a larger probability of occurrence for EM4 than for EM3, resulting in a significantly larger extreme response. For EM2, T_z is fixed at its median value, disregarding large values of T_z. This results in a smaller extreme response for EM2. EM1 and EM3, on the other hand, have the same model for T_z and give quite similar results.

For each of the extreme response estimates in Tabs. 5.4 and 5.5, the corresponding number of executed short-term response calculations, denoted

by n_{st} or similar, is reported in Tabs. 5.6 and 5.7. It is clear that IFORM and ISORM represent efficient methods for full long-term extreme response analysis. ISORM roughly doubles the computational effort compared to IFORM.

5.5.2.2 Environmental contour method

Using some common choices for the fractile level p, characteristic extreme response estimates denoted r_q^p were obtained for the environmental contour method. These estimates are presented in Tabs. 5.8 and 5.9 for annual exceedance probabilities $q = 10^{-2}$ and $q = 10^{-4}$ respectively. Comparing these results to the exact long-term extreme response r_q in Tabs. 5.4 and 5.5, we observe that all the considered choices of p give reasonable rough estimates for the long-term response.

The exact fractile levels corresponding to the full long-term estimates can also be calculated. For the exact extreme response value r_q, the corresponding fractile level is given as

$$p_q = F_{\tilde{R}|\boldsymbol{W}}(r_q|\hat{\boldsymbol{w}}).$$

Table 5.10 shows the fractile levels corresponding to the exact extreme response values r_q in Tabs. 5.4 and 5.5. We see that there is a large variation in the obtained fractiles, indicating that one single fractile level does not give accurate estimates for all the considered cases. However, as seen in Tabs. 5.8 and 5.9, rough estimates can still be obtained. When regarded as rough approximations, Tabs. 5.8 and 5.9 show that the extreme response estimates are generally not overly sensitive to changing fractile levels. Still, if the fractile level should be much larger than 0.9, which is the case for EM3 and EM4 when $q = 10^{-2}$, the environmental contour method may underestimate the extreme response quite severely.

Considering Tabs. 5.8–5.10, reasonable choices for the fractile values are perhaps $p = 0.95$ for $q = 10^{-2}$ and $p = 0.80$ for $q = 10^{-4}$. Thus, p has a larger value for the highest annual exceedance probability. This is in contrast to the choices of $p = 0.90$ for $q = 10^{-2}$ and $p = 0.95$ for $q = 10^{-4}$, which are common for offshore structures [29]. It should also be noted that instead of using r_q, which is obtained by full numerical integration, the IFORM and ISORM estimates can be used to determine appropriate values for the fractile levels.

Table 5.4: The characteristic extreme response values as calculated by the different methods for an annual exceedance probability $q = 10^{-2}$.

	Approximate formulation			Exact formulation				
					r_q^{S}[cm]			
	$\tilde{r}_q^{\mathrm{F}}$[cm]	$\tilde{r}_q^{\mathrm{S}}$[cm]	$\tilde{r}_q$[cm]	r_q^{F}[cm]	$C = 1$	$C = 10^4$	$C = 10^6$	r_q[cm]
EM1	56.4	48.7	54.4	56.8	49.6	58.7	58.5	61.8
EM2	2.52	2.39	2.42	2.54	2.42	2.55	2.55	2.58
EM3	53.3	49.7	51.6	53.7	50.6	61.0	60.8	62.1
EM4	246.8	243.4	243.4	249.2	248.3	284.9	284.6	284.6

Table 5.5: The characteristic extreme response values as calculated by the different methods for an annual exceedance probability $q = 10^{-4}$.

	Approximate formulation			Exact formulation				
					r_q^{S}[cm]			
	$\tilde{r}_q^{\mathrm{F}}$[cm]	$\tilde{r}_q^{\mathrm{S}}$[cm]	$\tilde{r}_q$[cm]	r_q^{F}[cm]	$C = 1$	$C = 10^4$	$C = 10^6$	r_q[cm]
EM1	97.0	83.5	85.2	97.7	85.2	92.8	92.4	92.6
EM2	3.47	3.30	3.33	3.47	3.33	3.39	3.39	3.41
EM3	97.0	87.5	87.8	97.8	89.1	96.8	96.7	97.2
EM4	406.3	398.5	398.0	408.2	403.9	420.3	420.1	420.1

Table 5.6: The number of short-term response calculations performed for each of the long-term extreme response estimates in Tab. 5.4.

	Approximate formulation			Exact formulation				
					$n_{\mathrm{st}}^{\mathrm{S}}$			
	$\tilde{n}_{\mathrm{st}}^{\mathrm{F}}$	$\tilde{n}_{\mathrm{st}}^{\mathrm{S}}$	$\tilde{n}_{\mathrm{st}}$	$n_{\mathrm{st}}^{\mathrm{F}}$	$C = 1$	$C = 10^4$	$C = 10^6$	n_{st}
EM1	19	87	399960	23	111	111	113	399960
EM2	43	81	8040	43	81	71	67	8040
EM3	61	113	78993	60	117	225	147	78993
EM4	33	67	78993	33	67	81	177	78993

Table 5.7: The number of short-term response calculations performed for each of the long-term extreme response estimates in Tab. 5.5.

	Approximate formulation			Exact formulation				
					$n_{\mathrm{st}}^{\mathrm{S}}$			
	$\tilde{n}_{\mathrm{st}}^{\mathrm{F}}$	$\tilde{n}_{\mathrm{st}}^{\mathrm{S}}$	$\tilde{n}_{\mathrm{st}}$	$n_{\mathrm{st}}^{\mathrm{F}}$	$C = 1$	$C = 10^4$	$C = 10^6$	n_{st}
EM1	13	104	399960	18	110	109	126	399960
EM2	57	95	8040	57	94	89	85	8040
EM3	160	276	78993	256	384	167	155	78993
EM4	101	159	78993	105	151	82	190	78993

Table 5.8: The characteristic extreme response values as calculated by the environmental contour method using different quantile levels p for an annual exceedance probability $q = 10^{-2}$. The corresponding design points are illustrated by diamond markers in Figs. 5.12 and 5.13.

	r_q^p[cm]			
	$p = 0.80$	$p = 0.85$	$p = 0.90$	$p = 0.95$
EM1	58.6	59.6	61.0	63.3
EM2	2.60	2.64	2.69	2.79
EM3	55.3	56.2	57.6	59.7
EM4	258.5	263.3	269.7	280.1

Table 5.9: The characteristic extreme response values as calculated by the environmental contour method using different quantile levels p for an annual exceedance probability $q = 10^{-4}$. The corresponding design points are illustrated by diamond markers in Figs. 5.12 and 5.13.

	r_q^p[cm]			
	$p = 0.80$	$p = 0.85$	$p = 0.90$	$p = 0.95$
EM1	101.0	102.9	105.4	109.5
EM2	3.50	3.56	3.63	3.76
EM3	100.9	102.8	105.4	109.5
EM4	418.1	425.9	436.5	453.4

Table 5.10: The fractile levels p_q corresponding to the exact extreme response values r_q in Tabs. 5.4 and 5.5.

	EM1	EM2	EM3	EM4
p_q, $q = 10^{-2}$	0.92	0.77	0.98	0.96
p_q, $q = 10^{-4}$	0.43	0.69	0.66	0.81

5.5.3 Design points

In addition to giving an estimate for the characteristic extreme response, the inverse reliability methods will produce a design point which represents the most critical combination of environmental parameters for the specified annual exceedance probability q. The design point corresponding to the ISORM estimate r_q^{S} ($C = 10^6$) is shown in Fig. 5.12 for EM1. In Fig. 5.13 the design points are shown for the two-dimensional environmental models EM2, EM3 and EM4, also including the IFORM design points corresponding to the estimates r_q^{F} ($C = 1$). In addition, the contour method design points are shown in Figs. 5.12 and 5.13. As explained in Section 5.4.5, these have been obtained by maximizing the median value of the short-term CDF $F_{\tilde{R}|\boldsymbol{W}}(r|\boldsymbol{w})$ on the respective contours.

The relative contribution of different sea states to the long-term integral in Eqn. (5.4) is illustrated in Figs. 5.12 and 5.13 by the function $g(\boldsymbol{w})$. This function is defined as a normalized version of the integrand in Eqn. (5.4) for $r = r_q$. Specifically,

$$g(\boldsymbol{w}) = -\frac{1}{M} \ln\left(F_{\tilde{R}|\boldsymbol{W}}(r_q|\boldsymbol{w})\right) f_{\boldsymbol{W}}(\boldsymbol{w}),$$

where M is chosen such that the maximal value of $g(\boldsymbol{w})$ equals unity.

By considering Figs. 5.12 and 5.13, we observe that the main contribution to the long-term integral is located within a rather concentrated region. Furthermore, the design points quite successfully locate this region. The ISORM design point ($C = 10^6$) almost exactly pinpoints the location of the largest contribution. However, local maxima other than the main contribution might occur. This can be observed in the left part of Fig. 5.12, corresponding to $q = 10^2$ for EM1. If such a local maximum represent a significant contribution, this may result in an underestimation of the long-term extreme response as seen in the first row of Tab. 5.4. This is a known shortcoming of the inverse reliability methods, and they should therefore be used with some caution.

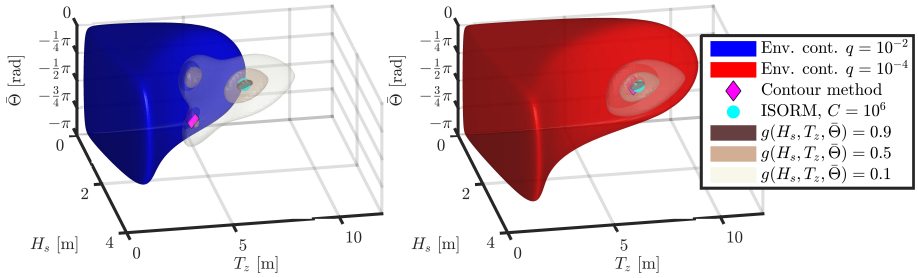

Figure 5.12: The design points corresponding to the characteristic extreme response value r_q^{S} (ISORM, $C = 10^6$) and the environmental contour method for annual exceedance probabilities $q = 10^{-2}$ (left) and $q = 10^{-4}$ (right). The contribution $g(\boldsymbol{w})$ to the long-term integral is also illustrated by displaying isosurfaces for the values 0.9, 0.5 and 0.1.

5.6 Concluding remarks

A framework for full long-term extreme response analysis has been demonstrated for a long-span case study bridge. Using recently developed IFORM and ISORM approaches, the extreme response was calculated in an efficient manner. Comparison with full numerical integration revealed that especially the ISORM method gives high accuracy. It has thus been shown that the proposed framework can be applied successfully for complex structures. Still, limitations do exist, e.g. in the presence of multiple local maxima for the contribution to the long-term integral. Therefore, future work should focus on comparison with alternative approaches and further verification of the IFORM and ISORM methods, especially for nonlinear response.

The full long-term analysis was also compared with the environmental contour method. The results show that the contour method can be used to obtain rough estimates of the long-term extreme response. Furthermore, a proper fractile level p could be determined by comparison with the IFORM and ISORM results.

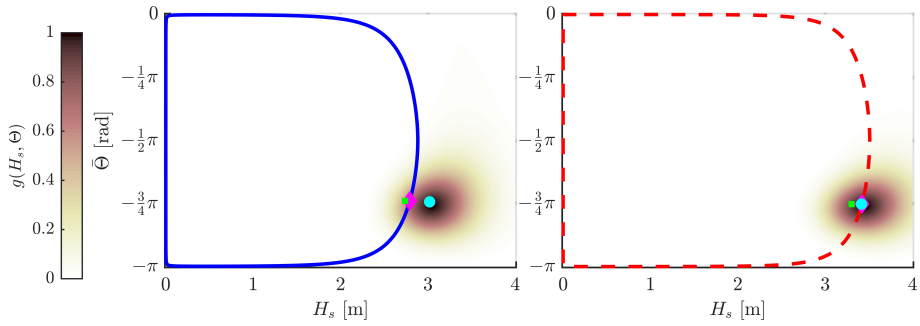

(a) EM2

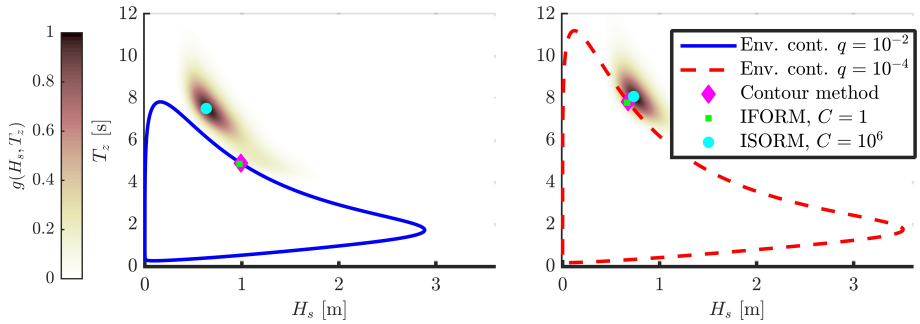

(b) EM3

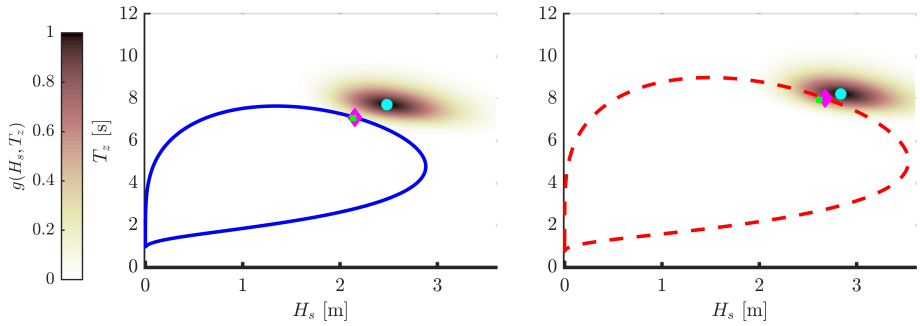

(c) EM4

Figure 5.13: The design points corresponding to the characteristic extreme response values r_q^{F} (IFORM, $C = 1$), r_q^{S} (ISORM, $C = 10^6$) and the environmental contour method for annual exceedance probabilities $q = 10^{-2}$ (left) and $q = 10^{-4}$ (right). The contribution $g(\boldsymbol{w})$ to the long-term integral is also illustrated in each case.

Appendix:

APPENDIX A

An error bound for the series expansion method

In this appendix, an error bound is derived for the series expansion method presented in Chapter 2 (Paper I). In order to establish some notation, a slightly extended derivation of the series expansion method is included in Section A.1. In Section A.2 the error bound is derived.

A.1 The series expansion of the complex coherency

The expression for the cross-spectral densities is given by (2.22), which is repeated here for convenience:

$$\frac{S_{q_\mu q_\nu}(\omega)}{S_{\eta\eta}(\omega)} = \int_{-\pi}^{\pi} \Psi(\theta,\omega)\, f_\mu(\theta-\alpha_m,\omega)\overline{f_\nu(\theta-\alpha_n,\omega)} e^{-i\kappa(\omega)(\Delta x\cos\theta+\Delta y\sin\theta)} d\theta. \tag{A.1}$$

Now if the product $\Psi(\theta,\omega)\, f_\mu(\theta-\alpha_m,\omega)\overline{f_\nu(\theta-\alpha_n,\omega)}$ is written as a Fourier series in θ, the integral (A.1) can be solved using the same approach as in Section 2.2.4. Having

$$\Psi(\theta,\omega) f_\mu(\theta-\alpha_m,\omega)\overline{f_\nu(\theta-\alpha_n,\omega)} = \sum_{k=-\infty}^{\infty} C_k^{\mu\nu}(\omega)\, e^{ik\theta}, \tag{A.2}$$

yields the cross-spectral densities

$$S_{q_\mu q_\nu}(\omega) = 2\pi S_{\eta\eta}(\omega) \sum_{k=-\infty}^{\infty} C_k^{\mu\nu}(\omega) i^k e^{-ik\beta} J_k(\kappa(\omega)L), \tag{A.3}$$

where L and β are given as

$$L = \sqrt{\Delta x^2 + \Delta y^2},$$
$$\beta = \bar{\theta} + \pi - \operatorname{atan2}(\Delta y, \Delta x).$$

The transfer functions $f_\mu(\tilde{\beta}, \omega)$ are usually known only by their values at a finite number of heading angles $\tilde{\beta}$. For our purposes it is convenient to extend these point values to continuous functions $f_\mu(\tilde{\beta}, \omega)$ using trigonometric interpolation [31, 38]. This means that the transfer functions are given by trigonometric polynomials

$$f_\mu(\tilde{\beta}, \omega) = \sum_{k=-N_f}^{N_f} a_k^\mu(\omega)\, e^{ik\tilde{\beta}}. \tag{A.4}$$

If the transfer function values are given at a number $N_{\tilde{\beta}}$ of heading angles, uniformly distributed on the interval $[0, 2\pi)$, the coefficients $a_k^\mu(\omega)$ can be efficiently computed using FFT, and we have that $N_f = \lfloor N_{\tilde{\beta}}/2 \rfloor$. With transfer functions given by (A.4) we find that

$$f_\mu(\theta - \alpha_m, \omega) = \sum_{k=-N_f}^{N_f} \left(e^{-ik\alpha_m} a_k^\mu(\omega)\right) e^{ik\theta} \tag{A.5}$$

and

$$\overline{f_\nu(\theta - \alpha_n, \omega)} = \sum_{k=-N_f}^{N_f} \left(\overline{e^{-ik\alpha_n} a_k^\nu(\omega)}\right) e^{-ik\theta} = \sum_{k=-N_f}^{N_f} \left(\overline{e^{ik\alpha_n} a_{-k}^\nu(\omega)}\right) e^{ik\theta}. \tag{A.6}$$

It can be shown that the Fourier coefficients of a product can be obtained by taking the convolution of the Fourier coefficients of the factors. Hence, we have that

$$f_\mu(\theta - \alpha_m, \omega)\, \overline{f_\nu(\theta - \alpha_n, \omega)} = \sum_{k=-2N_f}^{2N_f} A_k^{\mu\nu}(\omega)\, e^{ik\theta},$$

where the coefficients $A_k^{\mu\nu}$ are computed by taking the convolution between the coefficients in (A.5) and (A.6), i.e.

$$A_k^{\mu\nu}(\omega) = \sum_{j=-N_f+\max(0,k)}^{N_f+\min(0,k)} e^{-ij\alpha_m} a_j^\mu(\omega)\, \overline{e^{i(k-j)\alpha_n} a_{-(k-j)}^\nu(\omega)}.$$

Finally, with a spreading function given by $\Psi(\theta,\omega) = \sum_{k=-\infty}^{\infty} c_k(\omega)\, e^{ik\theta}$, the Fourier coefficients $C_k^{\mu\nu}(\omega)$ in (A.2) are given by the convolution

$$C_k^{\mu\nu}(\omega) = \sum_{r=-2N_f}^{2N_f} A_r^{\mu\nu}(\omega)\, c_{k-r}(\omega). \tag{A.7}$$

If the spreading function $\Psi(\theta,\omega)$ has a finite number of Fourier coefficients $\{c_k(\omega)\}_{k=-N_d}^{N_d}$, we will have that $C_k^{\mu\nu}(\omega) = 0$ for $k > 2N_f + N_d$, and the series expansion (A.3) will be finite. Specifically we have then that

$$S_{q_\mu q_\nu}(\omega) = 2\pi S_{\eta\eta}(\omega) \sum_{k=-N_{\text{tot}}}^{N_{\text{tot}}} C_k^{\mu\nu}(\omega) i^k e^{-ik\beta} J_k(\kappa(\omega)L),$$

where $N_{\text{tot}} = 2N_f + N_D$.

It is worth noticing that for the cross-spectral densities between loads at the same location we have that $m = n$ and thus $L = 0$. Using the fact that $J_k(0) = 0$ for $k \in \{\pm 1, \pm 2, \dots\}$ and $J_0(0) = 1$ yields the result

$$S_{q_\mu q_\nu}(\omega) = 2\pi S_{\eta\eta}(\omega) C_0^{\mu\nu}(\omega),$$

which holds whenever $m = n$, or equivalently $\lceil \mu/6 \rceil = \lceil \nu/6 \rceil$. As a special case, the auto-spectral densities are given by

$$S_{q_\mu q_\mu}(\omega) = 2\pi S_{\eta\eta}(\omega) C_0^{\mu\mu}(\omega),$$

which yields the following formula for the complex coherencies:

$$\gamma_{q_\mu q_\nu}(\omega) = \frac{S_{q_\mu q_\nu}(\omega)}{\sqrt{S_{q_\mu q_\mu}(\omega) S_{q_\nu q_\nu}(\omega)}} = \sum_{k=-\infty}^{\infty} \frac{C_k^{\mu\nu}(\omega)}{\sqrt{C_0^{\mu\mu}(\omega) C_0^{\nu\nu}(\omega)}} i^k e^{-ik\beta} J_k(\kappa(\omega)L). \tag{A.8}$$

The series expansion method is now obtained by truncating the above series. Specifically, the complex coherencies are approximated by

$$\widehat{\gamma_{q_\mu q_\nu}}(\omega) = \sum_{k=-\hat{N}}^{\hat{N}} \frac{C_k^{\mu\nu}(\omega)}{\sqrt{C_0^{\mu\mu}(\omega) C_0^{\nu\nu}(\omega)}} i^k e^{-ik\beta} J_k(\kappa(\omega)L). \tag{A.9}$$

A.2 An error bound for the series expansion method

The error that is made when the complex coherency (A.8) is approximated by the truncated series (A.9), is given by

$$\begin{aligned}\hat{E}^{\mu\nu}(\omega) &= \left|\gamma_{q_\mu q_\nu}(\omega) - \widehat{\gamma_{q_\mu q_\nu}}(\omega)\right| \\ &= \left|\sum_{|k|\geq\hat{N}+1} \frac{C_k^{\mu\nu}(\omega)}{\sqrt{C_0^{\mu\mu}(\omega)}\sqrt{C_0^{\nu\nu}(\omega)}} i^k e^{-ik\beta} J_k(\kappa(\omega)L)\right|.\end{aligned}$$

Using the triangle inequality and the error bound for the Bessel functions found in [43] yields

$$\hat{E}^{\mu\nu}(\omega) \leq \frac{b|\hat{N}+1|^{-1/3}}{\sqrt{C_0^{\mu\mu}(\omega)}\sqrt{C_0^{\nu\nu}(\omega)}} \sum_{|k|\geq\hat{N}+1} |C_k^{\mu\nu}(\omega)|,$$

where $b = 0.674886$. The coefficients $C_k^{\mu\nu}(\omega)$ are bounded using the expression (A.7), and we find that

$$\hat{E}^{\mu\nu}(\omega) \leq \frac{b|\hat{N}+1|^{-1/3}}{\sqrt{C_0^{\mu\mu}(\omega)}\sqrt{C_0^{\nu\nu}(\omega)}} \sum_{r=-2N_f}^{2N_f} |A_r^{\mu\nu}(\omega)| \sum_{|k|\geq\hat{N}+1} |c_{k-r}(\omega)|.$$

Since the spreading function is a real function, we have that $c_{-k}(\omega) = \overline{c_k(\omega)}$ and we have

$$\sum_{|k|\geq\hat{N}+1} |c_{k-r}(\omega)| = \sum_{k=\hat{N}-r+1}^{\infty} |c_k(\omega)| + \sum_{k=\hat{N}+r+1}^{\infty} |c_k(\omega)|.$$

For simplicity, we assume that $\hat{N} \geq 2N_f$ such that

$$\sum_{|k|\geq\hat{N}+1} |c_{k-r}(\omega)| = 2\sum_{k=1}^{\infty} |c_k(\omega)| - \left(\sum_{k=1}^{\hat{N}-r} |c_k(\omega)| + \sum_{k=1}^{\hat{N}+r} |c_k(\omega)|\right),$$

for $|r| \leq 2N_f$. This yields the error bound

$$\begin{aligned}\hat{E}^{\mu\nu}(\omega) \leq{}& \frac{b|\hat{N}+1|^{-1/3}}{\sqrt{C_0^{\mu\mu}(\omega)}\sqrt{C_0^{\nu\nu}(\omega)}} \\ & \sum_{r=-2N_f}^{2N_f} |A_r^{\mu\nu}(\omega)| \left(2\sum_{k=1}^{\infty} |c_k(\omega)| - \left(\sum_{k=1}^{\hat{N}-r} |c_k(\omega)| + \sum_{k=1}^{\hat{N}+r} |c_k(\omega)|\right)\right).\end{aligned}$$

For the total error $\hat{E} = \max_{\mu,\nu,\omega} \hat{E}^{\mu\nu}(\omega)$ we obtain the error bound

$$\hat{E} \leq b|\hat{N}+1|^{-1/3} \max_{\mu,\nu,\omega} \left\{ \sum_{r=-2N_f}^{2N_f} \frac{|A_r^{\mu\nu}(\omega)|}{\sqrt{C_0^{\mu\mu}(\omega)}\sqrt{C_0^{\nu\nu}(\omega)}} \left(2\sum_{k=1}^{\infty} |c_k(\omega)| - \left(\sum_{k=1}^{\hat{N}-r} |c_k(\omega)| + \sum_{k=1}^{\hat{N}+r} |c_k(\omega)| \right) \right) \right\}. \tag{A.10}$$

The error bound (A.10) makes it possible to find a number of terms $\hat{N}$ such that the error is guaranteed to be less than a given tolerance. The absolute sum $\sum_{k=1}^{\infty} |c_k(\omega)|$ of the Fourier coefficients of the spreading function must, however, be known. For the *cos-2s* spreading function given by

$$\Psi(\theta,\omega) = \frac{2^{2s(\omega)}\Gamma^2(s(\omega)+1)}{2\pi\Gamma(2s(\omega)+1)} \cos^{2s(\omega)} \frac{\theta-\bar{\theta}}{2},$$

it can be shown that

$$\sum_{k=1}^{\infty} |c_k(\omega)| = \begin{cases} 2\sum_{k=1}^{\lceil s(\omega)\rceil/2} c_{2k-1}(\omega) - \frac{c_0(\omega)}{2}, & \text{if } \lceil s(\omega)\rceil \text{ is even,} \\ 2\sum_{k=1}^{(\lceil s(\omega)\rceil-1)/2} c_{2k}(\omega) + \frac{c_0(\omega)}{2}, & \text{if } \lceil s(\omega)\rceil \text{ is odd.} \end{cases}$$

References

[1] Abramowitz, M. and Stegun, I. *Handbook of Mathematical Functions with Formulas, Graphs, and Mathematical Tables*. U.S. Department of Commerce, NIST, 1972. URL: http://app.knovel.com/hotlink/toc/id:kpHMFFGMT1/handbook-mathematical/handbook-mathematical.

[2] Agarwal, P. and Manuel, L. 'Simulation of offshore wind turbine response for long-term extreme load prediction'. *Engineering Structures* 31.10 (2009), pp. 2236–2246. DOI: 10.1016/j.engstruct.2009.04.002.

[3] Armijo, L. 'Minimization of functions having Lipschitz continuous first partial derivatives'. *Pacific Journal of Mathematics* 16.1 (1966), pp. 1–3. DOI: 10.2140/pjm.1966.16.1.

[4] Au, S. K. and Beck, J. L. 'First excursion probabilities for linear systems by very efficient importance sampling'. *Probabilistic Engineering Mechanics* 16.3 (2001), pp. 193–207. DOI: 10.1016/S0266-8920(01)00002-9.

[5] Au, S. K. and Beck, J. L. 'Estimation of small failure probabilities in high dimensions by subset simulation'. *Probabilistic Engineering Mechanics* 16.4 (2001), pp. 263–277. DOI: 10.1016/S0266-8920(01)00019-4.

[6] Battjes, J. A. *Long-term wave height distributions at seven stations around the British Isles*. Tech. rep. Wormley, UK: National Institute of Oceanography, 1970.

[7] Battjes, J. A. 'Long-term wave height distributions at seven stations around the British Isles'. *Deutsche Hydrographische Zeitschrift* 25.4 (1972), pp. 179–189. DOI: 10.1007/BF02312702.

[8] Bitner-Gregersen, E. M. and Haver, S. 'Joint environmental model for reliability calculations'. *Proceedings of the First (1991) International Offshore and Polar Engineering Conference*. Edinburgh, United Kingdom: International Society of Offshore and Polar Engineers, 1991, pp. 246–253. URL: https://www.onepetro.org/conference-paper/ISOPE-I-91-031.

[9] Breitung, K. '40 years FORM: Some new aspects?' *Probabilistic Engineering Mechanics* 42 (2015), pp. 71–77. DOI: 10.1016/j.probengmech.2015.09.012.

[10] Breitung, K. 'Asymptotic approximations for multinormal integrals'. *Journal of Engineering Mechanics* 110.3 (1984), pp. 357–366. DOI: 10.1061/(ASCE)0733-9399(1984)110:3(357).

[11] Ching, J., Beck, J. L. and Au, S. K. 'Hybrid Subset Simulation method for reliability estimation of dynamical systems subject to stochastic excitation'. *Probabilistic Engineering Mechanics* 20.3 (2005), pp. 199–214. DOI: 10.1016/j.probengmech.2004.09.001.

[12] Dassault Systèmes Simulia Corp. *Abaqus 6.14*. Providence, Rhode Island, USA, 2014.

[13] Der Kiureghian, A., Zhang, Y. and Li, C.-C. 'Inverse reliability problem'. *Journal of Engineering Mechanics* 120.5 (1994), pp. 1154–1159. DOI: 10.1061/(ASCE)0733-9399(1994)120:5(1154).

[14] Det Norske Veritas (DNV). *Environmental Conditions and Environmental Loads*. Tech. rep. DNV-RP-C205. Høvik, Norway, 2010, pp. 1–124. URL: https://rules.dnvgl.com/docs/pdf/DNV/codes/docs/2010-10/RP-C205.pdf.

[15] Det Norske Veritas (DNV). *SESAM User Manual - Wadam Wave Analysis by Diffraction and Morison Theory*. 2014.

[16] Det Norske Veritas (DNV). *WADAM*. Høvik, Norway, 2014.

[17] Du, X., Sudjianto, A. and Chen, W. 'An integrated framework for optimization under uncertainty using inverse reliability strategy'. *Journal of Mechanical Design* 126.4 (2004), pp. 562–570. DOI: 10.1115/1.1759358.

[18] Dubourg, V., Sudret, B. and Bourinet, J.-M. 'Reliability-based design optimization using kriging surrogates and subset simulation'. *Structural and Multidisciplinary Optimization* 44.5 (2011), pp. 673–690. DOI: 10.1007/s00158-011-0653-8.

[19] Georgiadis, C. and Hartz, B. J. *Wave Coherence Along Continuous Structures for Directional Spectral Models*. Tech. rep. Trondheim, Norway: SINTEF, 1982. URL: http://www.runet-software.com/documents/Wavecoherence.pdf.

[20] Giske, F.-I. G., Leira, B. J. and Øiseth, O. 'Efficient computation of cross-spectral densities in the stochastic modelling of waves and wave loads'. *Applied Ocean Research* 62 (2017), pp. 70–88. DOI: 10.1016/j.apor.2016.11.007.

[21] Giske, F.-I. G., Leira, B. J. and Øiseth, O. 'Full long-term extreme response analysis of marine structures using inverse FORM'. *Probabilistic Engineering Mechanics* 50 (2017), pp. 1–8. DOI: 10.1016/j.probengmech.2017.10.007.

[22] Giske, F.-I. G., Leira, B. J. and Øiseth, O. 'Long-term extreme response analysis of marine structures using inverse SORM'. *Submitted for journal publication* (2017).

[23] Giske, F.-I. G., Leira, B. J. and Øiseth, O. 'Long-term extreme response analysis of marine structures using inverse SORM'. *ASME 2017 36th International Conference on Ocean, Offshore and Arctic Engineering*. Vol. 3A. ASME, 2017. DOI: 10.1115/OMAE2017-61409.

[24] Giske, F.-I. G., Leira, B. J. and Øiseth, O. 'Long-term stochastic extreme response analysis of floating bridges'. *Procedia Engineering* 199 (2017), pp. 1175–1180. DOI: 10.1016/j.proeng.2017.09.305.

[25] Giske, F.-I. G., Leira, B. J. and Øiseth, O. 'Stochastic modelling of wave loads on floating bridges: efficient calculation of cross-spectral densities'. *IABSE Congress Report*. Vol. 19. IABSE, 2016, pp. 48–56.

[26] Giske, F.-I. G., Kvåle, K. A., Leira, B. J. and Øiseth, O. 'Long-term extreme response analysis of a long-span pontoon bridge'. *Marine Structures* 58 (2018), pp. 154–171. DOI: 10.1016/j.marstruc.2017.11.010.

[27] Hasselmann, D. E., Dunckel, M. and Ewing, J. A. 'Directional wave spectra observed during JONSWAP 1973'. *Journal of Physical Oceanography* 10.8 (1980), pp. 1264–1280. DOI: 10.1175/1520-0485(1980)010<1264:DWSODJ>2.0.CO;2.

[28] Hauser, D, Kahma, K and Krogstad, H. *Measuring and Analysing the Directional Spectra of Ocean Waves*. Luxembourg: Publications Office of the European Union, 2005. URL: http://www.envia.bl.uk/handle/123456789/4300.

[29] Haver, S. and Winterstein, S. 'Environmental contour lines: a method for estimating long term extremes by a short term analysis'. *Transactions of the Society of Naval Architects and Marine Engineers* 116 (2010), pp. 116–127. URL: http://www.sname.org/HigherLogic/System/DownloadDocumentFile.ashx?DocumentFileKey=ccb5aac7-6b77-420b-b233-836fc6e13597.

[30] Haver, S. and Kleiven, G. 'Environmental contour lines for design purposes: why and when?' *Proceedings of the ASME 2004 23rd International Conference on Offshore Mechanics and Arctic Engineering*. Vol. 1. 2004, pp. 337–345. DOI: 10.1115/OMAE2004-51157.

[31] Henrici, P. 'Fast Fourier methods in computational complex analysis'. *Siam Review* 21.4 (1979), pp. 481–527. DOI: 10.1137/1021093.

[32] Huseby, A. B., Vanem, E. and Natvig, B. 'A new approach to environmental contours for ocean engineering applications based on direct Monte Carlo simulations'. *Ocean Engineering* 60 (2013), pp. 124–135. DOI: 10.1016/j.oceaneng.2012.12.034.

[33] Huseby, A. B., Vanem, E. and Natvig, B. 'Alternative environmental contours for structural reliability analysis'. *Structural Safety* 54 (2015), pp. 32–45. DOI: 10.1016/j.strusafe.2014.12.003.

[34] Iserles, A. 'On the numerical quadrature of highly-oscillating integrals II: irregular oscillators'. *IMA Journal of Numerical Analysis* 25.1 (2005), pp. 25–44. DOI: 10.1093/imanum/drh022.

[35] Jensen, J. J. and Capul, J. 'Extreme response predictions for jack-up units in second order stochastic waves by FORM'. *Probabilistic Engineering Mechanics* 21.4 (2006), pp. 330–337. DOI: 10.1016/J.PROBENGMECH.2005.11.007.

[36] Jensen, J. J., Olsen, A. S. and Mansour, A. E. 'Extreme wave and wind response predictions'. *Ocean Engineering* 38.17-18 (2011), pp. 2244–2253. DOI: 10.1016/J.OCEANENG.2011.10.003.

[37] Koepf, W. *Hypergeometric Summation*. Universitext. London: Springer London, 2014. DOI: 10.1007/978-1-4471-6464-7.

[38] Kress, R. *Numerical Analysis*. Vol. 181. Graduate Texts in Mathematics. New York, NY: Springer New York, 1998. DOI: 10.1007/978-1-4612-0599-9.

[39] Krogstad, H. E. 'Height and period distributions of extreme waves'. *Applied Ocean Research* 7.3 (1985), pp. 158–165. DOI: 10.1016/0141-1187(85)90008-2.

[40] Krogstad, H. E. and Barstow, S. F. 'Directional distributions in ocean wave spectra'. *The Ninth International Offshore and Polar Engineering Conference*. International Society of Offshore and Polar Engineers, 1999, pp. 79–86. URL: https://www.onepetro.org/conference-paper/ISOPE-I-99-237.

[41] Kvåle, K. A., Øiseth, O. and Sigbjörnsson, R. 'Modelling of the stochastic dynamic behaviour of the Bergsøysund Bridge: an application of the power spectral density method'. *IX International Conference on Structural Dynamics, EURODYN 2014*. Vol. 1. 2014, pp. 2921–2928. URL: http://paginas.fe.up.pt/~eurodyn2014/CD/papers/406_MS16_ABS_1301.pdf.

[42] Kvåle, K. A., Sigbjörnsson, R. and Øiseth, O. 'Modelling the stochastic dynamic behaviour of a pontoon bridge: a case study'. *Computers & Structures* 165 (2016), pp. 123–135. DOI: 10.1016/j.compstruc.2015.12.009.

[43] Landau, L. J. 'Bessel functions: monotonicity and bounds'. *Journal of the London Mathematical Society* 61.1 (2000), pp. 197–215. DOI: 10.1112/S0024610799008352.

[44] Langen, I. *Frequency Domain Analysis of a Floating Bridge Exposed to Irregular Short-crested Waves*. Tech. rep. Trondheim, Norway: SINTEF, 1980.

[45] Langen, I. and Sigbjörnsson, R. 'On stochastic dynamics of floating bridges'. *Engineering Structures* 2.4 (1980), pp. 209–216. DOI: 10.1016/0141-0296(80)90002-4.

[46] Lee, I., Noh, Y. and Yoo, D. 'A novel second-order reliability method (SORM) using noncentral or generalized chi-squared distributions'. *Journal of Mechanical Design* 134.10 (2012). DOI: 10.1115/1.4007391.

[47] Li, H. and Foschi, R. O. 'An inverse reliability method and its application'. *Structural Safety* 20.3 (1998), pp. 257–270. DOI: 10.1016/S0167-4730(98)00010-1.

[48] Li, Q., Gao, Z. and Moan, T. 'Modified environmental contour method for predicting long-term extreme responses of bottom-fixed offshore wind turbines'. *Marine Structures* 48 (2016), pp. 15–32. DOI: 10.1016/j.marstruc.2016.03.003.

[49] Lim, J., Lee, B. and Lee, I. 'Second-order reliability method-based inverse reliability analysis using Hessian update for accurate and efficient reliability-based design optimization'. *International Journal for Numerical Methods in Engineering* 100.10 (2014), pp. 773–792. DOI: 10.1002/nme.4775.

[50] Longuet-Higgins, M., Cartwright, D. and Smith, N. 'Observations of the directional spectrum of sea waves using the motions of a floating buoy'. *Ocean Wave Spectra*. 1961, pp. 111–132. URL: https://books.google.no/books/about/Ocean_wave_spectra.html?id=D1JVAAAAMAAJ&pgis=1.

[51] Low, Y. M. and Cheung, S. H. 'On the long-term fatigue assessment of mooring and riser systems'. *Ocean Engineering* 53 (2012), pp. 60–71. DOI: 10.1016/j.oceaneng.2012.06.017.

[52] Lwin, M. M. 'Floating Bridges'. *Bridge Engineering Handbook*. Ed. by W.-F. Chen and L. Duan. Boca Raton: CRC Press, 2000. Chap. 22.

[53] Melchers, R. E. *Structural Reliability Analysis and Prediction*. 2nd ed. Chichester: John Wiley & Sons, 1999.

[54] Mitsuyasu, H., Tasai, F., Suhara, T., Mizuno, S., Ohkusu, M., Honda, T. and Rikiishi, K. 'Observations of the directional spectrum of ocean waves using a cloverleaf buoy'. *Journal of Physical Oceanography* 5.4 (1975), pp. 750–760. DOI: 10.1175/1520-0485(1975)005<0750:OOTDSO>2.0.CO;2.

[55] Montes-Iturrizaga, R. and Heredia-Zavoni, E. 'Environmental contours using copulas'. *Applied Ocean Research* 52 (2015), pp. 125–139. DOI: 10.1016/j.apor.2015.05.007.

[56] Naess, A. and Gaidai, O. 'Estimation of extreme values from sampled time series'. *Structural Safety* 31.4 (2009), pp. 325–334. DOI: 10.1016/j.strusafe.2008.06.021.

[57] Naess, A. and Gaidai, O. 'Monte Carlo methods for estimating the extreme response of dynamical systems'. *Journal of Engineering Mechanics* 134.8 (2008), pp. 628–636. DOI: 10.1061/(ASCE)0733-9399(2008)134:8(628).

[58] Naess, A., Gaidai, O. and Teigen, P. 'Extreme response prediction for nonlinear floating offshore structures by Monte Carlo simulation'. *Applied Ocean Research* 29.4 (2007), pp. 221–230. DOI: 10.1016/j.apor.2007.12.001.

[59] Naess, A. 'Technical note: On the long-term statistics of extremes'. *Applied Ocean Research* 6.4 (1984), pp. 227–228. DOI: 10.1016/0141-1187(84)90061-0.

[60] Naess, A. and Moan, T. *Stochastic Dynamics of Marine Structures*. Cambridge: Cambridge University Press, 2012. DOI: 10.1017/CBO9781139021364.

[61] Nocedal, J. and Wright, S. J. *Numerical Optimization*. 2nd ed. Springer series in operations research and financial engineering. Springer New York, 2006. DOI: 10.1007/978-0-387-40065-5.

[62] Ochi, M. K. *Applied Probability and Stochastic Processes in Engineering and Physical Sciences*. New York: Wiley, 1990, p. 499. URL: http://books.google.com/books?ei=JFOBU7TtFYHcObC4gLgK&id=ID3xAAAAMAAJ&pgis=1.

[63] Ochi, M. K. *Ocean Waves*. Cambridge: Cambridge University Press, 1998. DOI: 10.1017/CBO9780511529559.

[64] Olver, S. 'Fast, numerically stable computation of oscillatory integrals with stationary points'. *BIT Numerical Mathematics* 50.1 (2010), pp. 149–171. DOI: 10.1007/s10543-010-0251-y.

[65] Opgård, B. and Allievi, F. 'Chained floating bridge'. *IABSE Symposium Report*. Vol. 102. IABSE, 2014, pp. 1236–1243. DOI: 10.2749/222137814814067491.

[66] Panicker, N. and Borgman, L. 'Directional spectra from wave-gage arrays'. *Coastal Engineering Proceedings*. Vol. 1. 1970, pp. 117–136. URL: https://journals.tdl.org/icce/index.php/icce/article/view/2612.

[67] Papaioannou, I., Papadimitriou, C. and Straub, D. 'Sequential importance sampling for structural reliability analysis'. *Structural Safety* 62 (2016), pp. 66–75. DOI: 10.1016/j.strusafe.2016.06.002.

[68] Sagrilo, L., Naess, A. and Doria, A. 'On the long-term response of marine structures'. *Applied Ocean Research* 33.3 (2011), pp. 208–214. DOI: 10.1016/j.apor.2011.02.005.

[69] Shinozuka, M. 'Monte Carlo solution of structural dynamics'. *Computers & Structures* 2.5-6 (1972), pp. 855–874. DOI: 10.1016/0045-7949(72)90043-0.

[70] Sigbjörnsson, R. 'Extreme and fatigue response of offshore platforms due to three-dimensional stochastic wave fields'. *Engineering Structures* 3.4 (1981), pp. 219–224. DOI: 10.1016/0141-0296(81)90004-3.

[71] Sigbjörnsson, R. 'Stochastic theory of wave loading processes'. *Engineering Structures* 1.2 (1979), pp. 58–64. DOI: 10.1016/0141-0296(79)90014-2.

[72] Sigbjörnsson, R. and Smith, E. K. 'Wave induced vibrations of gravity platforms: a stochastic theory'. *Applied Mathematical Modelling* 4.3 (1980), pp. 155–165. DOI: 10.1016/0307-904X(80)90125-0.

[73] Stansberg, C. T., Contento, G., Hong, S. W., Irani, M., Ishida, S., Mercier, R., Wang, Y., Wolfram, J., Chaplin, J. and Kriebel, D. 'The specialist committee on waves final report and recommendations to the 23rd ITTC'. *Proceedings of the 23rd ITTC*. 2002, pp. 505–736. URL: http://ittc.info/media/1469/waves.pdf.

[74] The MathWorks Inc. *MATLAB Release 2015a*. Natick, Massachusets, United States, 2015.

[75] Vázquez-Hernández, A., Ellwanger, G. and Sagrilo, L. 'Long-term response analysis of FPSO mooring systems'. *Applied Ocean Research* 33.4 (2011), pp. 375–383. DOI: 10.1016/j.apor.2011.05.003.

[76] WAMIT Inc. *WAMIT User Manual - Version 7.1*. 2015. URL: http://www.wamit.com.

[77] Watanabe, E. and Utsunomiya, T. 'Analysis and design of floating bridges'. *Progress in Structural Engineering and Materials* 5.3 (2003), pp. 127–144. DOI: 10.1002/pse.151.

[78] Weideman, J. 'Numerical integration of periodic functions: a few examples'. *American Mathematical Monthly* 109.1 (2002), pp. 21–36. DOI: 10.2307/2695765.

[79] Winterstein, S. R., Ude, T. C., Cornell, C. A., Bjerager, P and Haver, S. 'Environmental parameters for extreme response: inverse FORM with omission factors'. *Proceedings of the 6th International Conference on Structural Safety and Reliability*. Innsbruck, Austria, 1993.

[80] Zhang, Y., Beer, M. and Quek, S. T. 'Long-term performance assessment and design of offshore structures'. *Computers & Structures* 154 (2015), pp. 101–115. DOI: 10.1016/j.compstruc.2015.02.029.

Previous PhD theses published at the Departement of Marine Technology
(earlier: Faculty of Marine Technology)
NORWEGIAN UNIVERSITY OF SCIENCE AND TECHNOLOGY

Report No.	Author	Title
	Kavlie, Dag	Optimization of Plane Elastic Grillages, 1967
	Hansen, Hans R.	Man-Machine Communication and Data-Storage Methods in Ship Structural Design, 1971
	Gisvold, Kaare M.	A Method for non-linear mixed -integer programming and its Application to Design Problems, 1971
	Lund, Sverre	Tanker Frame Optimalization by means of SUMT-Transformation and Behaviour Models, 1971
	Vinje, Tor	On Vibration of Spherical Shells Interacting with Fluid, 1972
	Lorentz, Jan D.	Tank Arrangement for Crude Oil Carriers in Accordance with the new Anti-Pollution Regulations, 1975
	Carlsen, Carl A.	Computer-Aided Design of Tanker Structures, 1975
	Larsen, Carl M.	Static and Dynamic Analysis of Offshore Pipelines during Installation, 1976
UR-79-01	Brigt Hatlestad, MK	The finite element method used in a fatigue evaluation of fixed offshore platforms. (Dr.Ing. Thesis)
UR-79-02	Erik Pettersen, MK	Analysis and design of cellular structures. (Dr.Ing. Thesis)
UR-79-03	Sverre Valsgård, MK	Finite difference and finite element methods applied to nonlinear analysis of plated structures. (Dr.Ing. Thesis)
UR-79-04	Nils T. Nordsve, MK	Finite element collapse analysis of structural members considering imperfections and stresses due to fabrication. (Dr.Ing. Thesis)
UR-79-05	Ivar J. Fylling, MK	Analysis of towline forces in ocean towing systems. (Dr.Ing. Thesis)
UR-80-06	Nils Sandsmark, MM	Analysis of Stationary and Transient Heat Conduction by the Use of the Finite Element Method. (Dr.Ing. Thesis)
UR-80-09	Sverre Haver, MK	Analysis of uncertainties related to the stochastic modeling of ocean waves. (Dr.Ing. Thesis)
UR-81-15	Odland, Jonas	On the Strength of welded Ring stiffened cylindrical Shells primarily subjected to axial Compression
UR-82-17	Engesvik, Knut	Analysis of Uncertainties in the fatigue Capacity of

		Welded Joints
UR-82-18	Rye, Henrik	Ocean wave groups
UR-83-30	Eide, Oddvar Inge	On Cumulative Fatigue Damage in Steel Welded Joints
UR-83-33	Mo, Olav	Stochastic Time Domain Analysis of Slender Offshore Structures
UR-83-34	Amdahl, Jørgen	Energy absorption in Ship-platform impacts
UR-84-37	Mørch, Morten	Motions and mooring forces of semi submersibles as determined by full-scale measurements and theoretical analysis
UR-84-38	Soares, C. Guedes	Probabilistic models for load effects in ship structures
UR-84-39	Aarsnes, Jan V.	Current forces on ships
UR-84-40	Czujko, Jerzy	Collapse Analysis of Plates subjected to Biaxial Compression and Lateral Load
UR-85-46	Alf G. Engseth, MK	Finite element collapse analysis of tubular steel offshore structures. (Dr.Ing. Thesis)
UR-86-47	Dengody Sheshappa, MP	A Computer Design Model for Optimizing Fishing Vessel Designs Based on Techno-Economic Analysis. (Dr.Ing. Thesis)
UR-86-48	Vidar Aanesland, MH	A Theoretical and Numerical Study of Ship Wave Resistance. (Dr.Ing. Thesis)
UR-86-49	Heinz-Joachim Wessel, MK	Fracture Mechanics Analysis of Crack Growth in Plate Girders. (Dr.Ing. Thesis)
UR-86-50	Jon Taby, MK	Ultimate and Post-ultimate Strength of Dented Tubular Members. (Dr.Ing. Thesis)
UR-86-51	Walter Lian, MH	A Numerical Study of Two-Dimensional Separated Flow Past Bluff Bodies at Moderate KC-Numbers. (Dr.Ing. Thesis)
UR-86-52	Bjørn Sortland, MH	Force Measurements in Oscillating Flow on Ship Sections and Circular Cylinders in a U-Tube Water Tank. (Dr.Ing. Thesis)
UR-86-53	Kurt Strand, MM	A System Dynamic Approach to One-dimensional Fluid Flow. (Dr.Ing. Thesis)
UR-86-54	Arne Edvin Løken, MH	Three Dimensional Second Order Hydrodynamic Effects on Ocean Structures in Waves. (Dr.Ing. Thesis)
UR-86-55	Sigurd Falch, MH	A Numerical Study of Slamming of Two-Dimensional Bodies. (Dr.Ing. Thesis)
UR-87-56	Arne Braathen, MH	Application of a Vortex Tracking Method to the Prediction of Roll Damping of a Two-Dimension Floating Body. (Dr.Ing. Thesis)

UR-87-57	Bernt Leira, MK	Gaussian Vector Processes for Reliability Analysis involving Wave-Induced Load Effects. (Dr.Ing. Thesis)
UR-87-58	Magnus Småvik, MM	Thermal Load and Process Characteristics in a Two-Stroke Diesel Engine with Thermal Barriers (in Norwegian). (Dr.Ing. Thesis)
MTA-88-59	Bernt Arild Bremdal, MP	An Investigation of Marine Installation Processes – A Knowledge - Based Planning Approach. (Dr.Ing. Thesis)
MTA-88-60	Xu Jun, MK	Non-linear Dynamic Analysis of Space-framed Offshore Structures. (Dr.Ing. Thesis)
MTA-89-61	Gang Miao, MH	Hydrodynamic Forces and Dynamic Responses of Circular Cylinders in Wave Zones. (Dr.Ing. Thesis)
MTA-89-62	Martin Greenhow, MH	Linear and Non-Linear Studies of Waves and Floating Bodies. Part I and Part II. (Dr.Techn. Thesis)
MTA-89-63	Chang Li, MH	Force Coefficients of Spheres and Cubes in Oscillatory Flow with and without Current. (Dr.Ing. Thesis
MTA-89-64	Hu Ying, MP	A Study of Marketing and Design in Development of Marine Transport Systems. (Dr.Ing. Thesis)
MTA-89-65	Arild Jæger, MH	Seakeeping, Dynamic Stability and Performance of a Wedge Shaped Planing Hull. (Dr.Ing. Thesis)
MTA-89-66	Chan Siu Hung, MM	The dynamic characteristics of tilting-pad bearings
MTA-89-67	Kim Wikstrøm, MP	Analysis av projekteringen for ett offshore projekt. (Licenciat-avhandling)
MTA-89-68	Jiao Guoyang, MK	Reliability Analysis of Crack Growth under Random Loading, considering Model Updating. (Dr.Ing. Thesis)
MTA-89-69	Arnt Olufsen, MK	Uncertainty and Reliability Analysis of Fixed Offshore Structures. (Dr.Ing. Thesis)
MTA-89-70	Wu Yu-Lin, MR	System Reliability Analyses of Offshore Structures using improved Truss and Beam Models. (Dr.Ing. Thesis)
MTA-90-71	Jan Roger Hoff, MH	Three-dimensional Green function of a vessel with forward speed in waves. (Dr.Ing. Thesis)
MTA-90-72	Rong Zhao, MH	Slow-Drift Motions of a Moored Two-Dimensional Body in Irregular Waves. (Dr.Ing. Thesis)
MTA-90-73	Atle Minsaas, MP	Economical Risk Analysis. (Dr.Ing. Thesis)
MTA-90-74	Knut-Aril Farnes, MK	Long-term Statistics of Response in Non-linear Marine Structures. (Dr.Ing. Thesis)
MTA-90-75	Torbjørn Sotberg, MK	Application of Reliability Methods for Safety Assessment of Submarine Pipelines. (Dr.Ing.

		Thesis)
MTA-90-76	Zeuthen, Steffen, MP	SEAMAID. A computational model of the design process in a constraint-based logic programming environment. An example from the offshore domain. (Dr.Ing. Thesis)
MTA-91-77	Haagensen, Sven, MM	Fuel Dependant Cyclic Variability in a Spark Ignition Engine - An Optical Approach. (Dr.Ing. Thesis)
MTA-91-78	Løland, Geir, MH	Current forces on and flow through fish farms. (Dr.Ing. Thesis)
MTA-91-79	Hoen, Christopher, MK	System Identification of Structures Excited by Stochastic Load Processes. (Dr.Ing. Thesis)
MTA-91-80	Haugen, Stein, MK	Probabilistic Evaluation of Frequency of Collision between Ships and Offshore Platforms. (Dr.Ing. Thesis)
MTA-91-81	Sødahl, Nils, MK	Methods for Design and Analysis of Flexible Risers. (Dr.Ing. Thesis)
MTA-91-82	Ormberg, Harald, MK	Non-linear Response Analysis of Floating Fish Farm Systems. (Dr.Ing. Thesis)
MTA-91-83	Marley, Mark J., MK	Time Variant Reliability under Fatigue Degradation. (Dr.Ing. Thesis)
MTA-91-84	Krokstad, Jørgen R., MH	Second-order Loads in Multidirectional Seas. (Dr.Ing. Thesis)
MTA-91-85	Molteberg, Gunnar A., MM	The Application of System Identification Techniques to Performance Monitoring of Four Stroke Turbocharged Diesel Engines. (Dr.Ing. Thesis)
MTA-92-86	Mørch, Hans Jørgen Bjelke, MH	Aspects of Hydrofoil Design: with Emphasis on Hydrofoil Interaction in Calm Water. (Dr.Ing. Thesis)
MTA-92-87	Chan Siu Hung, MM	Nonlinear Analysis of Rotordynamic Instabilities in Highspeed Turbomachinery. (Dr.Ing. Thesis)
MTA-92-88	Bessason, Bjarni, MK	Assessment of Earthquake Loading and Response of Seismically Isolated Bridges. (Dr.Ing. Thesis)
MTA-92-89	Langli, Geir, MP	Improving Operational Safety through exploitation of Design Knowledge - an investigation of offshore platform safety. (Dr.Ing. Thesis)
MTA-92-90	Sævik, Svein, MK	On Stresses and Fatigue in Flexible Pipes. (Dr.Ing. Thesis)
MTA-92-91	Ask, Tor Ø., MM	Ignition and Flame Growth in Lean Gas-Air Mixtures. An Experimental Study with a Schlieren System. (Dr.Ing. Thesis)
MTA-86-92	Hessen, Gunnar, MK	Fracture Mechanics Analysis of Stiffened Tubular Members. (Dr.Ing. Thesis)

MTA-93-93	Steinebach, Christian, MM	Knowledge Based Systems for Diagnosis of Rotating Machinery. (Dr.Ing. Thesis)
MTA-93-94	Dalane, Jan Inge, MK	System Reliability in Design and Maintenance of Fixed Offshore Structures. (Dr.Ing. Thesis)
MTA-93-95	Steen, Sverre, MH	Cobblestone Effect on SES. (Dr.Ing. Thesis)
MTA-93-96	Karunakaran, Daniel, MK	Nonlinear Dynamic Response and Reliability Analysis of Drag-dominated Offshore Platforms. (Dr.Ing. Thesis)
MTA-93-97	Hagen, Arnulf, MP	The Framework of a Design Process Language. (Dr.Ing. Thesis)
MTA-93-98	Nordrik, Rune, MM	Investigation of Spark Ignition and Autoignition in Methane and Air Using Computational Fluid Dynamics and Chemical Reaction Kinetics. A Numerical Study of Ignition Processes in Internal Combustion Engines. (Dr.Ing. Thesis)
MTA-94-99	Passano, Elizabeth, MK	Efficient Analysis of Nonlinear Slender Marine Structures. (Dr.Ing. Thesis)
MTA-94-100	Kvålsvold, Jan, MH	Hydroelastic Modelling of Wetdeck Slamming on Multihull Vessels. (Dr.Ing. Thesis)
MTA-94-102	Bech, Sidsel M., MK	Experimental and Numerical Determination of Stiffness and Strength of GRP/PVC Sandwich Structures. (Dr.Ing. Thesis)
MTA-95-103	Paulsen, Hallvard, MM	A Study of Transient Jet and Spray using a Schlieren Method and Digital Image Processing. (Dr.Ing. Thesis)
MTA-95-104	Hovde, Geir Olav, MK	Fatigue and Overload Reliability of Offshore Structural Systems, Considering the Effect of Inspection and Repair. (Dr.Ing. Thesis)
MTA-95-105	Wang, Xiaozhi, MK	Reliability Analysis of Production Ships with Emphasis on Load Combination and Ultimate Strength. (Dr.Ing. Thesis)
MTA-95-106	Ulstein, Tore, MH	Nonlinear Effects of a Flexible Stern Seal Bag on Cobblestone Oscillations of an SES. (Dr.Ing. Thesis)
MTA-95-107	Solaas, Frøydis, MH	Analytical and Numerical Studies of Sloshing in Tanks. (Dr.Ing. Thesis)
MTA-95-108	Hellan, Øyvind, MK	Nonlinear Pushover and Cyclic Analyses in Ultimate Limit State Design and Reassessment of Tubular Steel Offshore Structures. (Dr.Ing. Thesis)
MTA-95-109	Hermundstad, Ole A., MK	Theoretical and Experimental Hydroelastic Analysis of High Speed Vessels. (Dr.Ing. Thesis)
MTA-96-110	Bratland, Anne K., MH	Wave-Current Interaction Effects on Large-Volume Bodies in Water of Finite Depth. (Dr.Ing. Thesis)
MTA-96-111	Herfjord, Kjell, MH	A Study of Two-dimensional Separated Flow by a Combination of the Finite Element Method and

		Navier-Stokes Equations. (Dr.Ing. Thesis)
MTA-96-112	Æsøy, Vilmar, MM	Hot Surface Assisted Compression Ignition in a Direct Injection Natural Gas Engine. (Dr.Ing. Thesis)
MTA-96-113	Eknes, Monika L., MK	Escalation Scenarios Initiated by Gas Explosions on Offshore Installations. (Dr.Ing. Thesis)
MTA-96-114	Erikstad, Stein O., MP	A Decision Support Model for Preliminary Ship Design. (Dr.Ing. Thesis)
MTA-96-115	Pedersen, Egil, MH	A Nautical Study of Towed Marine Seismic Streamer Cable Configurations. (Dr.Ing. Thesis)
MTA-97-116	Moksnes, Paul O., MM	Modelling Two-Phase Thermo-Fluid Systems Using Bond Graphs. (Dr.Ing. Thesis)
MTA-97-117	Halse, Karl H., MK	On Vortex Shedding and Prediction of Vortex-Induced Vibrations of Circular Cylinders. (Dr.Ing. Thesis)
MTA-97-118	Igland, Ragnar T., MK	Reliability Analysis of Pipelines during Laying, considering Ultimate Strength under Combined Loads. (Dr.Ing. Thesis)
MTA-97-119	Pedersen, Hans-P., MP	Levendefiskteknologi for fiskefartøy. (Dr.Ing. Thesis)
MTA-98-120	Vikestad, Kyrre, MK	Multi-Frequency Response of a Cylinder Subjected to Vortex Shedding and Support Motions. (Dr.Ing. Thesis)
MTA-98-121	Azadi, Mohammad R. E., MK	Analysis of Static and Dynamic Pile-Soil-Jacket Behaviour. (Dr.Ing. Thesis)
MTA-98-122	Ulltang, Terje, MP	A Communication Model for Product Information. (Dr.Ing. Thesis)
MTA-98-123	Torbergsen, Erik, MM	Impeller/Diffuser Interaction Forces in Centrifugal Pumps. (Dr.Ing. Thesis)
MTA-98-124	Hansen, Edmond, MH	A Discrete Element Model to Study Marginal Ice Zone Dynamics and the Behaviour of Vessels Moored in Broken Ice. (Dr.Ing. Thesis)
MTA-98-125	Videiro, Paulo M., MK	Reliability Based Design of Marine Structures. (Dr.Ing. Thesis)
MTA-99-126	Mainçon, Philippe, MK	Fatigue Reliability of Long Welds Application to Titanium Risers. (Dr.Ing. Thesis)
MTA-99-127	Haugen, Elin M., MH	Hydroelastic Analysis of Slamming on Stiffened Plates with Application to Catamaran Wetdecks. (Dr.Ing. Thesis)
MTA-99-128	Langhelle, Nina K., MK	Experimental Validation and Calibration of Nonlinear Finite Element Models for Use in Design of Aluminium Structures Exposed to Fire. (Dr.Ing. Thesis)
MTA-99-	Berstad, Are J., MK	Calculation of Fatigue Damage in Ship Structures.

129		(Dr.Ing. Thesis)
MTA-99-130	Andersen, Trond M., MM	Short Term Maintenance Planning. (Dr.Ing. Thesis)
MTA-99-131	Tveiten, Bård Wathne, MK	Fatigue Assessment of Welded Aluminium Ship Details. (Dr.Ing. Thesis)
MTA-99-132	Søreide, Fredrik, MP	Applications of underwater technology in deep water archaeology. Principles and practice. (Dr.Ing. Thesis)
MTA-99-133	Tønnessen, Rune, MH	A Finite Element Method Applied to Unsteady Viscous Flow Around 2D Blunt Bodies With Sharp Corners. (Dr.Ing. Thesis)
MTA-99-134	Elvekrok, Dag R., MP	Engineering Integration in Field Development Projects in the Norwegian Oil and Gas Industry. The Supplier Management of Norne. (Dr.Ing. Thesis)
MTA-99-135	Fagerholt, Kjetil, MP	Optimeringsbaserte Metoder for Ruteplanlegging innen skipsfart. (Dr.Ing. Thesis)
MTA-99-136	Bysveen, Marie, MM	Visualization in Two Directions on a Dynamic Combustion Rig for Studies of Fuel Quality. (Dr.Ing. Thesis)
MTA-2000-137	Storteig, Eskild, MM	Dynamic characteristics and leakage performance of liquid annular seals in centrifugal pumps. (Dr.Ing. Thesis)
MTA-2000-138	Sagli, Gro, MK	Model uncertainty and simplified estimates of long term extremes of hull girder loads in ships. (Dr.Ing. Thesis)
MTA-2000-139	Tronstad, Harald, MK	Nonlinear analysis and design of cable net structures like fishing gear based on the finite element method. (Dr.Ing. Thesis)
MTA-2000-140	Kroneberg, André, MP	Innovation in shipping by using scenarios. (Dr.Ing. Thesis)
MTA-2000-141	Haslum, Herbjørn Alf, MH	Simplified methods applied to nonlinear motion of spar platforms. (Dr.Ing. Thesis)
MTA-2001-142	Samdal, Ole Johan, MM	Modelling of Degradation Mechanisms and Stressor Interaction on Static Mechanical Equipment Residual Lifetime. (Dr.Ing. Thesis)
MTA-2001-143	Baarholm, Rolf Jarle, MH	Theoretical and experimental studies of wave impact underneath decks of offshore platforms. (Dr.Ing. Thesis)
MTA-2001-144	Wang, Lihua, MK	Probabilistic Analysis of Nonlinear Wave-induced Loads on Ships. (Dr.Ing. Thesis)
MTA-2001-145	Kristensen, Odd H. Holt, MK	Ultimate Capacity of Aluminium Plates under Multiple Loads, Considering HAZ Properties. (Dr.Ing. Thesis)
MTA-2001-146	Greco, Marilena, MH	A Two-Dimensional Study of Green-Water

		Loading. (Dr.Ing. Thesis)
MTA-2001-147	Heggelund, Svein E., MK	Calculation of Global Design Loads and Load Effects in Large High Speed Catamarans. (Dr.Ing. Thesis)
MTA-2001-148	Babalola, Olusegun T., MK	Fatigue Strength of Titanium Risers – Defect Sensitivity. (Dr.Ing. Thesis)
MTA-2001-149	Mohammed, Abuu K., MK	Nonlinear Shell Finite Elements for Ultimate Strength and Collapse Analysis of Ship Structures. (Dr.Ing. Thesis)
MTA-2002-150	Holmedal, Lars E., MH	Wave-current interactions in the vicinity of the sea bed. (Dr.Ing. Thesis)
MTA-2002-151	Rognebakke, Olav F., MH	Sloshing in rectangular tanks and interaction with ship motions. (Dr.Ing. Thesis)
MTA-2002-152	Lader, Pål Furset, MH	Geometry and Kinematics of Breaking Waves. (Dr.Ing. Thesis)
MTA-2002-153	Yang, Qinzheng, MH	Wash and wave resistance of ships in finite water depth. (Dr.Ing. Thesis)
MTA-2002-154	Melhus, Øyvin, MM	Utilization of VOC in Diesel Engines. Ignition and combustion of VOC released by crude oil tankers. (Dr.Ing. Thesis)
MTA-2002-155	Ronæss, Marit, MH	Wave Induced Motions of Two Ships Advancing on Parallel Course. (Dr.Ing. Thesis)
MTA-2002-156	Økland, Ole D., MK	Numerical and experimental investigation of whipping in twin hull vessels exposed to severe wet deck slamming. (Dr.Ing. Thesis)
MTA-2002-157	Ge, Chunhua, MK	Global Hydroelastic Response of Catamarans due to Wet Deck Slamming. (Dr.Ing. Thesis)
MTA-2002-158	Byklum, Eirik, MK	Nonlinear Shell Finite Elements for Ultimate Strength and Collapse Analysis of Ship Structures. (Dr.Ing. Thesis)
IMT-2003-1	Chen, Haibo, MK	Probabilistic Evaluation of FPSO-Tanker Collision in Tandem Offloading Operation. (Dr.Ing. Thesis)
IMT-2003-2	Skaugset, Kjetil Bjørn, MK	On the Suppression of Vortex Induced Vibrations of Circular Cylinders by Radial Water Jets. (Dr.Ing. Thesis)
IMT-2003-3	Chezhian, Muthu	Three-Dimensional Analysis of Slamming. (Dr.Ing. Thesis)
IMT-2003-4	Buhaug, Øyvind	Deposit Formation on Cylinder Liner Surfaces in Medium Speed Engines. (Dr.Ing. Thesis)
IMT-2003-5	Tregde, Vidar	Aspects of Ship Design: Optimization of Aft Hull with Inverse Geometry Design. (Dr.Ing. Thesis)
IMT-	Wist, Hanne Therese	Statistical Properties of Successive Ocean Wave

2003-6		Parameters. (Dr.Ing. Thesis)
IMT-2004-7	Ransau, Samuel	Numerical Methods for Flows with Evolving Interfaces. (Dr.Ing. Thesis)
IMT-2004-8	Soma, Torkel	Blue-Chip or Sub-Standard. A data interrogation approach of identity safety characteristics of shipping organization. (Dr.Ing. Thesis)
IMT-2004-9	Ersdal, Svein	An experimental study of hydrodynamic forces on cylinders and cables in near axial flow. (Dr.Ing. Thesis)
IMT-2005-10	Brodtkorb, Per Andreas	The Probability of Occurrence of Dangerous Wave Situations at Sea. (Dr.Ing. Thesis)
IMT-2005-11	Yttervik, Rune	Ocean current variability in relation to offshore engineering. (Dr.Ing. Thesis)
IMT-2005-12	Fredheim, Arne	Current Forces on Net-Structures. (Dr.Ing. Thesis)
IMT-2005-13	Heggernes, Kjetil	Flow around marine structures. (Dr.Ing. Thesis
IMT-2005-14	Fouques, Sebastien	Lagrangian Modelling of Ocean Surface Waves and Synthetic Aperture Radar Wave Measurements. (Dr.Ing. Thesis)
IMT-2006-15	Holm, Håvard	Numerical calculation of viscous free surface flow around marine structures. (Dr.Ing. Thesis)
IMT-2006-16	Bjørheim, Lars G.	Failure Assessment of Long Through Thickness Fatigue Cracks in Ship Hulls. (Dr.Ing. Thesis)
IMT-2006-17	Hansson, Lisbeth	Safety Management for Prevention of Occupational Accidents. (Dr.Ing. Thesis)
IMT-2006-18	Zhu, Xinying	Application of the CIP Method to Strongly Nonlinear Wave-Body Interaction Problems. (Dr.Ing. Thesis)
IMT-2006-19	Reite, Karl Johan	Modelling and Control of Trawl Systems. (Dr.Ing. Thesis)
IMT-2006-20	Smogeli, Øyvind Notland	Control of Marine Propellers. From Normal to Extreme Conditions. (Dr.Ing. Thesis)
IMT-2007-21	Storhaug, Gaute	Experimental Investigation of Wave Induced Vibrations and Their Effect on the Fatigue Loading of Ships. (Dr.Ing. Thesis)
IMT-2007-22	Sun, Hui	A Boundary Element Method Applied to Strongly Nonlinear Wave-Body Interaction Problems. (PhD Thesis, CeSOS)
IMT-2007-23	Rustad, Anne Marthine	Modelling and Control of Top Tensioned Risers. (PhD Thesis, CeSOS)
IMT-2007-24	Johansen, Vegar	Modelling flexible slender system for real-time simulations and control applications
IMT-2007-25	Wroldsen, Anders Sunde	Modelling and control of tensegrity structures.

		(PhD Thesis, CeSOS)
IMT-2007-26	Aronsen, Kristoffer Høye	An experimental investigation of in-line and combined inline and cross flow vortex induced vibrations. (Dr. avhandling, IMT)
IMT-2007-27	Gao, Zhen	Stochastic Response Analysis of Mooring Systems with Emphasis on Frequency-domain Analysis of Fatigue due to Wide-band Response Processes (PhD Thesis, CeSOS)
IMT-2007-28	Thorstensen, Tom Anders	Lifetime Profit Modelling of Ageing Systems Utilizing Information about Technical Condition. (Dr.ing. thesis, IMT)
IMT-2008-29	Refsnes, Jon Erling Gorset	Nonlinear Model-Based Control of Slender Body AUVs (PhD Thesis, IMT)
IMT-2008-30	Berntsen, Per Ivar B.	Structural Reliability Based Position Mooring. (PhD-Thesis, IMT)
IMT-2008-31	Ye, Naiquan	Fatigue Assessment of Aluminium Welded Box-stiffener Joints in Ships (Dr.ing. thesis, IMT)
IMT-2008-32	Radan, Damir	Integrated Control of Marine Electrical Power Systems. (PhD-Thesis, IMT)
IMT-2008-33	Thomassen, Paul	Methods for Dynamic Response Analysis and Fatigue Life Estimation of Floating Fish Cages. (Dr.ing. thesis, IMT)
IMT-2008-34	Pákozdi, Csaba	A Smoothed Particle Hydrodynamics Study of Two-dimensional Nonlinear Sloshing in Rectangular Tanks. (Dr.ing.thesis, IMT/ CeSOS)
IMT-2007-35	Grytøyr, Guttorm	A Higher-Order Boundary Element Method and Applications to Marine Hydrodynamics. (Dr.ing.thesis, IMT)
IMT-2008-36	Drummen, Ingo	Experimental and Numerical Investigation of Nonlinear Wave-Induced Load Effects in Containerships considering Hydroelasticity. (PhD thesis, CeSOS)
IMT-2008-37	Skejic, Renato	Maneuvering and Seakeeping of a Singel Ship and of Two Ships in Interaction. (PhD-Thesis, CeSOS)
IMT-2008-38	Harlem, Alf	An Age-Based Replacement Model for Repairable Systems with Attention to High-Speed Marine Diesel Engines. (PhD-Thesis, IMT)
IMT-2008-39	Alsos, Hagbart S.	Ship Grounding. Analysis of Ductile Fracture, Bottom Damage and Hull Girder Response. (PhD-thesis, IMT)
IMT-2008-40	Graczyk, Mateusz	Experimental Investigation of Sloshing Loading and Load Effects in Membrane LNG Tanks Subjected to Random Excitation. (PhD-thesis, CeSOS)
IMT-2008-41	Taghipour, Reza	Efficient Prediction of Dynamic Response for Flexible amd Multi-body Marine Structures. (PhD-

		thesis, CeSOS)
IMT-2008-42	Ruth, Eivind	Propulsion control and thrust allocation on marine vessels. (PhD thesis, CeSOS)
IMT-2008-43	Nystad, Bent Helge	Technical Condition Indexes and Remaining Useful Life of Aggregated Systems. PhD thesis, IMT
IMT-2008-44	Soni, Prashant Kumar	Hydrodynamic Coefficients for Vortex Induced Vibrations of Flexible Beams, PhD thesis, CeSOS
IMT-2009-45	Amlashi, Hadi K.K.	Ultimate Strength and Reliability-based Design of Ship Hulls with Emphasis on Combined Global and Local Loads. PhD Thesis, IMT
IMT-2009-46	Pedersen, Tom Arne	Bond Graph Modelling of Marine Power Systems. PhD Thesis, IMT
IMT-2009-47	Kristiansen, Trygve	Two-Dimensional Numerical and Experimental Studies of Piston-Mode Resonance. PhD-Thesis, CeSOS
IMT-2009-48	Ong, Muk Chen	Applications of a Standard High Reynolds Number Model and a Stochastic Scour Prediction Model for Marine Structures. PhD-thesis, IMT
IMT-2009-49	Hong, Lin	Simplified Analysis and Design of Ships subjected to Collision and Grounding. PhD-thesis, IMT
IMT-2009-50	Koushan, Kamran	Vortex Induced Vibrations of Free Span Pipelines, PhD thesis, IMT
IMT-2009-51	Korsvik, Jarl Eirik	Heuristic Methods for Ship Routing and Scheduling. PhD-thesis, IMT
IMT-2009-52	Lee, Jihoon	Experimental Investigation and Numerical in Analyzing the Ocean Current Displacement of Longlines. Ph.d.-Thesis, IMT.
IMT-2009-53	Vestbøstad, Tone Gran	A Numerical Study of Wave-in-Deck Impact usin a Two-Dimensional Constrained Interpolation Profile Method, Ph.d.thesis, CeSOS.
IMT-2009-54	Bruun, Kristine	Bond Graph Modelling of Fuel Cells for Marine Power Plants. Ph.d.-thesis, IMT
IMT 2009-55	Holstad, Anders	Numerical Investigation of Turbulence in a Sekwed Three-Dimensional Channel Flow, Ph.d.-thesis, IMT.
IMT 2009-56	Ayala-Uraga, Efren	Reliability-Based Assessment of Deteriorating Ship-shaped Offshore Structures, Ph.d.-thesis, IMT
IMT 2009-57	Kong, Xiangjun	A Numerical Study of a Damaged Ship in Beam Sea Waves. Ph.d.-thesis, IMT/CeSOS.
IMT 2010-58	Kristiansen, David	Wave Induced Effects on Floaters of Aquaculture Plants, Ph.d.-thesis, CeSOS.

IMT 2010-59	Ludvigsen, Martin	An ROV-Toolbox for Optical and Acoustic Scientific Seabed Investigation. Ph.d.-thesis IMT.
IMT 2010-60	Hals, Jørgen	Modelling and Phase Control of Wave-Energy Converters. Ph.d.thesis, CeSOS.
IMT 2010- 61	Shu, Zhi	Uncertainty Assessment of Wave Loads and Ultimate Strength of Tankers and Bulk Carriers in a Reliability Framework. Ph.d. Thesis, IMT/ CeSOS
IMT 2010-62	Shao, Yanlin	Numerical Potential-Flow Studies on Weakly-Nonlinear Wave-Body Interactions with/without Small Forward Speed, Ph.d.thesis,CeSOS.
IMT 2010-63	Califano, Andrea	Dynamic Loads on Marine Propellers due to Intermittent Ventilation. Ph.d.thesis, IMT.
IMT 2010-64	El Khoury, George	Numerical Simulations of Massively Separated Turbulent Flows, Ph.d.-thesis, IMT
IMT 2010-65	Seim, Knut Sponheim	Mixing Process in Dense Overflows with Emphasis on the Faroe Bank Channel Overflow. Ph.d.thesis, IMT
IMT 2010-66	Jia, Huirong	Structural Analysis of Intect and Damaged Ships in a Collission Risk Analysis Perspective. Ph.d.thesis CeSoS.
IMT 2010-67	Jiao, Linlin	Wave-Induced Effects on a Pontoon-type Very Large Floating Structures (VLFS). Ph.D.-thesis, CeSOS.
IMT 2010-68	Abrahamsen, Bjørn Christian	Sloshing Induced Tank Roof with Entrapped Air Pocket. Ph.d.thesis, CeSOS.
IMT 2011-69	Karimirad, Madjid	Stochastic Dynamic Response Analysis of Spar-Type Wind Turbines with Catenary or Taut Mooring Systems. Ph.d.-thesis, CeSOS.
IMT - 2011-70	Erlend Meland	Condition Monitoring of Safety Critical Valves. Ph.d.-thesis, IMT.
IMT – 2011-71	Yang, Limin	Stochastic Dynamic System Analysis of Wave Energy Converter with Hydraulic Power Take-Off, with Particular Reference to Wear Damage Analysis, Ph.d. Thesis, CeSOS.
IMT – 2011-72	Visscher, Jan	Application of Particla Image Velocimetry on Turbulent Marine Flows, Ph.d.Thesis, IMT.
IMT – 2011-73	Su, Biao	Numerical Predictions of Global and Local Ice Loads on Ships. Ph.d.Thesis, CeSOS.
IMT – 2011-74	Liu, Zhenhui	Analytical and Numerical Analysis of Iceberg Collision with Ship Structures. Ph.d.Thesis, IMT.
IMT – 2011-75	Aarsæther, Karl Gunnar	Modeling and Analysis of Ship Traffic by Observation and Numerical Simulation. Ph.d.Thesis, IMT.

Imt – 2011-76	Wu, Jie	Hydrodynamic Force Identification from Stochastic Vortex Induced Vibration Experiments with Slender Beams. Ph.d.Thesis, IMT.
Imt – 2011-77	Amini, Hamid	Azimuth Propulsors in Off-design Conditions. Ph.d.Thesis, IMT.
IMT – 2011-78	Nguyen, Tan-Hoi	Toward a System of Real-Time Prediction and Monitoring of Bottom Damage Conditions During Ship Grounding. Ph.d.thesis, IMT.
IMT- 2011-79	Tavakoli, Mohammad T.	Assessment of Oil Spill in Ship Collision and Grounding, Ph.d.thesis, IMT.
IMT- 2011-80	Guo, Bingjie	Numerical and Experimental Investigation of Added Resistance in Waves. Ph.d.Thesis, IMT.
IMT- 2011-81	Chen, Qiaofeng	Ultimate Strength of Aluminium Panels, considering HAZ Effects, IMT
IMT- 2012-82	Kota, Ravikiran S.	Wave Loads on Decks of Offshore Structures in Random Seas, CeSOS.
IMT- 2012-83	Sten, Ronny	Dynamic Simulation of Deep Water Drilling Risers with Heave Compensating System, IMT.
IMT- 2012-84	Berle, Øyvind	Risk and resilience in global maritime supply chains, IMT.
IMT- 2012-85	Fang, Shaoji	Fault Tolerant Position Mooring Control Based on Structural Reliability, CeSOS.
IMT- 2012-86	You, Jikun	Numerical studies on wave forces and moored ship motions in intermediate and shallow water, CeSOS.
IMT- 2012-87	Xiang ,Xu	Maneuvering of two interacting ships in waves, CeSOS
IMT- 2012-88	Dong, Wenbin	Time-domain fatigue response and reliability analysis of offshore wind turbines with emphasis on welded tubular joints and gear components, CeSOS
IMT- 2012-89	Zhu, Suji	Investigation of Wave-Induced Nonlinear Load Effects in Open Ships considering Hull Girder Vibrations in Bending and Torsion, CeSOS
IMT- 2012-90	Zhou, Li	Numerical and Experimental Investigation of Station-keeping in Level Ice, CeSOS
IMT- 2012-91	Ushakov, Sergey	Particulate matter emission characteristics from diesel enignes operating on conventional and alternative marine fuels, IMT
IMT- 2013-1	Yin, Decao	Experimental and Numerical Analysis of Combined In-line and Cross-flow Vortex Induced Vibrations, CeSOS

IMT-2013-2	Kurniawan, Adi	Modelling and geometry optimisation of wave energy converters, CeSOS
IMT-2013-3	Al Ryati, Nabil	Technical condition indexes doe auxiliary marine diesel engines, IMT
IMT-2013-4	Firoozkoohi, Reza	Experimental, numerical and analytical investigation of the effect of screens on sloshing, CeSOS
IMT-2013-5	Ommani, Babak	Potential-Flow Predictions of a Semi-Displacement Vessel Including Applications to Calm Water Broaching, CeSOS
IMT-2013-6	Xing, Yihan	Modelling and analysis of the gearbox in a floating spar-type wind turbine, CeSOS
IMT-7-2013	Balland, Océane	Optimization models for reducing air emissions from ships, IMT
IMT-8-2013	Yang, Dan	Transitional wake flow behind an inclined flat plate-----Computation and analysis, IMT
IMT-9-2013	Abdillah, Suyuthi	Prediction of Extreme Loads and Fatigue Damage for a Ship Hull due to Ice Action, IMT
IMT-10-2013	Ramìrez, Pedro Agustìn Pèrez	Ageing management and life extension of technical systems- Concepts and methods applied to oil and gas facilities, IMT
IMT-11-2013	Chuang, Zhenju	Experimental and Numerical Investigation of Speed Loss due to Seakeeping and Maneuvering. IMT
IMT-12-2013	Etemaddar, Mahmoud	Load and Response Analysis of Wind Turbines under Atmospheric Icing and Controller System Faults with Emphasis on Spar Type Floating Wind Turbines, IMT
IMT-13-2013	Lindstad, Haakon	Strategies and measures for reducing maritime CO2 emissons, IMT
IMT-14-2013	Haris, Sabril	Damage interaction analysis of ship collisions, IMT
IMT-15-2013	Shainee, Mohamed	Conceptual Design, Numerical and Experimental Investigation of a SPM Cage Concept for Offshore Mariculture, IMT
IMT-16-2013	Gansel, Lars	Flow past porous cylinders and effects of biofouling and fish behavior on the flow in and around Atlantic salmon net cages, IMT
IMT-17-2013	Gaspar, Henrique	Handling Aspects of Complexity in Conceptual Ship Design, IMT
IMT-18-2013	Thys, Maxime	Theoretical and Experimental Investigation of a Free Running Fishing Vessel at Small Frequency of Encounter, CeSOS
IMT-19-2013	Aglen, Ida	VIV in Free Spanning Pipelines, CeSOS

IMT-1-2014	Song, An	Theoretical and experimental studies of wave diffraction and radiation loads on a horizontally submerged perforated plate, CeSOS
IMT-2-2014	Rogne, Øyvind Ygre	Numerical and Experimental Investigation of a Hinged 5-body Wave Energy Converter, CeSOS
IMT-3-2014	Dai, Lijuan	Safe and efficient operation and maintenance of offshore wind farms ,IMT
IMT-4-2014	Bachynski, Erin Elizabeth	Design and Dynamic Analysis of Tension Leg Platform Wind Turbines, CeSOS
IMT-5-2014	Wang, Jingbo	Water Entry of Freefall Wedged – Wedge motions and Cavity Dynamics, CeSOS
IMT-6-2014	Kim, Ekaterina	Experimental and numerical studies related to the coupled behavior of ice mass and steel structures during accidental collisions, IMT
IMT-7-2014	Tan, Xiang	Numerical investigation of ship's continuous- mode icebreaking in leverl ice, CeSOS
IMT-8-2014	Muliawan, Made Jaya	Design and Analysis of Combined Floating Wave and Wind Power Facilities, with Emphasis on Extreme Load Effects of the Mooring System, CeSOS
IMT-9-2014	Jiang, Zhiyu	Long-term response analysis of wind turbines with an emphasis on fault and shutdown conditions, IMT
IMT-10-2014	Dukan, Fredrik	ROV Motion Control Systems, IMT
IMT-11-2014	Grimsmo, Nils I.	Dynamic simulations of hydraulic cylinder for heave compensation of deep water drilling risers, IMT
IMT-12-2014	Kvittem, Marit I.	Modelling and response analysis for fatigue design of a semisubmersible wind turbine, CeSOS
IMT-13-2014	Akhtar, Juned	The Effects of Human Fatigue on Risk at Sea, IMT
IMT-14-2014	Syahroni, Nur	Fatigue Assessment of Welded Joints Taking into Account Effects of Residual Stress, IMT
IMT-1-2015	Bøckmann, Eirik	Wave Propulsion of ships, IMT
IMT-2-2015	Wang, Kai	Modelling and dynamic analysis of a semi-submersible floating vertical axis wind turbine, CeSOS
IMT-3-2015	Fredriksen, Arnt Gunvald	A numerical and experimental study of a two-dimensional body with moonpool in waves and current, CeSOS
IMT-4-2015	Jose Patricio Gallardo Canabes	Numerical studies of viscous flow around bluff bodies, IMT

IMT-5-2015	Vegard Longva	Formulation and application of finite element techniques for slender marine structures subjected to contact interactions, IMT
IMT-6-2015	Jacobus De Vaal	Aerodynamic modelling of floating wind turbines, CeSOS
IMT-7-2015	Fachri Nasution	Fatigue Performance of Copper Power Conductors, IMT
IMT-8-2015	Oleh I Karpa	Development of bivariate extreme value distributions for applications in marine technology,CeSOS
IMT-9-2015	Daniel de Almeida Fernandes	An output feedback motion control system for ROVs, AMOS
IMT-10-2015	Bo Zhao	Particle Filter for Fault Diagnosis: Application to Dynamic Positioning Vessel and Underwater Robotics, CeSOS
IMT-11-2015	Wenting Zhu	Impact of emission allocation in maritime transportation, IMT
IMT-12-2015	Amir Rasekhi Nejad	Dynamic Analysis and Design of Gearboxes in Offshore Wind Turbines in a Structural Reliability Perspective, CeSOS
IMT-13-2015	Arturo Jesùs Ortega Malca	Dynamic Response of Flexibles Risers due to Unsteady Slug Flow, CeSOS
IMT-14-2015	Dagfinn Husjord	Guidance and decision-support system for safe navigation of ships operating in close proximity, IMT
IMT-15-2015	Anirban Bhattacharyya	Ducted Propellers: Behaviour in Waves and Scale Effects, IMT
IMT-16-2015	Qin Zhang	Image Processing for Ice Parameter Identification in Ice Management, IMT
IMT-1-2016	Vincentius Rumawas	Human Factors in Ship Design and Operation: An Experiential Learning, IMT
IMT-2-2016	Martin Storheim	Structural response in ship-platform and ship-ice collisions, IMT
IMT-3-2016	Mia Abrahamsen Prsic	Numerical Simulations of the Flow around single and Tandem Circular Cylinders Close to a Plane Wall, IMT
IMT-4-2016	Tufan Arslan	Large-eddy simulations of cross-flow around ship sections, IMT

IMT-5-2016	Pierre Yves-Henry	Parametrisation of aquatic vegetation in hydraulic and coastal research,IMT
IMT-6-2016	Lin Li	Dynamic Analysis of the Instalation of Monopiles for Offshore Wind Turbines, CeSOS
IMT-7-2016	Øivind Kåre Kjerstad	Dynamic Positioning of Marine Vessels in Ice, IMT
IMT-8-2016	Xiaopeng Wu	Numerical Analysis of Anchor Handling and Fish Trawling Operations in a Safety Perspective, CeSOS
IMT-9-2016	Zhengshun Cheng	Integrated Dynamic Analysis of Floating Vertical Axis Wind Turbines, CeSOS
IMT-10-2016	Ling Wan	Experimental and Numerical Study of a Combined Offshore Wind and Wave Energy Converter Concept
IMT-11-2016	Wei Chai	Stochastic dynamic analysis and reliability evaluation of the roll motion for ships in random seas, CeSOS
IMT-12-2016	Øyvind Selnes Patricksson	Decision support for conceptual ship design with focus on a changing life cycle and future uncertainty, IMT
IMT-13-2016	Mats Jørgen Thorsen	Time domain analysis of vortex-induced vibrations, IMT
IMT-14-2016	Edgar McGuinness	Safety in the Norwegian Fishing Fleet – Analysis and measures for improvement, IMT
IMT-15-2016	Sepideh Jafarzadeh	Energy effiency and emission abatement in the fishing fleet, IMT
IMT-16-2016	Wilson Ivan Guachamin Acero	Assessment of marine operations for offshore wind turbine installation with emphasis on response-based operational limits, IMT
IMT-17-2016	Mauro Candeloro	Tools and Methods for Autonomous Operations on Seabed and Water Coumn using Underwater Vehicles, IMT
IMT-18-2016	Valentin Chabaud	Real-Time Hybrid Model Testing of Floating Wind Tubines, IMT
IMT-1-2017	Mohammad Saud Afzal	Three-dimensional streaming in a sea bed boundary layer
IMT-2-2017	Peng Li	A Theoretical and Experimental Study of Wave-induced Hydroelastic Response of a Circular Floating Collar
IMT-3-2017	Martin Bergström	A simulation-based design method for arctic maritime transport systems

IMT-4-2017	Bhushan Taskar	The effect of waves on marine propellers and propulsion
IMT-5-2017	Mohsen Bardestani	A two-dimensional numerical and experimental study of a floater with net and sinker tube in waves and current
IMT-6-2017	Fatemeh Hoseini Dadmarzi	Direct Numerical Simualtion of turbulent wakes behind different plate configurations
IMT-7-2017	Michel R. Miyazaki	Modeling and control of hybrid marine power plants
IMT-8-2017	Giri Rajasekhar Gunnu	Safety and effiency enhancement of anchor handling operations with particular emphasis on the stability of anchor handling vessels
IMT-9-2017	Kevin Koosup Yum	Transient Performance and Emissions of a Turbocharged Diesel Engine for Marine Power Plants
IMT-10-2017	Zhaolong Yu	Hydrodynamic and structural aspects of ship collisions
IMT-11-2017	Martin Hassel	Risk Analysis and Modelling of Allisions between Passing Vessels and Offshore Installations
IMT-12-2017	Astrid H. Brodtkorb	Hybrid Control of Marine Vessels – Dynamic Positioning in Varying Conditions
IMT-13-2017	Kjersti Bruserud	Simultaneous stochastic model of waves and current for prediction of structural design loads
IMT-14-2017	Finn-Idar Grøtta Giske	Long-Term Extreme Response Analysis of Marine Structures Using Inverse Reliability Methods